THESIS FOR THE DEGREE OF DOCTOR OF PHILOSOPHY

Interplay of Thermoelectric and Mechanical Properties of Doped Conjugated Polymers

Mariavittoria Craighero

Department of Chemistry and Chemical Engineering
CHALMERS UNIVERSITY OF TECHNOLOGY
Göteborg, Sweden, 2025

Interplay of Thermoelectric and Mechanical Properties of Doped Conjugated Polymers
MARIAVITTORIA CRAIGHERO

ISBN 978-91-8103-212-3

Doktorsavhandlingar vid Chalmers tekniska högskola
Ny serie nr 5670
ISSN 0346-718X

Department of Chemistry and Chemical Engineering
Chalmers University of Technology
SE-41296 Göteborg
Sweden
Phone: +46 (0)31 772 1000

Cover: Illustration of the fabrication process of conductive yarns based on conjugated polymers and their integration into electronic textiles. These yarns serve as building blocks in wearable thermoelectric generators, which can power other integrated IoT devices by harvesting body heat. The cover is designed by Mariza Mone.

Chalmers Digitaltryck
Göteborg, Sweden, 2025

This project has received funding from the European Union's Horizon 2020 research and innovation programme under the Marie Skłodowska-Curie grant agreement No 955837.

Interplay of Thermoelectric and Mechanical Properties of Doped Conjugated Polymers

MARIAVITTORIA CRAIGHERO

Department of Chemistry and Chemical Engineering
Chalmers University of Technology

ABSTRACT

The rapid growth of interconnected and wearable devices, which together make up the so-called Internet of Things, is increasing the demand for autonomous and on-site energy supplies. One promising solution relies on harvesting heat, an abundant and often wasted energy source, using thermoelectric generators (TEGs) that can directly convert heat into electricity. Wearable small devices, such as health-monitoring sensors and GPS, may be powered by the heat dissipated from the human body using TEGs made of organic semiconductors, such as conjugated polymers, which offer the advantages to be lightweight and flexible. However, to design effective organic TEGs, a good thermoelectric perfomance of conjugated polymers alone is not enough. Long-term stability, bulk processability and mechanical robustness are also essential for their use in wearable electronics.

This thesis explores the structure–property relationships governing the thermoelectric and mechanical behavior of p- and n-type conjugated polymers for their potential use in flexible and wearable electronics. Here, side-chain engineering is used as a tool to improve the thermoelectric performance of thiophene-based conjugated polymers. Shorter oligoether side chains enhance solid-state order, leading to improved charge-carrier mobility and thus a p-type conductor with high electrical conductivity. Additionally, the formation of lateral doping gradients, achieved through the drift of dopant counterions in an electric field, is explored. In turn, gradients are proposed as a viable strategy to improve the thermoelectric performance of non-optimized doped polymers and can serve as a screening tool for new materials. Moreover, the effect of chemical doping on the nanostructure and mechanical behavior of conjugated polymers with oligoether side chains is investigated. Doping enhances solid-state order of these materials, increases the temperatures associated with the onset of polymer relaxation, and raises their elastic modulus. The extent of these changes depends on the type of dopant counterion, suggesting that counterion selection offers a strategy for tailoring the mechanical properties, enabling the design of soft conductors needed for wearable electronics. Finally, the mechanical properties of a n-type conjugated polymer are studied. The suitability of this n-type polymer as coating material for the preparation of conductive multifilaments is assessed, which show a promising stability with a half-life of more than 3 years. The importance of air stability and mechanical robustness for the development of wearable organic TEGs is highlighted throughout.

Keywords: *organic thermoelectrics, conjugated polymers, chemical doping, electrical properties, mechanical properties, wearable devices*

To my beloved parents

NOMENCLATURE

Symbols and Abbreviations

^{19}F NMR	^{19}F nuclear magnetic resonance
DMA	dynamic mechanical analyzer
DMTA	dynamic mechanical thermal analysis
DSC	differential scanning calorimetry
E	Young's modulus
E'	storage modulus
E''	loss modulus
EA	electron affinity
E_g	bandgap energy
FTIR	Fourier transform infrared
GIWAXS	grazing-incidence wide-angle X-ray scattering
HOMO	highest occupied molecular orbital
IE	ionization energy
IoT	Internet of Things
LUMO	lowest unoccupied molecular orbital
n	charge carrier concentration
N_p	number of polarons per unit volume
OLEDs	organic light-emitting diodes
OPVs	organic photovoltaics
PCET	proton-coupled electron-transfer
PF	thermolectric power factor
P_{out}	output power
SEM	scanning electron microscopy
TEGs	thermoelectric generators
T_g	glass transition temperature
T_α	α-relaxation temperature
T_β	β-relaxation temperature
UV-vis-NIR	ultraviolet-visible-near infrared
V_{bias}	bias voltage
V_{oc}	open-circuit voltage
XPS	X-ray photoelectron spectroscopy
ZT	figure of merit
α	Seebeck coefficient
ε	strain
ε_{break}	elongation at break

η_{ion}	ionization efficiency
κ	thermal conductivity
μ	charge carrier mobility
σ	stress
σ_{el}	electrical conductivity

Chemicals

AcN	acetonitrile
AcN-d_3	deuterated acetonitrile
BCF	tris(pentafluorophenyl)borane
BQ	benzoquinone
DDQ	2,3-dichloro-5,6-dicyano-1,4-benzoquinone
DMSO	dimethyl sulfoxide
EBSA	ethylbenzene sulfonic acid
F_4TCNQ	2,3,5,6-tetrafluoro-7,7,8,8-tetracyanoquinodimethane
F_6TCNNQ	1,3,4,5,7,8-hexafluorotetracyanonaphthoquinodimethane
$FeCl_3$	iron(III) chloride
HQ	hydroquinone
H-TFSI	bistriflimidic acid
LiNFSI	lithium bis(nonafluorobutanesulfonyl)imide
LiTFSI	lithium bis(trifluoromethanesulfonyl)imide
Magic Blue	tris(4-bromophenyl)ammoniumyl hexachloroantimonate
Mo(tfd-$COCF_3$)$_3$	molybdenum dithiolene complex
N-DMBI-H	4-(1,3-dimethyl-2,3-dihydro-1*H*-benzimidazol-2-yl)-*N*,*N*-dimethylaniline
P(NDI2OD-T2)	poly[[*N*,*N*′-bis(2-octyldodecyl)-naphthalene-1,4,5,8-bis(dicarboximide)-2,6-diyl]-*alt*-5,5′-(2,2′-bithiophene)]
P3ATs	poly(3-alkylthiophene)s
P3BT	poly(3-butylthiophene)
P3HT	poly(3-hexylthiophene)
PBFDO	poly(benzodifurandione)
PBTTT	poly[2,5-bis(3-dodecylthiophen-2-yl)thieno(3,2-*b*)thiophene]
PCPDTBT	poly[2,6-(4,4-bis(2-hexadecyl)-4*H*-cyclopenta[2,1-*b*;3,4-*b*′]dithiophene)-*alt*-4,7(2,1,3-benzothiadiazole)]
PEDOT:PSS	poly(3,4-ethylenedioxythiophene):polystyrene sulfonate
PEO	poly(ethylene oxide)
TEA	triethylamine

PUBLICATIONS

This thesis consists of an extended summary of the following appended papers:

Paper I
Impact of Oxidation-Induced Ordering on the Electrical and Mechanical Properties of a Polythiophene Co-Processed with Bistriflimidic Acid
Sandra Hultmark, Mariavittoria Craighero, Sepideh Zokaei, Donghyun Kim, Emmy Järsvall, Furqan Farooqi, Sara Marina, Renee Kroon, Jaime Martin, Igor Zozoulenko and Christian Müller
Journal of Materials Chemistry C, **2023**, 11, 8091-8099

Paper II
Impact of Oligoether Side-Chain Length on the Thermoelectric Properties of a Polar Polythiophene
Mariavittoria Craighero, Jiali Guo, Sepideh Zokaei, Sophie Griggs, Junfu Tian, Jesika Asatryan, Joost Kimpel, Renee Kroon, Kai Xu, Juan Sebastian Reparaz, Jaime Martín, Iain McCulloch, Mariano Campoy-Quiles, and Christian Müller
ACS Applied Electronic Materials, **2024**, 6, 2909−2916

Paper III
Electrically Programmed Doping Gradients Optimize the Thermoelectric Power Factor of a Conjugated Polymer
Jian Liu, Mariavittoria Craighero, Vandna K. Gupta, Dorothea Scheunemann, Sri Harish Kumar Paleti, Emmy Järsvall, Youngseok Kim, Kai Xu, Juan Sebastián Reparaz, L. Jan Anton Koster, Mariano Campoy-Quiles, Martijn Kemerink, Anna Martinelli, and Christian Müller
Advanced Functional Materials, **2024**, 2312549

Paper IV
Poly(benzodifurandione) Coated Silk Yarn for Thermoelectric Textiles
Mariavittoria Craighero, Qifan Li, Zijin Zeng, Chunghyeon Choi, Youngseok Kim, Hyungsub Yoon, Tiefeng Liu, Przemyslaw Sowinski, Shuichi Haraguchi, Byungil Hwang, Besira Mihiretie, Simone Fabiano, and Christian Müller
Advanced Science, **2024**, 2406770

Paper V
Free Volume Dependent Side-Chain Relaxation Softens a Chemically Doped Thienothiophene Copolymer
Mariavittoria Craighero, Meghna Jha, Veronica Flores Vela, Joost Kimpel, Andreas Schaefer, Jiali Guo, Jesika Asatryan, Alberto Peinador Veiga, Shuichi Haraguchi, Jaime Martín, Mariano Campoy-Quiles, and Christian Müller
Manuscript in preparation

CONTRIBUTION REPORT

Paper I	Co-author. Carried out mechanical and electrical measurements together with S.Z. Wrote the manuscript together with S.H., S.Z. supervised by C.M.. S.H. carried out thermal analysis with FSC and DSC. E.J. carried out optical spectroscopy and determination of oxidation level. D.K. and I.Z. carried out molecular dynamics simulations. S.M and J.M. carried out GIWAXS measurements. R.K. synthesized the polymer.
Paper II	Main author. Planned the experiments with S.Z and C.M.. Carried out optical spectroscopy, electrical and thermoelectrical measurements. Performed data analysis and estimation of ionization efficiency and charge carrier density with C.M.. Performed thermomechanical measurements with S.Z.. Wrote the manuscript with C.M.. J.G., K.X. J.S.R. and M.C.-Q. carried out thermal conductivity measurements. J.K. carried out size exclusion chromatography. J.A and J.M. carried out GIWAXS measurements. R.K., S.G., J.T. and I.M. synthesized the polymers.
Paper III	Co-author. Performed thermoelectrical measurements for comparison and for symmetry studies using MatLab code written by Y.K.. Prepared samples for thermal conductivity measurements, which were performed by K.X. J.S.R. and M.C.-Q.. Wrote the manuscript together with J.L., C.M. and A.M.. J.L. conceived the project with C.M., and carried out electrical and thermoelectrical measurements, wrote LabView code. V.K.G. and A.M. performed Raman measurements and analysis. E.J. and S.H.K.P. carried out spectroscopy measurements. D. S. and M. K. performed kinetic Monte Carlo simulations. L.J.A.K. performed drift similations.
Paper IV	Shared first author with Q.L.. Planned the experiments with Q.L. and C.M.. Carried out free-standing films and yarns preparation, mechanical, thermoelectrical, SEM, stability measurements together with Q.L.. Prepared small device and performed its characterization together with Q.L. and Y.K.. Wrote the manuscript with C.M.. Q.L. and S.F. contributed to writing the manuscript. Q.L. synthesized the polymer. Z.Z. and B.M. performed device simulations. C.C. and H.Y. fabricated the large prototype. T.L. carried out electrical measumerements of this films. P.S. performed WAXS measurements. S.H. gave support to yarn preparation. B. H. carried out washibility measurements.
Paper V	Main author. Planned the experiments with C.M.. Carried out optical spectroscopy and electrical measurements. Performed data analysis and estimation charge carrier density with M.J., J.K. and A.S.. Carried out mechanical measurements with V.F.V., with support of S.H.. Wrote the manuscript with M.J. and C.M.. M.J. performed FFV calculations. J.K. synthesized the polymer and carried out ^{19}F NMR measurements and data analysis. A.S. carried out XPS measurements and data analysis. J.G. and M.C.-Q. supported the study. J.A., A.P.V. and J.M. carried out GIWAXS measurements.

RELATED PUBLICATIONS NOT INCLUDED IN THIS THESIS

The author has published the following papers which are not included in the thesis:

Paper VI **Robust PEDOT: PSS Wet-Spun Fibers for Thermoelectric Textiles**
Youngseok Kim, Anja Lund, Hyebin Noh, Anna I Hofmann, Mariavittoria Craighero, Sozan Darabi, Sepideh Zokaei, Jae Il Park, Myung-Han Yoon, Christian Müller
Macromolecular Materials and Engineering, **2020**, 305, 1900749

Paper VII **All-Polymer Conducting Fibers and 3D Prints via Melt Processing and Templated Polymerization**
Anna I Hofmann, Ida Ostergren, Youngseok Kim, Sven Fauth, Mariavittoria Craighero, Myung-Han Yoon, Anja Lund, Christian Müller
ACS Applied Materials & Interfaces, **2020**, 12, 8713-8721

Paper VIII **Electrically Conducting Elastomeric Fibers with High Stretchability and Stability**
Sepideh Zokaei, Mariavittoria Craighero, Claudia Cea, Lucas M. Kneissl, Renee Kroon, Dion Khodagholy, Anja Lund, Christian Müller
Small, **2022**, 02102813

Paper IX **Mechanically Adaptive Mixed Ionic-Electronic Conductors Based on a Polar Polythiophene Reinforced with Cellulose Nanofibrils**
Mariza Mone, Youngseok Kim, Sozan Darabi, Sepideh Zokaei, Lovisa Karlsson, Mariavittoria Craighero, Simone Fabiano, Renee Kroon, and Christian Müller
ACS Applied Materials & Interfaces, **2023**, 15, 28300-28309

Paper X **Impact of Doping on the Mechanical Properties of Conjugated Polymers**
Sri Harish Kumar Paleti, Youngseok Kim, Joost Kimpel, Mariavittoria Craighero, Shuichi Haraguchi, and Christian Müller
Chemical Society Reviews, **2024**, 53, 1702-1729

Paper XI **A Surface Passivated Fluorinated Polymer Nanocomposite for Carbon Monoxide Resistant Plasmonic Hydrogen Sensing**
Ida Östergren, Iwan Darmadi, Sarah Lerch, Robson Rosa da Silva, Mariavittoria Craighero, Sri Harish Kumar Paleti, Kasper Moth-Poulsen, Christoph Langhammer, Christian Müller
Journal of Materials Chemistry A, **2024**, 12, 7906-7915

Paper XII **Benchmarking the Elastic Modulus of Conjugated Polymers with Nanoindentation**

Sri Harish Kumar Paleti, Shuichi Haraguchi, Zhiqiang Cao, Mariavittoria Craighero, Joost Kimpel, Zijin Zeng, Przemyslaw Sowinski, Di Zhu, Judith Pons i Tarrés, Youngseok Kim, Qifan Li, Junda Huang, Alexei Kalaboukhov, Besira Mihiretie, Simone Fabiano, Xiaodan Gu, Christian Müller

Macromolecules, **2025**

TABLE OF CONTENT

1 Introduction

Organic electronics is a growing field focused on the use of carbon-based semiconductors for electronic and energy-related applications. Unlike traditional silicon-based technologies, organic electronics are made of, e.g., conductive and semiconductive polymers, potentially offering many advantages such as low cost, large-area fabrication, ease of processing and mechanical flexibility.

This class of materials was firstly discovered in the mid-1970s by Heeger, MacDiarmid, Shirakawa and their research teams,[1] and has since then enabled significant technological progress. Over the past decades, organic semiconductors, such as conjugated polymers, have played a central role in the development of innovative devices across various applications, including organic light-emitting diodes (OLEDs) used in flexible displays,[2, 3] organic solar cells for lightweight photovoltaics (OPVs),[4, 5] bioelectronics,[6, 7] as well as energy storage[8, 9] and harvesting technologies.[10]

One example of the latter is organic thermoelectrics[11, 12] which are the focus of this thesis. Organic thermoelectric generators (TEGs) can directly convert heat into electricity without the need of moving parts, offering a sustainable and promising solution for continuous energy generation. The flexibility and lightweight nature of organic semiconductors make organic thermoelectric generators particularly attractive for wearable applications, where they can serve as power sources for, e.g., healthcare monitoring systems and other Internet of Things (IoT) devices by harvesting the heat dissipated by the human body.[13, 14]

1.1 Conjugated polymers

Conjugated polymers are macromolecules that can exhibit conductive or semiconductive behavior. Their key feature is a conjugated backbone that comprises alternating single- and double-carbon bonds (Figure 1.1). Their semiconducting property arises from sp^2-hybridized carbon atoms, which form both localized σ-bonds with adjacent carbon atoms and delocalized π-bonds with a multitude of carbon atoms in the molecule. Extension of the π-bonding system creates delocalized bonding π and antibonding π* orbitals, shaping the valence band limited by the highest occupied molecular orbital (HOMO) and the conduction band with the lowest unoccupied molecular orbital (LUMO), respectively. The difference in energy between HOMO and LUMO is denoted as the band gap E_g, which defines many of the optical and electrical properties of conjugated polymers. As the conjugation length increases, the band gap E_g decreases reaching values within the typical range of 1.5 - 3 eV for semiconductor materials.

The presence of aromatic units in the backbones of conjugated polymers promote a strong tendency for π-stacking that influences their nanostructure. Typically, ordered domains are embedded in a less ordered matrix. These ordered regions are often characterized by the π-stacking of polymer backbones, while the side chains, which are commonly incorporated to enhance solubility and processability, are oriented orthogonally to the π-stacking direction.

However, π-conjugation and stacking alone do not ensure electrical conductivity. Charge carriers must be introduced, for example, through doping (Sections 1.2).

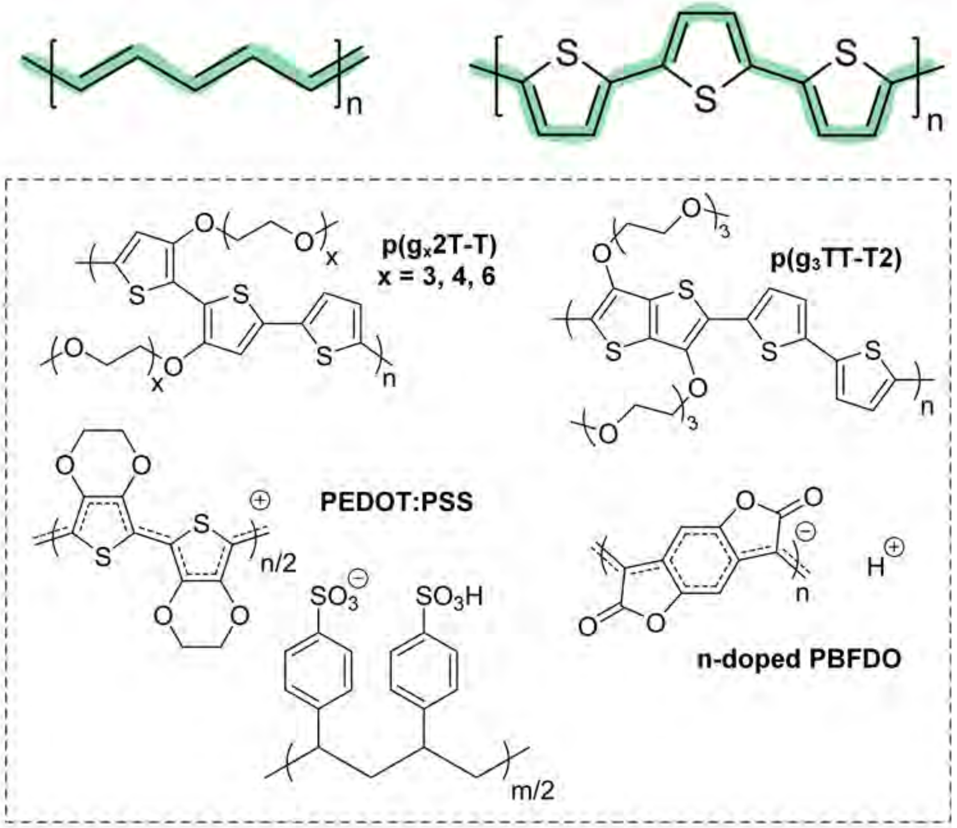

Figure 1.1. Chemical structure of two exemplary conjugated polymers, with the characteristic alternating single-double carbon bonds highlighted, and the conjugated polymers studied in this thesis.

1.2 Chemical doping

Chemical doping is a powerful technique that allows the introduction of charge carriers into conjugated polymers and hence tune their electrical properties. This process typically involves an electron or proton transfer between the conjugated polymer and the dopant species, resulting in the formation of polarons and/or bipolarons/polaron pairs. These are radical cations, in case of p-type doping, or radical anions, in case of n-type doping, that are delocalized along polymer segments and cause intramolecular distortion. The charge neutrality is maintained by the dopant counterions that reside in the vicinity of the charge on the polymer backbone.

The formation of polarons or bipolarons/polaron pairs can also be represented as new electronic states, which give rise to new optical transitions at lower energies (Figure 1.2). Distinct peaks in the near-infrared (NIR) and infrared (IR) serve as optical signatures of charge carriers on the conjugated backbone, enabling their identification.[15, 16]

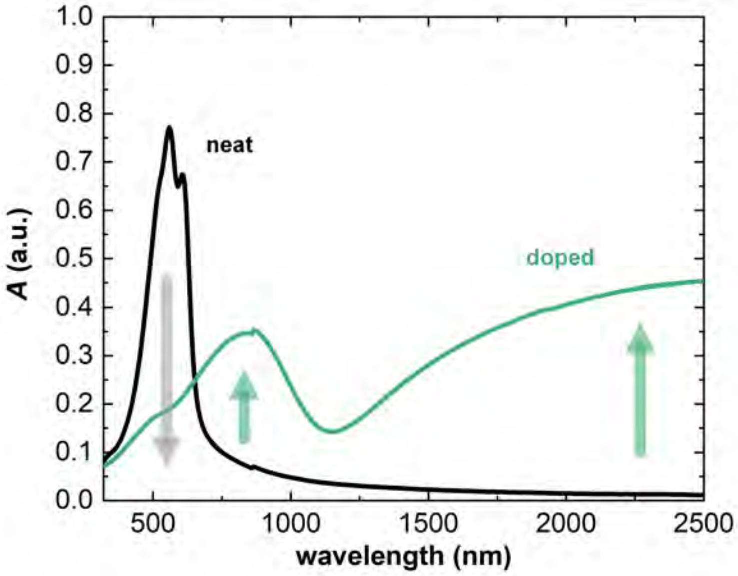

Figure 1.2. UV-vis-NIR absorption spectra showing the absorption *A* for neat p(g_3TT-T2) and p(g_3TT-T2) chemically doped by proton-coupled electron-transfer reaction of benzoquinone (BQ) in the presence of LiNFSI electrolyte.

1.2.1 Doping mechanisms

Two main chemical doping mechanisms are redox doping and acid-base doping.

Chemical redox doping involves the use of molecular dopants that act as oxidizing or reducing agents. Through a redox reaction driven by a favorable energy difference between the ionization energy (IE) or electron affinity (EA) of the polymer and a relevant energy level in case of the dopant, the dopants exchange one or more electrons with the conjugated polymer.

If the dopant accepts electrons from the polymer (often $EA_d > IE_p$ by at least 0.11 eV for efficient electron transfer[17]), p-doping occurs. Conversely, n-doping takes place when the dopant donates electrons to the polymer (often $EA_p > IE_d$) (Figure 1.3).[18]

Redox doping can also occur through the presence of atmospheric oxygen, which can act as an oxidizing agent in acidic conditions.[19, 20] Recently, Fabiano *et al.* showed that redox doping can still occur despite an unfavorable energy difference between IE and EA ($EA_d < IE_p$ for p-doping). Weak dopants, when photoexcited, can facilitate charge transfer with conjugated polymers.[21]

In case of acid-base doping, the charge transfer takes place through the transfer of a proton (H^+) or hydride (H^-) to the polymer backbone resulting in p-doping or n-doping, respectively (Figure 1.3).[22, 23]

An alternative approach is Lewis acid-base doping, where a Lewis acid-base complex facilitates the protonation (or electron transfer) of the polymer backbone. For example, Nguyen *et al.* have argued that a complex of water– tris(pentafluorophenyl)borane (BCF) can protonate high-IE polymers like PCPDTBT,[24] and according to Jang *et al.* and Campoy-Quiles *et al.* a complex of 2,3,5,6-tetrafluoro-7,7,8,8-tetracyanoquinodimethane (F_4TCNQ)-BCF can undergo electron transfer with various polymers.[25, 26]

Figure 1.4 shows the chemical structures of the dopants used in this thesis.

1.2.2 Doping processes

Generally, two methods are used for chemical doping of conjugated polymers: (1) co-processing and (2) sequential processing. Co-processing involves blending the conjugated polymer and dopant through dissolution in the same solvent and processing the resulting solution using techniques such as spin coating or drop casting. Sequential processing, instead, comprises two steps: first processing the conjugated polymer to form a solid sample and then exposing it to a dopant solution or vapor (Figure 1.3). Another approach is ion-exchange doping, where a conjugated polymer film is subjected to a strong oxidizing (or reducing) agent that is dissolved in an electrolyte solution. Oxidation (or reduction) of the film is followed by exchange of the dopant counterions with different ions from the electrolyte (Figure 1.3).[27-29] Takeya *et al.* introduced an alternative doping process based on proton-coupled electron transfer (PCET) of quinones in aqueous solutions at different pH values. Here, a quinone (e.g., benzoquinone, BQ) accepts two electrons from the polymer and two protons (H^+) from the buffered solution to form a neutral hydroquinone (HQ). Since HQ cannot act as a counterion for the p-doped polymer, excess electrolyte anions neutralize the charge on the polymer (Figure 1.3).[30]

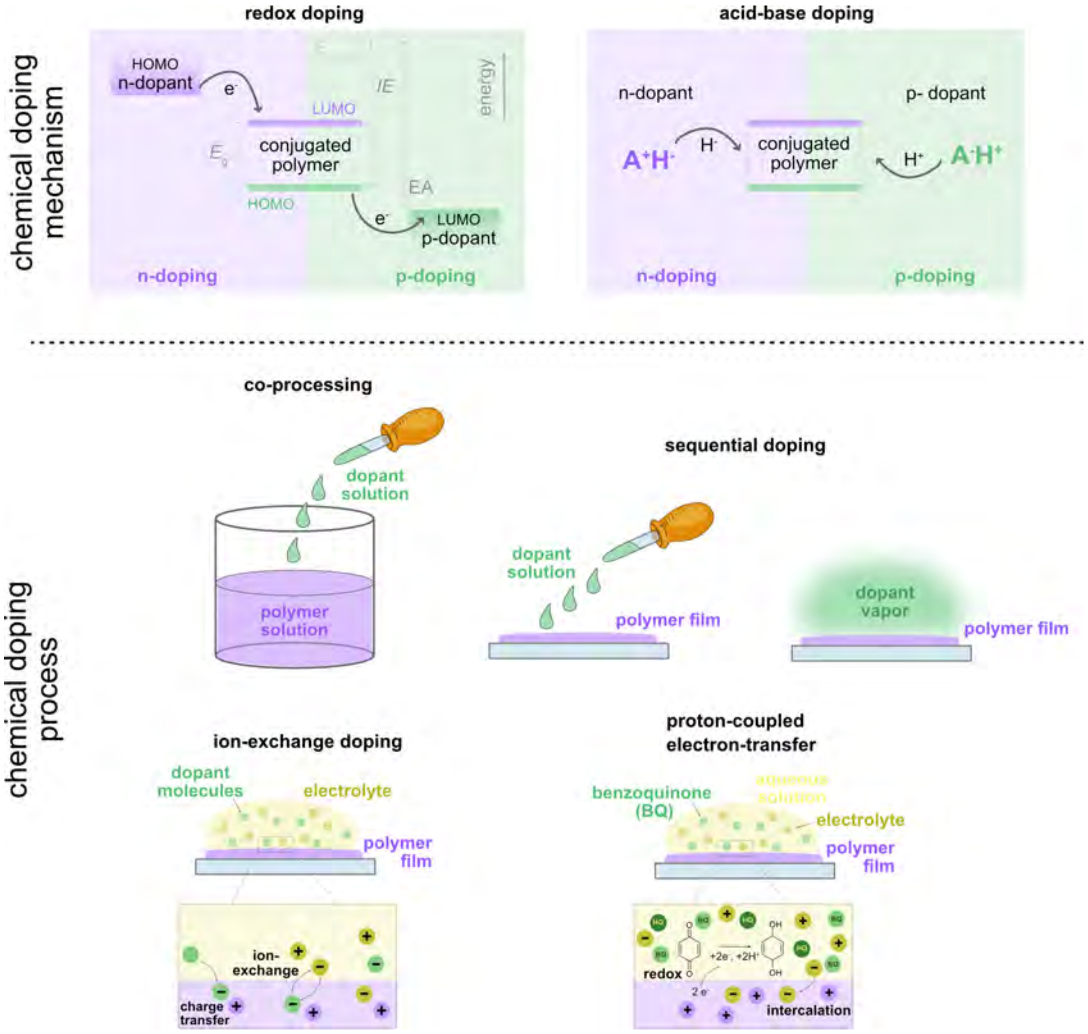

Figure 1.3. Basic principles of redox doping and acid-base doping (top); schematic of different doping processes (bottom): co-processing, sequential doping with dopant solution or dopant vapor, ion-exchange and proton-coupled electron-transfer doping.

1.3 Charge transport in conjugated polymers

Only a fraction of the charge carriers that are introduced via chemical doping are mobile, and thus contribute to charge transport. This usually requires two processes to occur: (1) ionization of polymer and dopant, forming a polaron that is Coulombically bound to the counterion, and (2) dissociation of the polaron from the counterion resulting in a mobile charge.[31]

Charge transport in conjugated polymers often occurs through a thermally activated hopping mechanism of the localized charge carriers, which is typical for disordered structures like organic semiconductors.[31, 32] To achieve efficient charge transport, charge carriers must be able to move freely between polymer chains without being trapped or scattered.

Consequently, several factors can influence charge-carrier transport, such as molecular packing, disorder, the presence of impurities, temperature, electric field and the charge-carrier density. For instance, within ordered domains, the delocalization of charge carriers is promoted by π-stacking, which in turn eases dissociation.[33] Conversely, structural defects, such as conformational changes that lead to backbone twisting in amorphous domains, as well as defects in ordered domains can lead to a loss of conjugation and therefore reduce the mobility of charge carriers.[34] Further, the connectivity between ordered domains influences charge transport. Tie chains, i.e. parts of a polymer chain, that bridge an amorphous domain between adjacent crystallites can aid charge transport. Conversely, transport can be impeded by grain boundaries in otherwise highly ordered materials.[35]

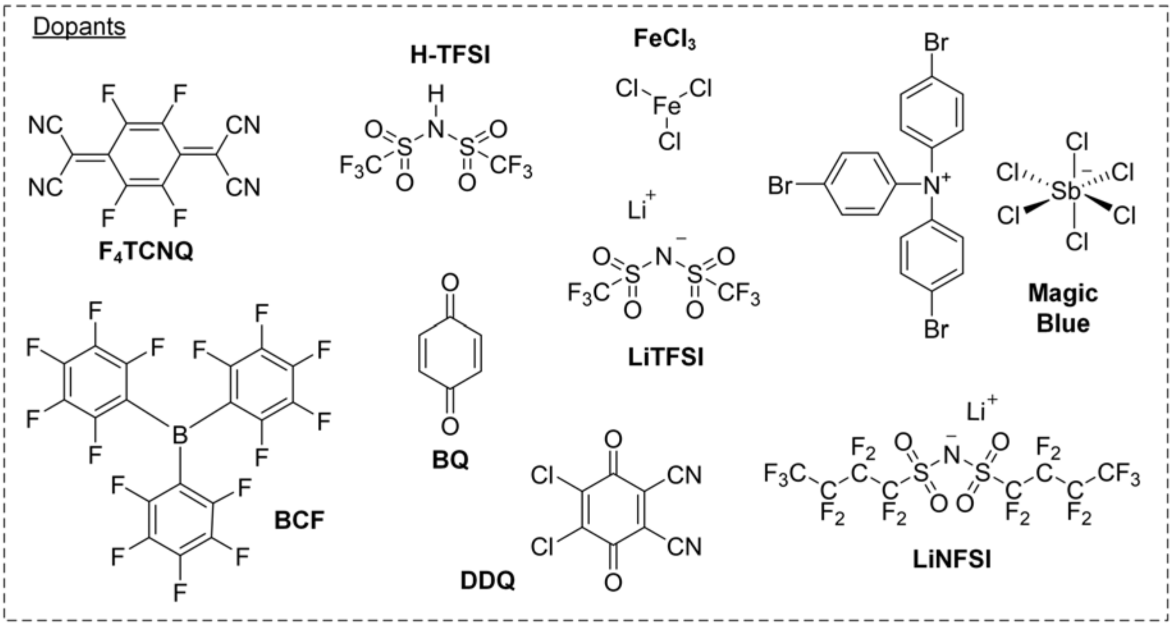

Figure 1.4. Chemical structure of the dopants used in this thesis.

2 Thermoelectric and mechanical properties of conjugated polymers

Conjugated polymers must exhibit excellent (thermo)electrical and mechanical properties to enable the fabrication of mechanically robust and flexible thermoelectric generators.[36, 37] Therefore, the investigation of both thermoelectric and mechanical characteristics of conjugated polymers becomes essential for assessing their usefulness for applications.

In this Section, the thermoelectric (Section 2.1) and mechanical (Section 2.2) properties of conjugated polymers are explored. Additionally, the relationship between these two properties is discussed in Section 2.3.

2.1 Thermoelectric properties of conjugated polymers

When a semiconducting or conducting material is exposed to a temperature difference, charge carriers will move from the hot to the cold side leading to a formation of an electric potential that can be used to drive an electric current (Figure 2.1). This phenomenon is known as the Seebeck effect and was first observed by Thomas J. Seebeck in 1821.[38]

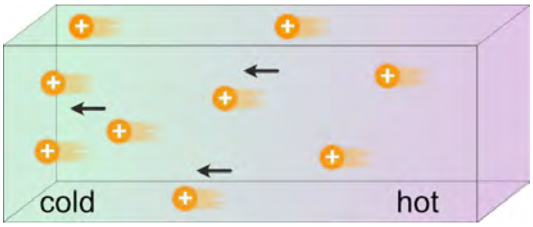

Figure 2.1. Seebeck effect in a p-type semiconductor.

The thermoelectric performance of a material can be evaluated through the dimensionless figure of merit *ZT*, given by:

$$ZT = \frac{\sigma_{el}\alpha^2}{\kappa}T \qquad (2.1)$$

where σ_{el} is the electrical conductivity, α is the Seebeck coefficient, and κ is the thermal conductivity of the material at a given temperature *T*. Therefore, a good thermoelectric material should show a high σ_{el}, high α, and low κ in order to maximize *ZT*. An ideal material would embody the "phonon-glass electron-crystal" concept meaning that it combines the electronic properties of semiconductor single crystals with the thermal properties of amorphous materials.[39]

However, the three thermoelectric parameters are highly interdependent and can vary with temperature. Hence, the optimization of the final performance typically requires a trade-off.

The electrical conductivity is proportional to the product of charge carrier concentration *n* and charge carrier mobility μ, given by

$$\sigma_{el} = nq\mu, \tag{2.2}$$

where q is the elementary charge, i.e. $1.6 \cdot 10^{-19}$ C. σ_{el} increases with the number of charge carriers, which can be tuned by doping (see Section 1.2), and with the mobility μ which depends on polymer chain conformation and solid-state order as well as *n* (see Section 1.3).

The Seebeck coefficient can be seen as a measure of the average entropy per charge carrier. Therefore, α usually decreases upon addition of charge carriers (i.e. doping). α is defined as:

$$\alpha = -\frac{\Delta V}{\Delta T}, \tag{2.3}$$

where ΔV is the electrical potential that arises when a material is exposed to a temperature difference ΔT. The sign of α indicates the type of charge carriers, i.e. $\alpha < 0$ for electrons (n-type semiconductors) and $\alpha > 0$ for holes (p-type semiconductors) (Figure 2.1).

The thermal conductivity κ represents the ability of a material to transfer heat. The total thermal conductivity is composed of a lattice contribution κ_{latt} and an electronic contribution κ_e since both phonons and electrons contribute to heat transport, according to

$$\kappa = \kappa_{latt} + \kappa_e. \tag{2.4}$$

The Wiedemann-Franz law describes how the electronic part depends on σ_{el}, according to

$$\kappa_e = L\sigma_{el}T, \tag{2.5}$$

where L is the Lorenz number, of which the value for organic materials remains a debated topic,[40] and *T* is the temperature. So, when a material has a high electrical conductivity, its thermal transport is generally governed by the electronic contribution ($\kappa_e \gg \kappa_{latt}$). Instead, materials exhibiting a low electrical conductivity have a minor electronic contribution and thus the thermal conductivity is largely governed by the phonon contribution. The classical picture of a phonon is a quantified lattice vibrational energy that transfers heat through lattice vibration, unless it is scattered by defects, impurities, and grain boundaries. Regardless, thermal transport in polymers is governed by defects and grain boundaries, and therefore their intrinsic thermal conductivity is low. Typical values are $\kappa = 0.1 – 0.5$ W m^{-1} K^{-1} and $\kappa = 0.2 – 1$ W m^{-1} K^{-1} for largely amorphous and long-range ordered conjugated polymers, respectively.[41] As a result, conjugated polymers are appealing thermoelectric materials. However, the effect of introducing charge carries (i.e. doping) on the thermal conductivity κ is still unclear. Both an increase due to a larger electronic contribution[42, 43] and a decrease due to solid solution scattering caused by counterions[44, 45] have been reported.

Therefore, enhancing the figure of merit *ZT* is not a trivial task due to the interdependency of the thermoelectric parameters, particularly the interplay between α and σ_{el} with charge-carrier concentration n. Indeed, improving one parameter could negatively affect the other, as shown in Figure 2.2. In this figure, some experimental data collected in this thesis lie on the empirical power-law proposed by Chabinyc *et al.*,[46] which argues that the Seebeck coefficient scales with the electrical conductivity to the power of -0.25.

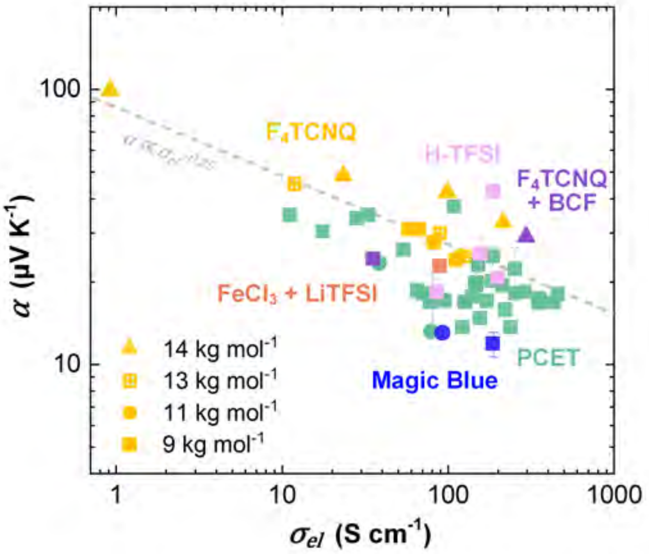

Figure 2.2. Seebeck coefficient α vs. electrical conductivity σ_{el}. Grey dashed line represents $\alpha \propto {\sigma_{el}}^{-0.25}$. Experimental data collected for p(g$_3$TT-T2),[47, 48] with different molecular weights, oxidized with different dopant molecules and doping mechanisms. *Unpublished data.*

Several strategies to decouple the thermoelectric parameters have been proposed. One approach is structural anisotropy,[49] which can be induced by, for example, high-temperature rubbing[50] or drawing.[51] This method aims to improve σ_{el} by increasing the charge carrier mobility μ which benefits from long-range connectivity. An alternative approach is to enhance

α through the modification of the energy landscape achieved by, e.g., mixtures of conjugated polymers.[52, 53]

Considering the interdependency of the thermoelectric parameters, the majority of studies focus on finding the optimal point where the figure of merit ZT or the power factor $PF = \sigma_{el}\alpha^2$ is maximized. However, this thesis will discuss in more detail how the electrical conductivity can be enhanced through different techniques, as discussed in Section 5.

2.2 Mechanical properties of conjugated polymers

Conjugated polymers, like other polymers, display a wide span of mechanical properties,[36, 54, 55] which can be tuned by many approaches, including synthetic design,[56, 57] blending with insulating polymers[58-60] or compounding with nanomaterials, [61, 62] and chemical doping.[20, 63, 64]

Tensile testing is the most widely used technique for investigating the mechanical properties of polymers and can be used to determine the stiffness, ductility, elasticity, stretchability and toughness of a material. In this method, a sample is typically elongated at a fixed strain or force rate, allowing to record the stress σ as a function of strain ε until fracture (Figure 2.3).

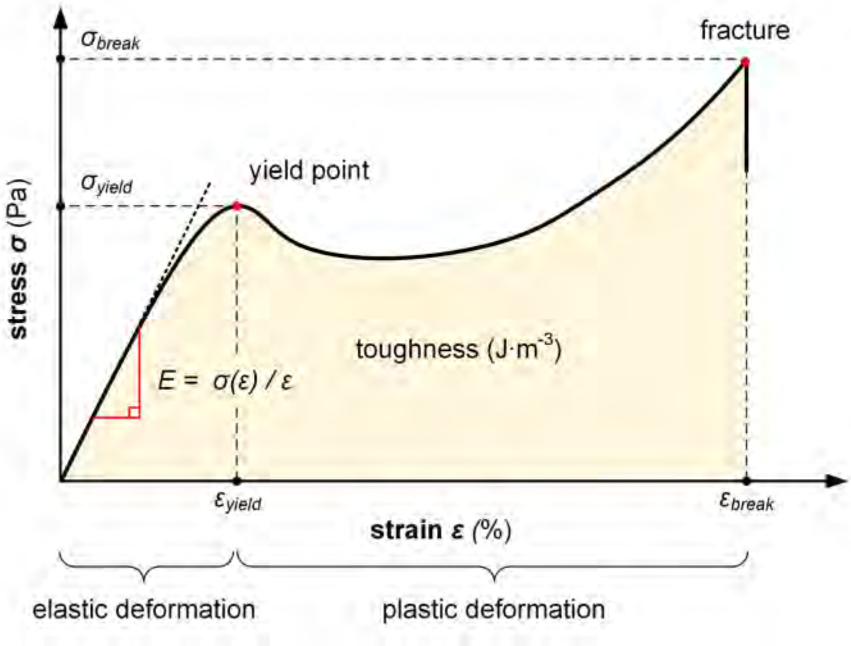

Figure 2.3. Stress–strain curve recorded during a tensile deformation experiment of a ductile polymer allows to determine the Young's modulus E, the yield strain and stress, ε_{yield} and σ_{yield}, the strain and stress at break, ε_{break} and σ_{break}, and the toughness (yellow area under $\sigma(\varepsilon)$). Reproduced from ref [55] with permission from the Royal Society of Chemistry.

Initially, the material undergoes elastic deformation, where σ increases linearly with strain ε. The initial slope of $\sigma(\varepsilon)$ is referred to as the Young's modulus $E = \sigma(\varepsilon)/\varepsilon$. When the applied deformation approaches the yield stress σ_{yield}, the material starts to experience plastic (permanent) deformation. Ultimately, the sample breaks, yielding the stress and strain at break, σ_{break} and ε_{break}. Materials with a low ε_{break} are considered brittle, while ductile materials feature an ε_{break} >> 100%. The area under the stress-strain curve is the toughness, i.e. the energy per volume absorbed by a material during tensile deformation, meaning that an initially stiff and then ductile material has a high toughness.[55, 65]

2.2.1 Viscoelastic behavior

Conjugated polymers, like other polymers, are viscoelastic materials, showing both elastic and viscous behavior. When deformed, they can store and/or dissipate energy through conformational changes on different length scales, given that enough time for relaxation is provided. Such conformational changes are driven by temperature and occur at different temperatures depending on the specific segment of the polymer chain involved. Hence, some characteristic temperatures exist, such as the glass transition temperature T_g, also referred to as α-relaxation temperature T_α, which marks the onset of main-chain relaxation processes, i.e. the polymer backbone, and the β-relaxation temperature T_β, which is associated to the relaxation processes of side-chains where relevant.[66]

As a result, viscoelastic materials display complex rheological and mechanical behavior that depends on temperature, time, frequency and deformation rate.

When a polymer is subjected to dynamic deformation, such as an oscillating sinusoidal strain $\varepsilon(t) = \varepsilon_0 sin\omega t$ in a dynamic mechanical analyzer (DMA), the resulting stress $\sigma(t) = \sigma_0 sin(\omega t + \delta)$ will be out of phase by δ from the strain (Figure 2.4a). The ratios between the stress and strain components define the storage and loss moduli, $E' = \frac{\sigma_0}{\varepsilon_0} cos\,\delta$ and $E'' = \frac{\sigma_0}{\varepsilon_0} sin\,\delta$ respectively. The storage modulus describes the elastic behavior of the material, related to the energy stored in the system during deformation. The loss modulus E'' represents the energy dissipated in the form of, e.g., heat, describing the viscous behavior. Their ratio E'/E'' is called tanδ, which is the damping factor.[55]

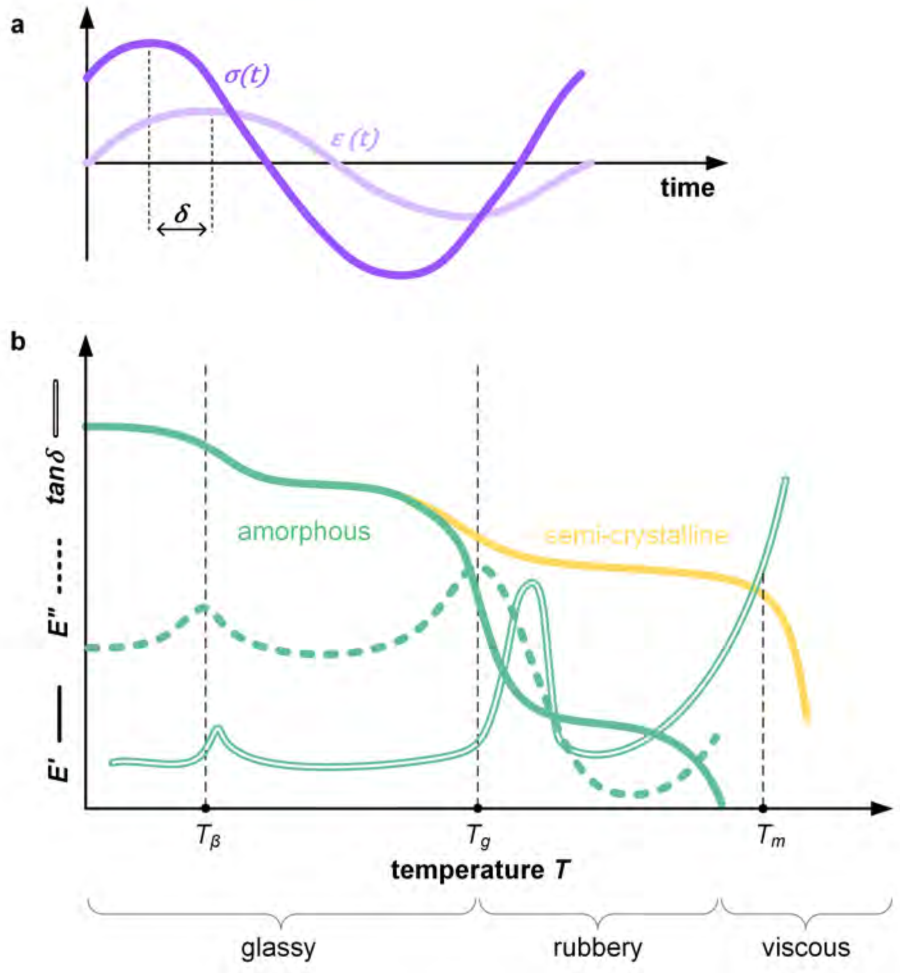

Figure 2.4. a) Oscillating sinusoidal strain $\varepsilon(t)$ applied to a viscoelastic material and the resulting stress $\sigma(t)$, which has a phase difference of δ from the strain. b) DMTA graph for an amorphous polymer (green), showing the variation in storage modulus (E') (solid line), loss modulus (E") (dashed line) and $tan\ \delta$ (double line) with temperature. Adapted from ref [55] with permission from the Royal Society of Chemistry.

Figure 2.4b shows a typical dynamic mechanical thermal analysis (DMTA) thermogram for an amorphous polymer, i.e. $E'$and E'' vs. T. Three principal regions can be distinguished corresponding to the glassy, rubbery and viscous regimes. In the glassy regime, the polymer chains have very little segmental mobility, potentially leading to a sub-glass transition temperature T_β. As a result, the material is brittle with a high E'. The transition from the glassy to the rubbery regime occurs around the T_g due to the onset of main-chain relaxation. The T_g is associated with a significant drop in E' along with a peak in E'' as well as in tanδ, and its position is affected by the frequency and heating/cooling rate. Above the T_g, the rubbery plateau is reached, where E' is constant. The extent of the rubbery plateau depends on the presence of entanglements and crosslinks, which prevent the polymer chains from flowing, and on the molecular weight, which determines how easily a polymer can disentangle.[55] In the viscous regime, polymer chains are completely disentangled and hence free to relax.

The mechanical properties of conjugated polymers vary with temperature and are governed by T_g (Figure 2.5). For instance, conjugated polymers with a T_g below 0 °C, such as, e.g., polythiophenes with oligoether side chains, are soft and ductile at room temperature with an elastic modulus of 1-100 MPa.[61, 63, 64, 67] In contrast, polymers with a T_g above room temperature, like regio-random poly(3-butylthiophene) (P3BT) with a $T_g \approx 45$ °C, are in the glassy state at room temperature with an elastic modulus of several hundred MPa.[68, 69]

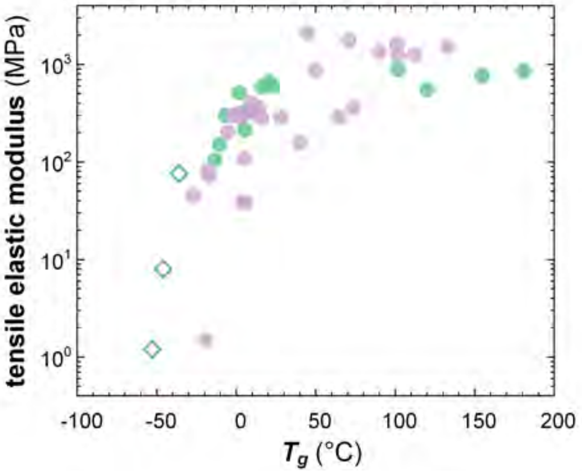

Figure 2.5. Tensile elastic modulus at room temperature vs. the T_g of conjugated polymers with oligoether (open diamond) and alkyl side chains (filled circles). Values from tensile testing or DMTA (green) and from oscillatory shear rheometry (purple, converted using $E = 2G(1 + \nu)$ with $\nu = 0.5$). Adapted from ref [55] with permission from the Royal Society of Chemistry.

2.3 Correlation between electrical and mechanical properties

Both electrical and mechanical properties of conjugated polymers are significantly influenced by their nano- and microstructure, resulting in interdependencies between them.[37]

The presence of ordered domains, such as crystallites or regions where π-stacking occurs, concomitantly enhances charge transport and increases the elastic modulus.[70] Tie chains, which connect ordered domains in conjugated polymers with sufficiently high molecular weight, tend to increase the charge-carrier mobility due to an improved connectivity between ordered domains. At the same time they contribute to achieve a ductile material with a high ε_{break}. Uniaxial orientation, typical for fibers and stretched tapes, also impacts charge transport and stiffness, leading to an enhancement of, e.g., conductivity as well as Young's modulus along the direction of alignment.[51, 71, 72]

Therefore, σ_{el} and E tend to correlate (Figure 2.6). Materials with a high electrical conductivity typically exhibit a high elastic modulus. For instance, materials without side chains such as poly(3,4-ethylenedioxythiophene):polystyrene sulfonate (PEDOT:PSS) and poly(benzodifurandione) (PBFDO:H) tend to feature values of σ_{el} >> 1000 S cm^{-1} and E > 1 GPa.[55, 73-75] Similarly, σ_{el} and E tend to increase in tandem with the oxidation level of conjugated polymers, as observed in the case of polythiophenes with oligoether or alkyl side chains doped with F_4TCNQ.[51, 63, 69]

However, in some cases, this correlation can be partially decoupled through the use of multi-component systems[76, 77] and the addition of suitable dopants, as reported for p(g$_4$2T-T) doped with bistriflimidic acid (H-TFSI).[20] This highlights the potential of selecting appropriate dopants or counterions for the design of conducting materials that are not characterized by a very high stiffness.

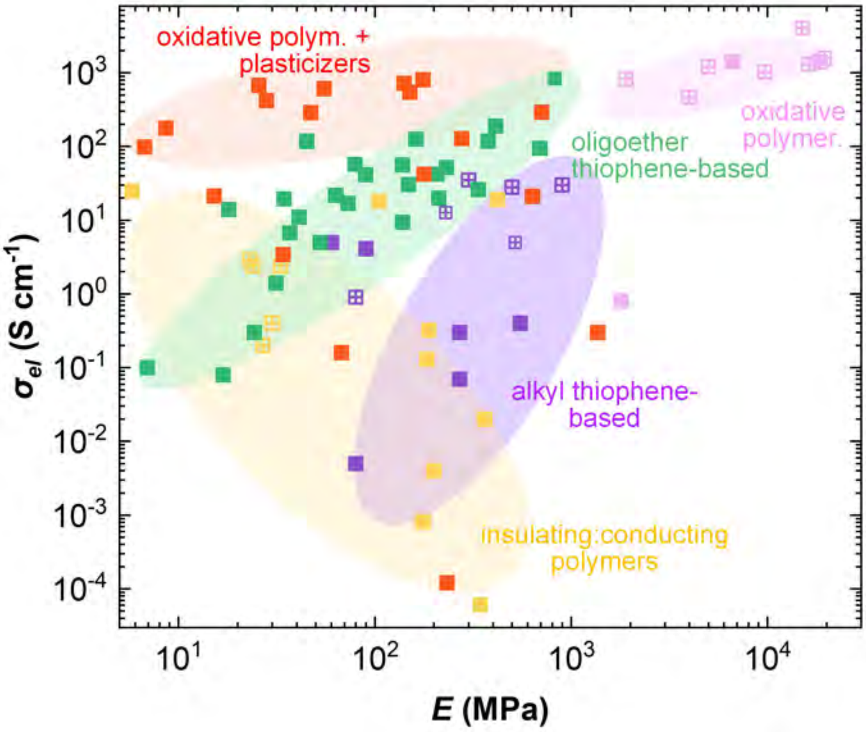

Figure 2.6. Electrical conductivity σ_{el} vs. elastic modulus E for isotropic (filled symbol) and anisotropic (open symbol) doped conjugated polymers. Adapted from ref [78]; references of data therein.

3 Aims of this thesis

The field of organic thermoelectrics has made significant progress in recent years, accompanied by increasing interest in chemical doping as a tool to achieve the high electrical conductivities required.[31, 79] However, some challenges remain, hindering further progress. For instance, doped conjugated polymers often suffer from poor ambient and thermal stability, while n-type polymers exhibit limited performance, i.e. typically an order of magnitude lower than p-type counterparts, as well as air instability. Additionally, the prepration of bulk samples is essential for building prototypes and thermoelectric devices, which necessitates a deeper understanding of their mechanical behavior, a topic that is until now poorly explored.

Within this thesis, I explore the thermoelectric properties of p-doped and n-doped conjugated polymers, their stability over time as well as the interplay between electrical and mechanical properties. The following research questions are addressed:

1. How does the length of oligoether side chains influence the thermoelectric properties of doped polythiophenes? (Section 5)
2. How does the drift of counterions in an electric field affect the thermoelectric properties of chemically doped conjugated polymers with oligoether side chains? (Section 7)
3. How does chemical doping affect the mechanical properties of conjugated polymers with oligoether side chains? (Section 6)
4. Is it possible to decouple the electrical and mechanical properties of doped conjugated polymers to some degree? (Section 6)
5. Which mechanical properties does the newly reported n-type polymer PBFDO have? (Section 6)
6. To what extent can PBFDO be used for the fabrication of mechanically robust textile devices? (Section 8)

4 Determination of charge-carrier density

Chemical doping facilitates the introduction of charge carriers to conjugated polymers, allowing for the optimization of their electrical properties by tuning the charge-carrier concentration n and through the introduction of new energy levels (Section 1.2). Since organic thermoelectrics require a high electrical conductivity, achieving a high doping regime characterized by high charge-carrier density of up to $n = 10^{27}$ m^{-3} is a typical goal.[31]

Given the need of a high n for thermoelectric applications and its influence on the interplay between α and σ_{el} (Section 2.1), determining n experimentally is of critical importance. Once n is known and σ_{el} is measured, the charge-carrier mobility μ can be calculated through Equation 2.2 assuming that each charge carrier is mobile and thus contributes to electronic transport.

Various techniques can be employed to determine the charge-carrier density. For instance, optical absorbance spectroscopy in the UV-vis-NIR range can provide an estimation of the polaron mole fraction by comparing the absorbance peaks associated to the neutral polymer and polaron sites.[80, 81] Additionally, optical spectroscopy can be combined with electrochemistry, i.e. spectroelectrochemistry, to estimate the molar attenuation coefficient of polarons by recording the absorbance spectra and comparison with the injected charges at different doping levels which can be determined with chronoamperometry.[82, 83] Another technique that allows charge-carrier density quantification is electron paramagnetic resonance (EPR) spectroscopy, which is sensitive to unpaired electrons interacting with an external magnetic field. This makes it particularly useful for studying polarons or dopant monovalent counterions in doped conjugated polymers, while bipolarons/polaron pairs are spin silent.[83-85]

Alternative approaches for determining n rely on the quantification of dopant counterions within the polymer film, assuming an ionization efficiency η_{ion}, i.e. the ratio between the number of polarons and number of dopant molecules per unit volume, equal to 100%. For instance, X-ray photoelectron spectroscopy (XPS) or ^{19}F nuclear magnetic resonance (NMR) have been used to quantify the number of TFSI anions in poly[2,5-bis(3-dodecylthiophen-2-yl)thieno(3,2-*b*)thiophene] (PBTTT).[86, 87] Additionally, gas chromatography can detect molecular H_2, a byproduct formed upon doping poly(3-hexylthiophene) (P3HT) with BCF or P(NDI2OD-T2) with 4-(1,3-dimethyl-2,3-dihydro-1*H*-benzimidazol-2-yl)-*N*,*N*-dimethylaniline (N-DMBI-H).[88] Rutherford Back Scattering (RBS) is another analytical technique that can be used to detect, for example, Sb atoms in Magic Blue-doped PBTTT.[89]

In this thesis, I used optical spectroscopy and XPS together with ^{19}F NMR to estimate *n* in F_4TCNQ-doped polythiophenes with oligoether side chains and in a thienothiophene copolymer doped via proton-coupled electron-transfer (PCET) reactions, respectively.

4.1 UV-vis-NIR and FTIR spectroscopy

A series of three polymers with a thiophene-based backbone and oligoether side chains of varying lengths called p(g_x2T-T) with x = 3, 4, or 6 (synthesized according to ref [90, 91] by Sophie Griggs, Dr. Renee Kroon and Junfu Tian, respectively; see Figure 4.1 for chemical structures) were chosen for studying the impact of side-chain length on thermoelectric and mechanical properties (paper II).

Each polymer was co-processed with 20 mol% of F_4TCNQ per thiophene ring. I anticipated that increasing the side-chain length reduces *n*, as a larger volume fraction is occupied by the non-conjugated side chains. To investigate this hypothesis, the number of charge carriers in the three polymers was estimated through comparison of the UV-vis-NIR absorbance spectra of F_4TCNQ-doped polymer films with those of the neutral F_4TCNQ and the F_4TCNQ anion dissolved in dry acetonitrile, as reported by Kiefer *et al.*[92] (Figure 4.1). Specifically, the absorption peaks around 3.4 eV in the UV-vis spectra of doped films were compared with a superposition of the absorption spectra of neutral F_4TCNQ and its anion yielding an estimate of the ratio of ionized and neutral dopant molecules *f* in the films and hence the ionization efficiency $\eta_{ion} = 1/(1+f)$. It should be noted that this method results in a poor description of the experimentally obtained spectra, likely because F_4TCNQ and its anion are in a different dielectric environment, meaning that the obtained value for *f* is only a crude estimate. The number of polarons per unit volume N_p^{UVvis} was estimated by assuming that each F_4TCNQ anion generates one polaron on the polymer backbone (Table 4.1):

$$N_p^{UVvis} = \eta_{ion} \cdot x_d \left(\frac{M_{g_x2T-T}}{3 \cdot \rho_{p(g_x2T-T)}} (100 - x_d) + \frac{M_{F_4TCNQ}}{\rho_{F_4TCNQ}} x_d \right)^{-1}, \tag{4.1}$$

where x_d is the dopant molar concentration (i.e. 20 mol% F_4TCNQ), $\rho_{p(g_x2T-T)}$ = 1 g cm^{-3} and ρ_{F_4TCNQ} = 1.6 g cm^{-3} are the assumed density of p(g_x2T-T) and F_4TCNQ, and M_{g_x2T-T} = 570, 659 or 835 g mol^{-1} and M_{F_4TCNQ} = 276 g mol^{-1} are the molecular weight of the g_x2T-T repeat unit in case of *x* =3, 4 and 6 respectively and F_4TCNQ. The error of N_p^{UVvis} was estimated to be 30%, dominated by the uncertainty in *f* and the film thickness.

Among the three polymers co-processed with 20 mol% F_4TCNQ, p($g_3$2T-T) shows the highest values, i.e. η_{ion}^{UVvis} = 42 ± 14 % and N_p^{UVvis} = (2.8 ± 0.8) · 10^{26} m^{-3}.

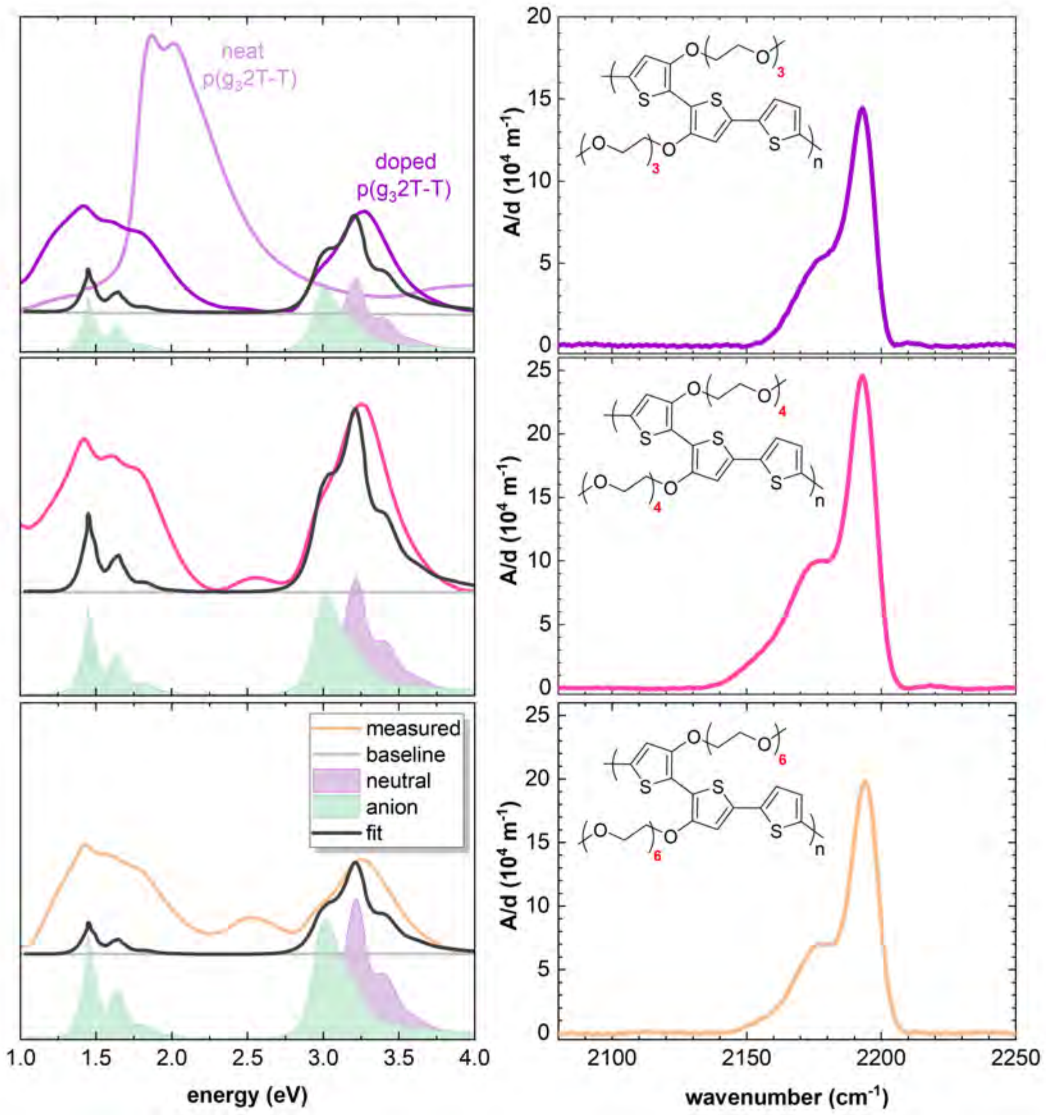

Figure 4.1. Chemical structure of p(g_x2T-T) polymers; UV-vis spectra of neat p($g_3$2T-T) and of p(g_x2T-T) films co-processed with 20 mol% F_4TCNQ (purple, pink, orange line), of neutral F_4TCNQ and its anions in dry acetonitrile from ref [92] (purple and green filled curves) and superposition of the dopant spectra that best describes the measured spectra in the UV region as well as a vertical offset (black and grey, respectively); transmission FTIR absorbance spectra of p(g_x2T-T) films co-processed with 20 mol% F_4TCNQ with the absorbance *A* normalized by the film thickness *d*. Adapted with permission from ref [64] published by ACS Publications.

Transmission FTIR absorbance spectra, which confirmed the absence of F_4TCNQ dianions, were used to obtain an independent estimate of number of polarons for samples co-processed with 20 mol% F_4TCNQ (Figure 4.1). N_p^{FTIR} per unit volume was calculated by comparing the relative intensities of the cyano stretch vibration peaks at 2190 cm^{-1}, which are characteristic of F_4TCNQ anions, with the extinction coefficient previously reported for F_4TCNQ doped p($g_4$2T-T) with an ionization efficiency of 100% (Table 4.1).[63, 92] The extinction coefficient was assumed to scale linearly with the concentration of ionized dopant in the sample, and an error of approximately 30% was considered due to the uncertainty in film thickness. Based on these assumptions and considering that each anion generates one polaron, a value of $\eta_{ion}^{FTIR} = 31 \pm 9$ % is obtained for p($g_3$2T-T), in reasonable agreement with η_{ion}^{UVvis}. Instead, the values obtained for p($g_4$2T-T) and p($g_6$2T-T) are approximately twice those obtained from the analysis of UV-vis spectra.

The number of polarons per unit volume, together with the electrical conductivity σ_{el}, was used to derive the charge carrier mobility μ according to equation 2.2. Regardless the uncertainty in N_p, p($g_3$2T-T) exhibits a much higher μ than p($g_4$2T-T) and p($g_6$2T-T) because of a much higher σ_{el} (see Section 5.1).

Table 4.1. Polymer co-processed with 20 mol% F_4TCNQ per thiophene ring, ionization efficiency η_{ion}^{UVvis} and number of polarons per unit volume N_p^{UVvis} from analysis of UV-vis spectra, number of polarons per unit volume N_p^{FTIR} and ionization efficiency η_{ion}^{FTIR} from analysis of FTIR spectra.

polymer	η_{ion}^{UVvis} (%)	N_p^{UVvis} (10^{26} m^{-3})	η_{ion}^{FTIR} (%)	N_p^{FTIR} (10^{26} m^{-3})
p($g_3$2T-T)	42 ± 14	2.8 ± 0.8	31 ± 9	2.2 ± 0.7
p($g_4$2T-T)	36 ± 12	2.1 ± 0.6	60 ± 18	4.2 ± 1.3
p($g_6$2T-T)	28 ± 9	1.4 ± 0.4	47 ± 14	3.3 ± 1.0

4.2 X-ray Photoelectron Spectroscopy (XPS)

When the absorbance spectra of counterions do not exhibit distinct spectroscopic features in the UV-vis or IR region, which is the case for, e.g. TFSI and NFSI anions, other analytical techniques are needed for determining n. One of these alternative techniques is XPS, which was employed here to characterize the atomic composition near the surface of thin films of the thienothiophene copolymer p(g$_3$TT-T2) with triethylene glycol side chains. This polymer, synthesized by Joost Kimpel,[47, 48] was chemically doped via PCET reactions of 2,3-dichloro-5,6-dicyano-1,4-benzoquinone (DDQ) in the presence of an electrolyte, such as LiNFSI or LiTFSI, in MilliQ water.

XPS is a surface sensitive technique. Hence, the method described here works if there is no doping gradient or unreacted dopant molecules on the top of the film. XPS enables the estimation of the molar ratio of atoms in each species, which is directly related to the ratio of peak integrals for a given transition. Since both p(g$_3$TT-T2) and NFSI contain sulfur, the molar ratio of the anion to the polymer repeat unit can be determined by measuring the areas of the sulfur peaks corresponding to each component, as previously described by Jacobs *et al.*.[87] For the peak fitting, separate $2p$ doublet components were assigned to the neutral polymer chain segments and polarons (Figure 4.2, see Materials and Methods in paper V for fitting details), with the latter being shifted to a higher binding energy due to the positive charge. Distinct $2p$ doublet components were used to describe the peaks arising from the two sulfur atoms of NFSI. The calculated molar ratio of NFSI to polymer repeat unit x_{ox} is around 0.64, which was used to estimate the number of charge carriers per volume N_p^{XPS}, assuming that each counterion corresponds to a polaron and no volume change upon doping, according to:

$$N_p^{XPS} = x_{ox} \cdot N_A \left(\frac{M_{g_3TT-T2}}{\rho_{p(g_3TT-T2)}}\right)^{-1}, \tag{4.2}$$

Here, N_A is Avogadro's number, M_{g_3TT-T2} is the molar mass of the repeat unit, 626.8 g mol^{-1}, and $\rho_{p(g_3TT-T2)}$ is the density of p(g$_3$TT-T2), taken as 1.05 g cm^{-3}, based on the reported value for PBTTT,[68] a similar polymer but with alkyl side chains. Alternatively, if a volume expansion upon doping is considered, leading to a total volume comprising both the polymer and anion, N_p^{XPS} is given by:

$$N_p^{XPS} = x_{ox} \cdot N_A \left(\frac{M_{g_3TT-T2}}{\rho_{p(g_3TT-T2)}}(100 - x_{ox}) + \frac{M_{NFSI}}{\rho_{LiNFSI}} x_{ox}\right)^{-1}, \tag{4.3}$$

where M_{NFSI} is the molar mass of the NFSI anion, 580 g mol^{-1}, and ρ_{LiNFSI} is the density of LiNFSI salt, taken as 1.33 g cm^{-3}, based on the reported value for LiTFSI. Considering a total uncertainty of approximately 20%, resulting from the volume estimation (15%) and the fitting process (5%), the calculated polaron number per volume is N_p^{XPS} = (7.1 ± 1.03) · 10^{26} m^{-3}. The same fitting procedure was performed for XPS spectra recorded for p(g$_3$TT-T2) doped by

PCET with LiTFSI as electrolyte, resulting in a molar ratio of TFSI to polymer repeat of around 0.62, and to a $N_p^{XPS} = (7.2 \pm 1.08) \cdot 10^{26}$ m^{-3}.

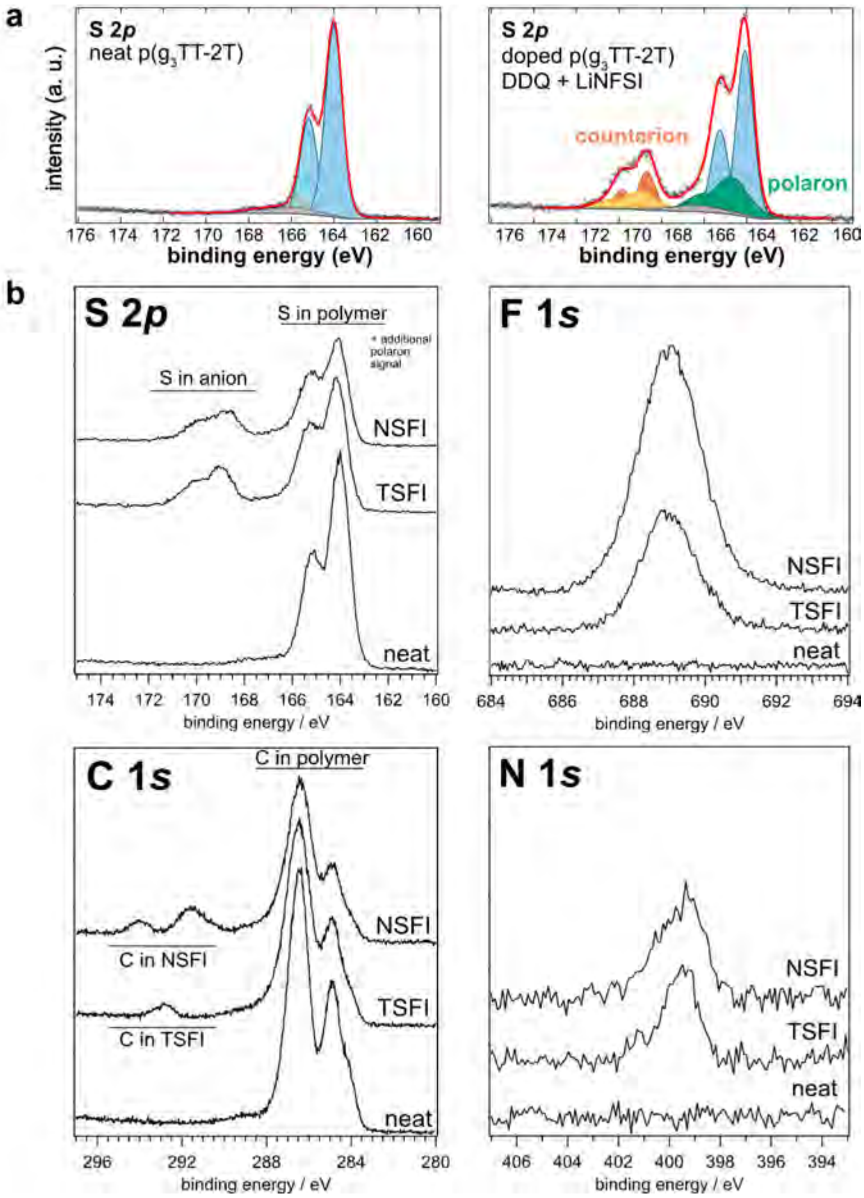

Figure 4.2. XPS spectra of p(g$_3$TT-T2) neat and doped films. a) Sulfur 2*p* XPS spectra of p(g$_3$TT-T2) (left) and p(g$_3$TT-T2):NFSI (right) including peak fits corresponding to signals from the neat polymer (blue), polaron (green) and NFSI (yellow and orange). b) Sulfur S 2*p*, Fluorine F 1*s*, Carbon C 1*s* and Nitrogen N 1*s* XPS spectra of p(g$_3$TT-T2) neat and doped through PCET with TFSI or NFSI counterions. XPS measurement, spectra fitting and data analysis were performed by Dr. Andreas Schaefer. *Unpublished data.*

4.3 ^{19}F nuclear magnetic resonance (NMR)

An alternative technique for quantifying counterions that do not exhibit optical spectroscopic features is nuclear magnetic resonance (NMR), which measures the response of magnetically active nuclei to radiowaves in a magnetic field. Since ^{19}F is a highly abundant, magnetically active nucleus, quantitative ^{19}F NMR allows for the measurement of the absolute concentration of fluorine atoms, e.g. present in the counterions studied here, by integrating the NMR signals of the target species and comparing them to an internal standard of known concentration. The integrated intensity ratios of each signal in an NMR spectrum are proportional to the mole ratio of the corresponding nuclei.

Quantitative ^{19}F NMR was used to determine the number of NFSI anions present in p(g$_3$TT-T2) at different doping levels, as indicated by corresponding UV-vis spectra (Figure 4.3). The polymer was doped via PCET reactions of benzoquinone (BQ) in the presence of aqueous electrolyte, comprising LiNFSI at pH 2, 4 and 7 to achieve various doping levels.[30, 93]

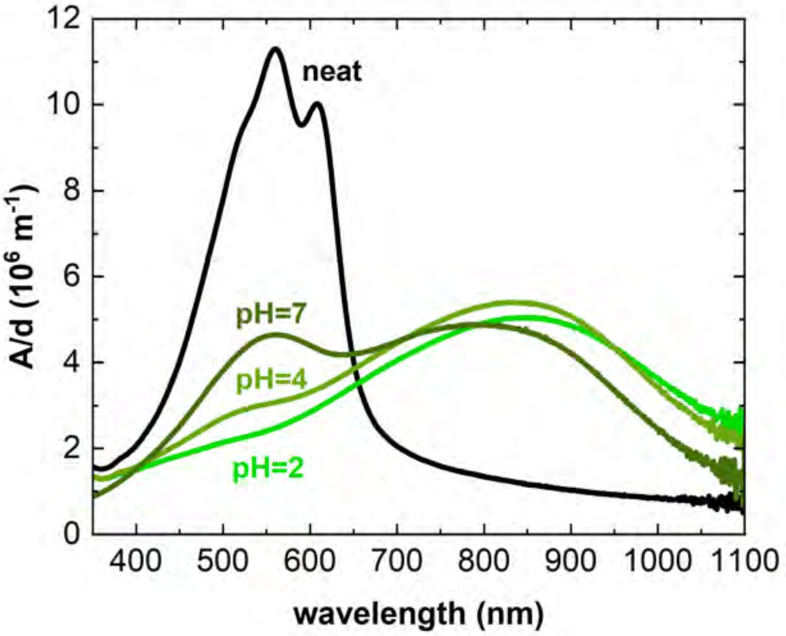

Figure 4.3. UV-vis absorbance spectra of solid thin films of neat and doped p(g$_3$TT-T2) through PCET in aqueous solution with pH 2, 4 or 7. *Unpublished data.*

NFSI counterions were removed from the doped thin films by dedoping the sample with 2 mL of 10% v:v triethylamine (TEA) in deuterated acetonitrile (AcN-d$_3$) solution, as previously reported.[87, 94] ^{19}F NMR spectra of samples composed of 0.7 mL of dedoping solution and 20 μL of 25.5 mM of hexafluorobenzene, used as the reference compound, were recorded (Figure 4.4). UV–vis spectra were measured to confirm dedoping (Figure 4.4), which was almost fully achieved, as evidenced by the nearly complete recovery of the neutral absorption band of the polymer in the visible region. Additionally, before dedoping the polymer films, UV–vis and ^{19}F NMR spectra were recorded for samples that had been prewashed with 2 mL of AcN-d_3 for 2 minutes and for the prewashing solution, respectively (Figure 4.4). The resulting ^{19}F NMR spectra of the prewashing solution revealed a significant amount of NFSI, suggesting an excess of electrolyte on the film surface - despite a prerinsing step performed prior to the prewashing step by spinning off 50 uL of MilliQ water at 3000 rpm - along with a slight dedoping effect, as indicated by the increased intensity of the absorbance peak of the neat polymer at ~ 560 nm in the UV-vis spectra (Figure 4.4). The amount of NFSI in the prewashing solution was not considered for the calculations of the number of charge carriers per unit volume N_p^{NMR}.

The charge-carrier density was estimated by dividing the NFSI concentration obtained from integration of the NMR peaks by the dry film volumes, which ranged from 5 to 10 µm^3. The estimated number of polarons per unit volume is approximately N_p^{NMR}= $(1.2 \pm 0.2) \cdot 10^{27}$ m^{-3},$(6.7 \pm 1.3) \cdot 10^{26}$ m^{-3}, and $(8.6 \pm 1.7) \cdot 10^{25}$ m^{-3} for the samples doped at pH 2, 4 and 7, respectively. An error of around 20% was considered due to uncertainties in the volume measurements of dry samples and the swelling of polymer films upon doping. The calculated N_p^{NMR} values agree with the increase in N_p inferred from UV–vis spectra (Figure 4.3).

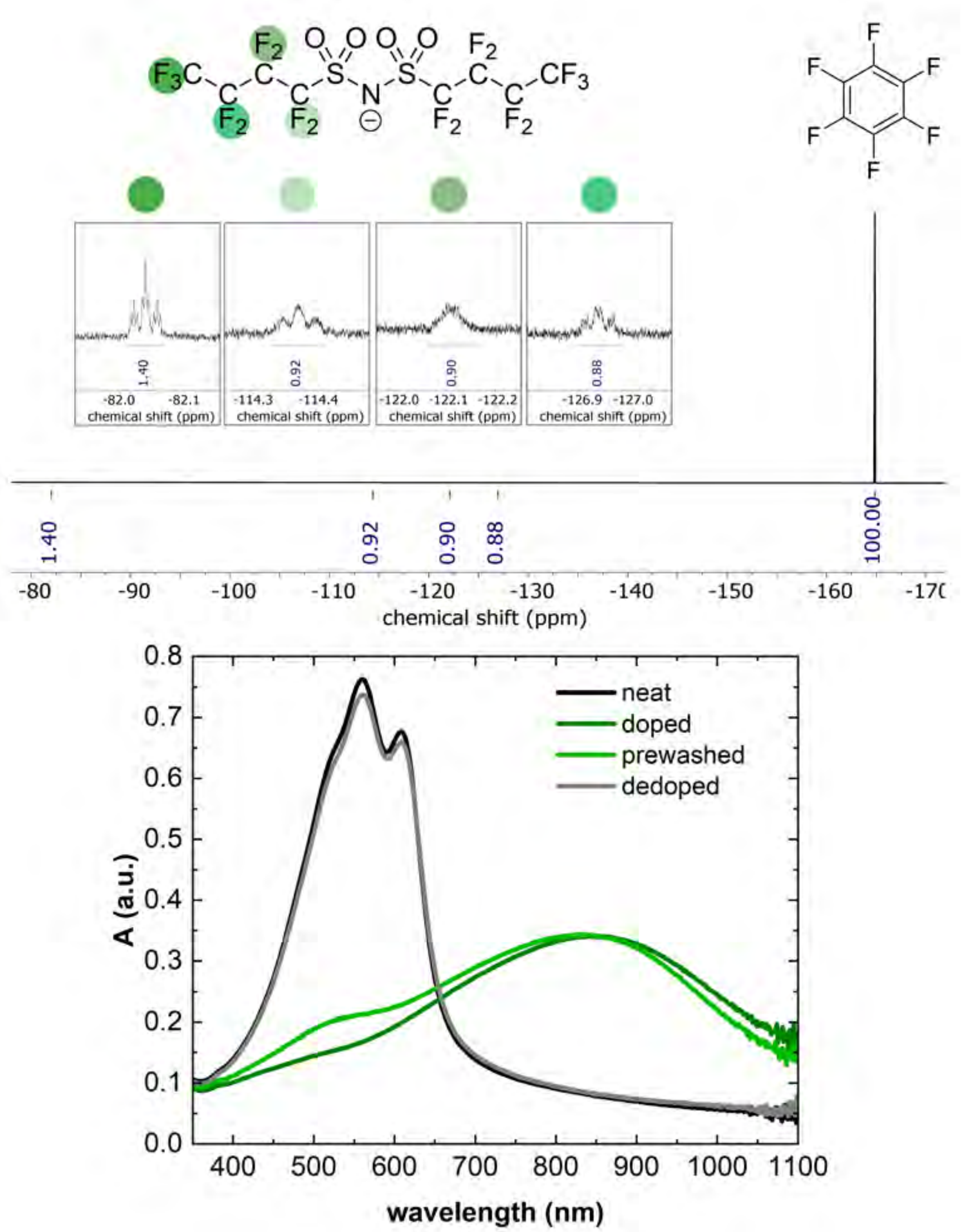

Figure 4.4. Quantitative 19F NMR spectra of the dedoping solution containing NFSI counterions and hexafluorobenzene as the calibration standard. UV-vis absorbance spectra of solid thin films of neat, doped, prewashed and dedoped p(g$_3$TT-T2). Quantitative ^{19}F NMR measurement and spectra analysis were performed by Joost Kimpel. *Unpublished data.*

5 Effect of solid-state order on charge transport and electrical properties

Charge transport in molecularly doped systems is influenced by several factors, including structural characteristics, Coulomb interactions between the charges and the dopant counterions, as well as ionization and dissociation efficiencies (Section 1.3). This Section primarily investigates how solid-state order affects the charge transport properties of p-doped conjugated polymers.

Doping conjugated polymers for thermoelectric applications comprises reaching a high doping regime characterized by high charge-carrier densities up to $n = 10^{27}$ m^{-3} (Section 4). This is typically achieved by introducing a considerable amount of dopant, i.e. tens of mol % with respect to the repeat unit. The amount and size of introduced dopant can significantly influence the nano- and microstructure of conjugated polymers, altering key features such as the degree of order, crystal structure and size, and connectivity between ordered domains. These structural modifications have a significant impact on charge transport and on the resulting electrical properties.

For instance, chemical doping can enhance the degree of π-stacking in less ordered polymers such as regio-random P3HT,[95, 96] induce the formation of new crystalline phases,[97-99] or modify the conjugation length of amorphous segments of the polymer chains, thus improving the connectivity between ordered domains.[89, 100]

The nano- and microstructure of conjugated polymers can be modified not only through molecular doping but also by molecular design or physical post-treatments. For example, planarization of the conjugated backbone is a common strategy to improve intrachain conjugation and interchain π-interactions, leading to more ordered microstructures.[101, 102] Side-chain engineering, commonly used to enhance polymer solubility, can also significantly influence solid-state organization.[103, 104] Additionally, post-processing methods such as thermal annealing[105, 106] and uniaxial chain alignment techniques[50, 51] enable fine-tuning of the microstructure to enhance the charge transport properties.

In this Section, I explore the influence of solid-state order on charge transport through X-ray diffraction analysis and electrical conductivity measurements. In particular, four different ways of how solid-state order can be altered are presented.

5.1 Impact of side chain length and type of side chain

Firstly, I investigated the effect of side-chain length on the microstructure (paper II) for a series of three polymers with a thiophene-based backbone and oligoether side chains (see Figure 4.1 for chemical structures of the polymers). Grazing-incidence wide-angle X-ray scattering (GIWAXS) was used to determine the degree of order of the three polymers, p($g_3$2T-T), p($g_4$2T-T) and p($g_6$2T-T), in their neat and oxidized states.

Films of all three neat polymers show a low degree of order. p($g_3$2T-T) exhibits an out-of-plane $h00$ diffraction peak at $q_{100} \approx 0.30$ Å^{-1}, which indicates the lamella stacking, and a weak in-plane q_{010} diffraction, indicating limited π-stacking, on top of a broad amorphous halo at $q \approx 1.5$ Å^{-1}. From this an edge-on texture is evident (Figure 5.1a). Instead, p($g_4$2T-T) and p($g_6$2T-T) show a face-on orientation with weak out-of-plane q_{010} diffraction peak at $q \approx 1.7$ Å^{-1} and no $h00$ diffraction peaks.

Co-processing the three polymers with 20 mol% of F_4TCNQ results in an increase of structural order of the polymers, as reported for doped regiorandom P3HT.[95] This is evidenced by a clear out-of-plane diffraction peak $q_{010} \approx 1.75$ Å^{-1} that emerges due to π-stacking of the polymer backbone (Figure 5.1b). A change in texture from a predominately edge-on to face-on orientation is observed for p($g_3$2T-T) upon doping, with in-plane $h00$ diffraction peaks and out-of-plane diffraction peak q_{010}.

By comparing the out-of-plane q_{010} diffraction peak of doped p(g_x2T-T) polymers, a decrease in intensity with increasing side-chain length is observed (Figure 5.1b), indicating a higher degree of order for the polymer with the shortest side chains, i.e. p($g_3$2T-T). This correlates with the electrical properties, where p($g_3$2T-T) displays the highest electrical conductivity among the three polymers, reaching a value of $\sigma_{el} = 830 \pm 15$ S cm^{-1}. Instead, p($g_4$2T-T) and p($g_6$2T-T) show comparable values of $\sigma_{el} = 56 \pm 3$ S cm^{-1} and 51 ± 4 S cm^{-1}, respectively. This aligns with the higher degree of order and more pronounced π-stacking of p($g_3$2T-T) compared to p($g_4$2T-T) and p($g_6$2T-T).

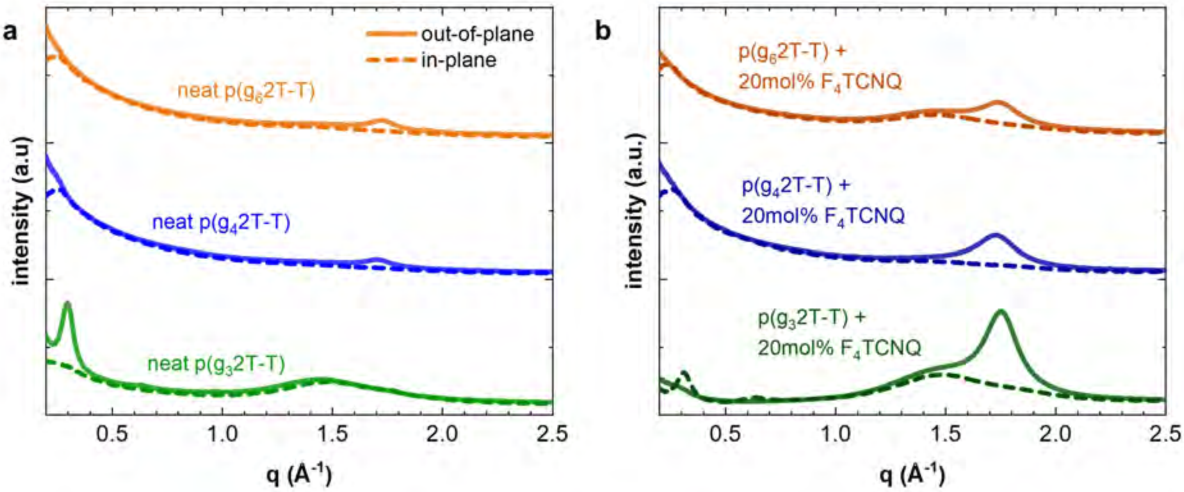

Figure 5.1. GIWAXS diffractograms of p(g$_x$2T-T) a) neat and b) co-processed with 20 mol% of F$_4$TCNQ. GIWAXS measurements were performed by Jesika Asatryan. Adapted with permission from ref [64] published by ACS Publications.

Varying the length of side chains is not the only strategy for modifying the degree of solid-state order in conjugated polymers to improve their electrical conductivity. An alternative approach in side-chain engineering involves the modification of the chemical nature of the side chains.[107-109]

Here, the impact of exchanging oligoether side chains for alkyl side chains was investigated for a random oligoether:alkyl copolymer (x(g$_3$TT-T2):y(a$_{10}$TT-T2), further pTTEG-*co*-pTTA) (Figure 5.2 for chemical structure), synthesized by Di Zhu according to ref [47].

GIWAXS diffraction measurements of the neat polymers revealed that partial substitution of oligoether side chains with alkyl chains results in a decrease of solid-state order (Figure 5.2). This is indicated by the higher π-stacking paracrystallinity $g_{\pi-\pi}$, which quantifies the disorder in ordered domains coming from statistical variations in stacking distances.[34] Specifically, pTTEG-*co*-pTTA exhibited a $g_{\pi-\pi}$ of 14.9%, compared to 12.4% for pTTEG. Sequentially doping with 5mM F$_4$TCNQ solution induces an expansion of the lamellar stacking distance along with a slight contraction of the π-stacking distance in both polymers, as evidenced by the shift of $h00$ diffraction peaks to lower q values and q_{010} to higher q values. Additionally, both doped polymers show a reduction in $g_{\pi-\pi}$ compared to their neat state reaching a value of 10.3% and 11.9% for pTTEG and pTTEG-*co*-pTTA, respectively.

Despite the lower degree of order, pTTEG-*co*-pTTA displays a higher electrical conductivity of 390 ± 12 S cm^{-1} compared to 82 ± 5 S cm^{-1} of pTTEG. This suggests that other parameters than the degree of order appear to play a role and still need to be elucidated.

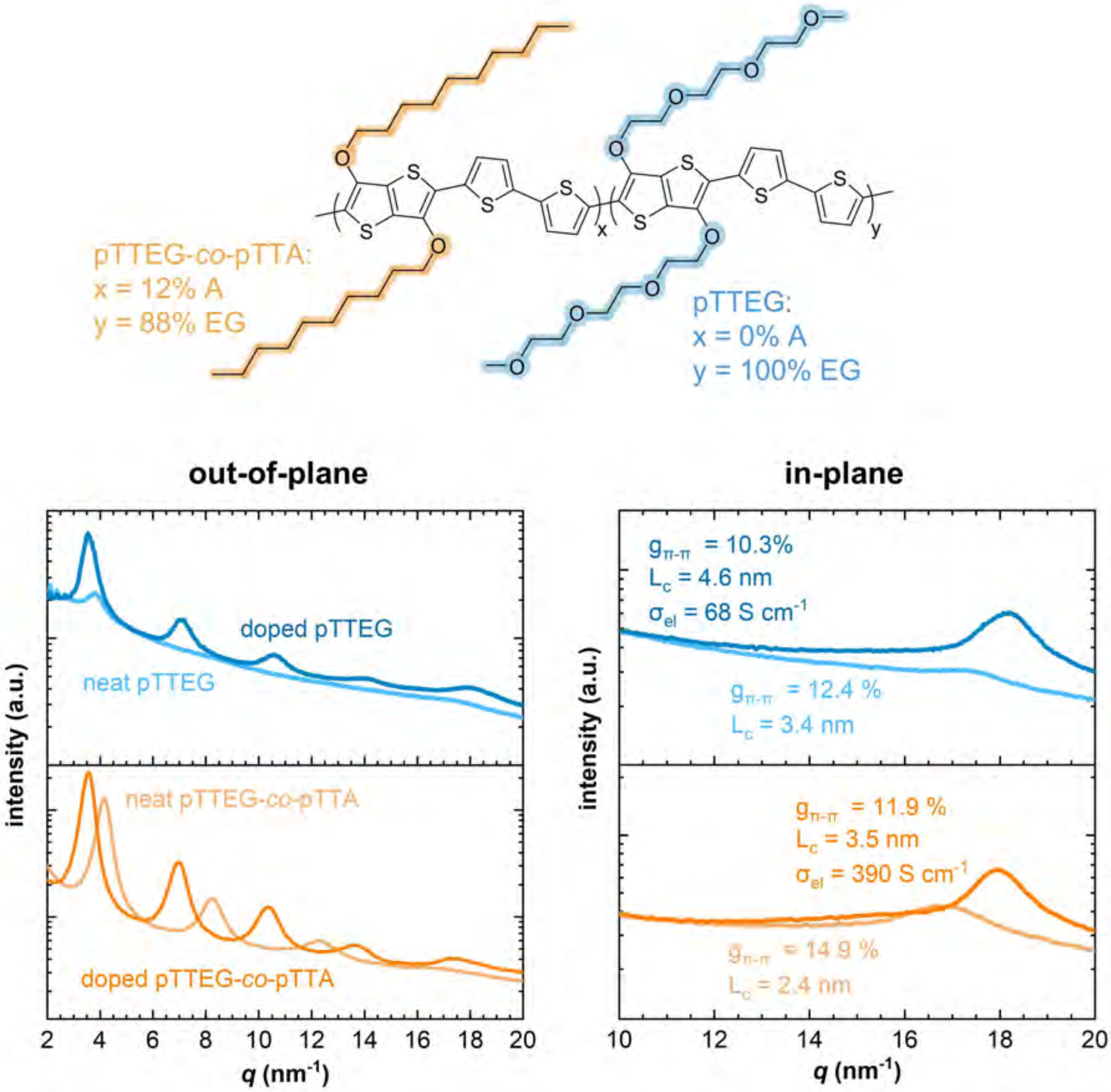

Figure 5.2. Chemical structure and GIWAXS diffractograms of pTTEG (blue) and pTTEG-co-pTTA (orange) in the neat and doped state. GIWAXS measurements were performed by Jesika Asatryan and Alberto Peinador Veiga. *Unpublished data.*

5.2 Impact of backbone: all-thiophene vs. thienothiophene

Chemical design of polymer backbone is a common strategy used to enhance the planarity of conjugated polymers, promoting a longer conjugation length and a more ordered nanostructure. Here, the effect of backbone chemical structure on polymer nanostructure and charge transport is investigated for two copolymers: an all-thiophene and a thienothiophene based polymer, p($g_3$2T-T) and p(g_3TT-T2), both having triethylene glycol side chains (see Figure 5.3 for chemical structure).

GIWAXS diffraction measurements of the neat polymer films revealed that p(g_3TT-T2) exhibits a high degree of solid-state order and an edge-on texture, as evidenced by the out-of-plane $h00$ diffraction peaks, at $q_{100} \approx 4.2$ nm^{-1}, $q_{200} \approx 8.4$ nm^{-1}, $q_{300} \approx 12.5$ nm^{-1}, and an in-plane q_{010} diffraction at $q \approx 17.1$ nm^{-1}, indicating π-stacking. (Figure 5.3). Instead, p($g_3$2T-T), as described in Section 5.1, shows limited π-stacking with a weak in-plane q_{010} diffraction peak on top of a broad amorphous halo at $q \approx 15$ nm^{-1}. Despite the enhanced solid-state order induced by chemical doping, the doped polymers show a similar structural trend as in their neat state, with p(g_3TT-T2) showing a highly ordered microstructure and p($g_3$2T-T) showing an amorphous halo but now a clear π-stacking peak. I attribute the greater solid-state order observed in case of both neat and doped p(g_3TT-T2) to the presence of the planar and rigid thienothiophene (TT) unit, in contrast to the bithiophene (2T) unit in p($g_3$2T-T).

Sequential doping of p(g_3TT-T2) with 10 mM F_4TCNQ in AcN solution induces an expansion of the unit cell along the side chains and a reduction of the π-stacking distance, as evidenced by the shift of the out-of-plane $h00$ diffraction peaks to lower q values and the in-plane q_{010} diffraction to higher q values. This suggests that dopant counterions intercalate between the side chains in the ordered polymer domains, as indicated by the increase in lamellar spacing from 14.8 Å to 17.7 Å for the neat and doped polymer, respectively. Moreover, sequential doping of p(g_3TT-T2) with dopants of different sizes, such as Magic Blue, H-TFSI, LiNFSI, results in different lamellar distances, i.e. 16.5 Å, 17.9 Å, and 21.5 Å, respectively (Figure 5 in paper V). This confirms both the presence of dopant counterions between the side chains and the influence of dopant size on the polymer nanostructure. The electrical conductivity σ_{el} of p(g_3TT-T2) doped with F_4TCNQ is 104 ± 19 S cm^{-1}.

Interestingly, p($g_3$2T-T) co-processed with 20 mol% of F_4TCNQ shows no shift of the diffraction peaks, indicating that the polymer unit cell remains unaffected by doping and by the presence of counterions. This suggests that the dopant counterions do not intercalate within ordered domains of the polymer. Instead, they are likely located in the amorphous regions. A similar behavior was reported for $SbCl_6^-$ counterions (from Magic Blue) in P3HT, which resulted in an increased distance between the polarons on polymer backbone and the counterions, which in turn reduced Coulombic interactions, enhancing the charge carrier mobility.[89, 110, 111] The electrical conductivity σ_{el} of p($g_3$2T-T) co-processed with 20 mol% of F_4TCNQ is 830 ± 15 S cm^{-1}.

The higher electrical conductivity of doped p($g_3$2T-T) despite its lower degree of solid-state order compared to p(g_3TT-T2) suggests that charge-carrier transport is influenced not only by the polymer nanostructure but also by additional factors, such as Coulombic interactions and polaron delocalization, which are important to consider.

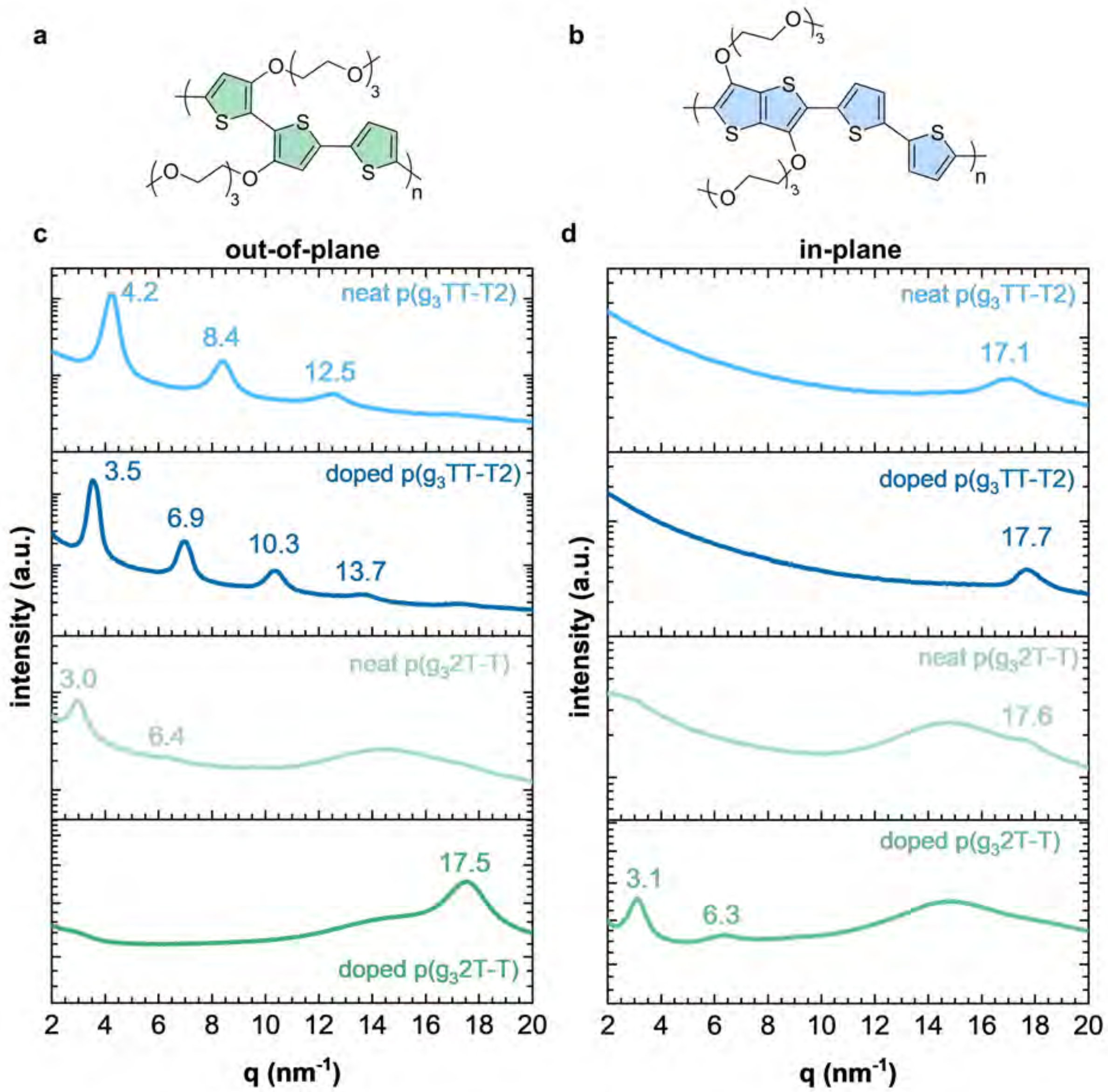

Figure 5.3. a, b) Chemical structure of p($g_3$2T-T) and p(g_3TT-T2). c, d) Out-of-plane and in-plane GIWAXS 1D line cuts of neat and doped p(g_3TT-T2) (blue) and p($g_3$2T-T) (green). GIWAXS measurements were performed by Jesika Asatryan.

5.3 Polymer chain alignment by high temperature rubbing

The influence of post-processing techniques on microstructure and charge transport was investigated for p($g_3$2T-T). High-temperature rubbing was chosen as the post-processing method, a well-established technique for controlling in-plane orientation and solid-state ordering within polymer thin films.[50]

Thin films of p($g_3$2T-T) were doctor bladed onto glass substrates and then subjected to high temperature rubbing. This process consists of a translating hot plate set at a temperature above the glass transition temperature of the polymer but below its melting point, along with a rotating cylinder covered with a microfiber cloth in contact with the polymer thin film, inducing uniaxial alignment in the translating direction (Figure 5.4a). p($g_3$2T-T) films were rubbed at a relatively low temperature of 55 ºC, significantly lower than the temperatures exceeding 150 ºC typically used to uniaxially align P3HT and PBTTT.[82, 98] This lower rubbing temperature is possible due to the low glass transition temperature of -36 ºC (Section 6) and its low degree of order at room temperature (Section 5.2). The polymer films were sequentially doped with F_4TCNQ solution at varying concentrations, ranging from 0.01 to 1 g L^{-1}, using the incremental concentration doping (ICD) procedure introduced by Vijayakumar *et al.*, which results in high doping levels.[112]

Polarized UV−vis−NIR spectroscopy was used to characterize the degree of alignment of polymer films (Figure 5.4). The absorption of neat p($g_3$2T-T) is considerably stronger parallel to the rubbing direction, with a maximum dichroic ratio $\frac{A_{\parallel}}{A_{\perp}}$ of 7.4 at 666 nm, confirming the uniaxial alignment of the polymer backbone. Upon sequential doping, the spectrum recorded for POL ∥ R indicates that the neutral absorption band of the polymer is bleached along with the appearance of polaronic bands in the NIR region and weak absorption bands of F_4TCNQ anions. Instead, the spectrum recorded for POL ⊥ R shows stronger bands of F_4TCNQ^- anions at around ~ 770 and ~ 870 nm and of neutral F_4TCNQ at around ~ 380 nm.[92] The higher absorption of F_4TCNQ anions in POL ⊥ R orientation suggests that the dopant counterions preferentially align with their long axis perpendicular to the polymer chain direction of p($g_3$2T-T), as previously observed for P3HT.[98]

The electrical conductivity is considerably higher along the rubbing direction (Figure 5.4d), reaching values of up to $\sigma_{el,\parallel}$ ~ 7300 S cm^{-1}, compared to $\sigma_{el,\perp}$ ~ 1300 S cm^{-1} and $\sigma_{el,not\ rub}$ ~ 3900 S cm^{-1} for p($g_3$2T-T) doped with 1 g L^{-1} F_4TCNQ solution. In contrast, the Seebeck coefficient displays a low degree of in-plane anisotropy with values below 10 μV K^{-1} for most of the isotropic and anisotropic doped samples (Figure 5.4e).

The different values of electrical conductivity for different directions highlight the significant influence of uniaxial chain alignment techniques on charge transport properties.

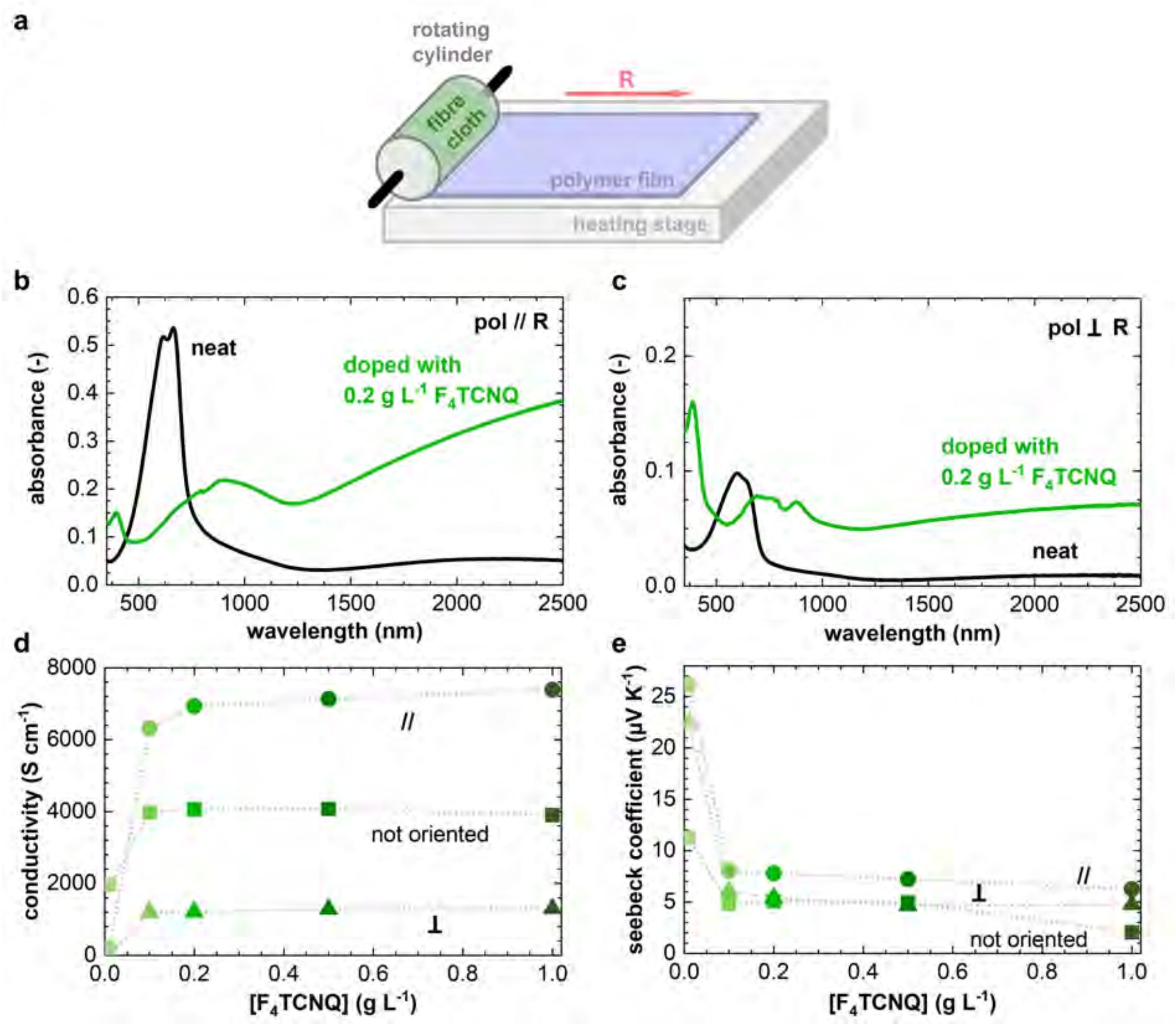

Figure 5.4. a) Schematic of the high-temperature rubbing technique. b, c) UV–vis–NIR spectra with light polarization oriented parallel and perpendicular to the chain direction of neat and doped $p(g_32T\text{-}T)$. d, e) Electrical conductivity and Seebeck coefficient vs. F_4TCNQ concentration of isotropic and anisotropic samples. All experiments and measurements were performed together with Shubhradip Guchait in the lab of Martin Brinkmann at CNRS in Strasbourg. No error bars are shown because only one sample per dopant concentration was measured. The film thickness was estimated to be circa 55 nm from the absorption peak of the neat polymer, assuming a linear relationship between the molar extinction coefficient of the polymer and its thickness, according to 0.1 abs = 10 nm. *Unpublished data.*

5.4 Doping level

The degree of order is influenced not only by side-chain length and type, backbone conformation and post-processing techniques but also by the amount of dopant (paper I).

Indeed, co-processing p($g_4$2T-T) with different mol% of H-TFSI results in different degrees of structural order (Figure 5.5).

The intensity of the out-of-plane $0h0$ diffraction peak associated with π-stacking increases with the addition of up to 7 mol% H-TFSI to p($g_4$2T-T), and then decreases together with a shift to lower q values at higher H-TFSI concentrations. Interestingly, p($g_4$2T-T) films that contain a large amount of H-TFSI (25 and 40 mol%) give rise to GIWAXS diffractograms that are more comparable to neat p($g_4$2T-T) with an out-of-plane q_{100} diffraction and a weak q_{010} diffraction. This indicates that the degree of π-stacking also depends on the amount of dopant counterions present in the sample: π-stacking is favored at low dopant concentrations, while high dopant concentrations are detrimental to π-stacking. A lower degree of order at high dopant concentrations may indicate that polaron/counterion interactions reduce the ability of the polymer to order.[20]

The electrical conductivity of p($g_4$2T-T) co-processed with H-TFSI increases with the dopant concentration up to 25 mol%, where it reaches a conductivity of ~ 20 S cm^{-1}, followed by a decrease to ~ 5 S cm^{-1} for higher H-TFSI mol% values (Figure 5.5). The electrical conductivity decreases as the dopant amount reaches 40 mol% H-TFSI despite a further increase in the oxidation level, as evidenced by UV-vis spectroscopy (Figure 5.5), suggesting a reduced charge-carrier mobility due to a lower degree of order.

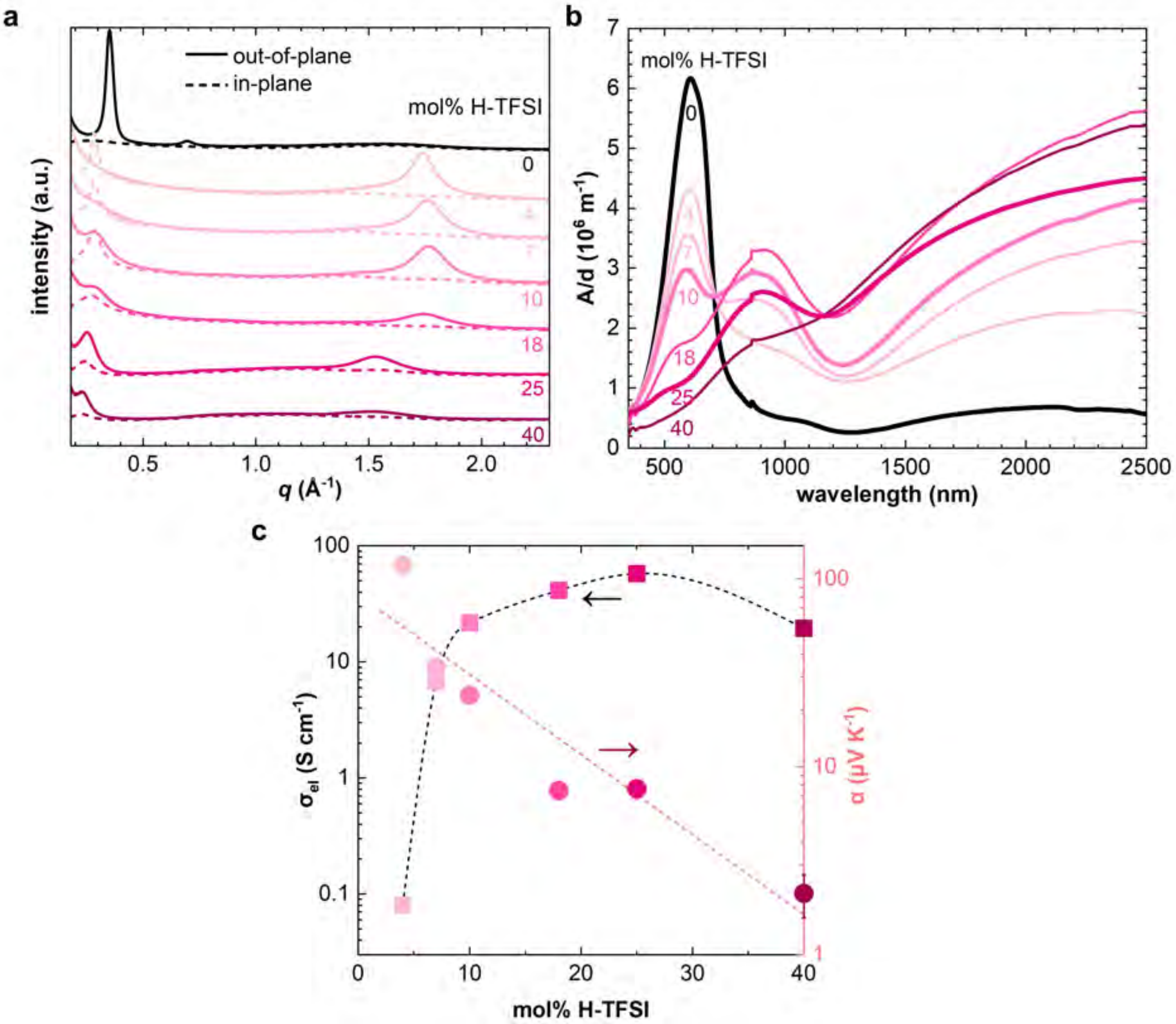

Figure 5.5. a) GIWAXS diffractograms of p($g_4$2T-T) co-processed with different amounts of H-TFSI. b) UV-vis absorption spectra and c) electrical conductivity σ_{el} and Seebeck coefficient α of p($g_4$2T-T) co-processed with different amounts of H-TFSI. GIWAXS measurements were performed by Sara Marina. Adapted with permission from ref [20] published by RSC.

6 Effect of doping on the mechanical properties

Chemical doping can strongly alter the nano- and microstructure (Section 5) of conjugated polymers[18] and these alterations can change their mechanical properties through different effects including plasticization, stiffening of the polymer backbone, ionic interactions, a change in the degree of order, and a change in free volume (Section 2.2).

The presence of dopant counterions between the side chains of conjugated polymers can induce a plasticization effect by reducing the interchain interactions. For example, regioregular P3HT (regioregularity: 95%) experiences a plasticization effect when doped with ethylbenzene sulfonic acid (EBSA), showing a decrease in T_g from 30 to 15 °C and, hence, a decrease in elastic modulus at room temperature from 900 to 345 MPa.[113] A similar effect occurs in case of free-standing and tensile-drawn films of P3HT when doped with the molybdenum dithiolene complex $Mo(tfd\text{-}COCF_3)_3$, yielding an elastic modulus of 0.4 GPa (compared with 1.1 GPa prior to doping).[51]

Conversely, chemical doping can increase the elastic modulus by enhancing π-stacking and hence the degree of order. This effect has been observed especially in case of softer conjugated polymers. For instance, p($g_4$2T-T), with an elastic modulus of 8 MPa at room temperature, can experience a 29-fold increase in modulus up to 232 MPa along with a change in T_g from -43 to 3 °C when doped with 30 mol% F_4TCNQ.[63]

I investigate the mechanical properties of conjugated polymers using dynamic mechanical thermal analysis (DMTA), differential scanning calorimetry (DSC) and tensile deformation to address hypotheses 3 and 4 (Section 3). Section 6.1 and 6.2 focus on how the backbone chemical structure and chemical doping influence the mechanical properties of a polythiophene-based copolymer with oligoether side chains. Moreover, the mechanical properties of an n-type conjugated polymer without side chains are explored in Section 6.3, addressing hypothesis 5 of this thesis.

6.1 Effect of the polymer backbone on the mechanical properties

The relaxation temperatures of p($g_3$2T-T) and p(g_3TT-T2) were analyzed to investigate the effect of the backbone structure.

DMTA in tensile mode at a frequency of 1 Hz of neat p($g_3$2T-T) supported by a glass fiber mesh (Figure 6.1a) indicates a softening of the material upon heating from −80 to 50 °C, as evidenced by a decrease in E', a peak in E'' at −36 °C, a peak in tanδ at −30 °C, which I assign to the onset of a relaxation process of the polymer chain.[64] I performed DMTA of neat p($g_4$2T-T) and p($g_6$2T-T) to explore the effect of side-chain length on the relaxation temperature of the polymer. The resulting DMTA thermographs (Figure S9 in paper II) indicate similar values of −41 and −43 °C, both taken from the peak in E'', for p($g_4$2T-T) and p($g_6$2T-T), respectively.[64] The increase in the side-chain length from triethylene glycol to tetra- or hexaethylene glycol, corresponding to a side-chain fraction of 57, 63 and 71 wt% respectively, only slightly reduces the relaxation temperature, which is similar to the behavior observed for poly(3-alkylthiophene)s (P3ATs) with long alkyl side chains (e.g., decyl and dodecyl with a side-chain fraction of 63 and 68 wt%, respectively).[66, 68]

Since p(g_x2T-T) polymers have the same backbone, I expected that they would show a similar T_α, corresponding to the relaxation of the backbone. At the same time, since the loss modulus peak of p(g_x2T-T) occurs at the relaxation temperature of oligoether side chains T_β, it is feasible that the backbone and side-chain relaxation of p(g_x2T-T) polymers overlap, resulting in a single transition in the DMTA plot, which I refer to as $T_{\alpha/\beta}$. This result may be attributed to an "internal plasticization" effect induced by long and flexible side chains, which led to a decrease in the temperature associated with the backbone relaxation, as reported for regiorandom P3ATs with long alkyl side chains.[68, 114]

DMTA in tensile mode at a frequency of 1 Hz of free-standing samples of neat p(g_3TT-T2), processed via solid-state pressing at 180 °C, reveals two distinct transitions upon heating the material from −80 to 60 °C (Figure 6.1b), suggesting the occurrence of distinguishable relaxation processes. A first sub-glass transition T_β is observed at -50 °C, as evidenced by a decrease in E' from above to below 1000 MPa, along with peaks in E'' and tanδ. This transition is likely associated with relaxation of the oligoether side chains, given the similar low T_g of -50 °C reported for poly(ethylene oxide) (PEO).[115] A second transition appears at T_α of -5 °C indicated by a further peak in tanδ. This transition is attributed to main chain relaxation, i.e. the polymer backbone. Specifically, I propose that T_α corresponds to the relaxation of the bithiophene units, since the T-TT linkage likely experiences sulfur-oxygen interactions. Further experiments are required to validate this hypothesis.

Interestingly, incorporating a rigid unit, such as the thienothiophene-based monomer g_3TT, in the backbone not only enhances the degree of solid-state order (Section 5.2) but also introduces distinct segmental backbone relaxation compared to a fully thiophene-based backbone. Similar behavior was observed in case of a poly(benzodithiophene-*alt*-dithienyl difluorobenzotriazole) type copolymer with tri- and tetraethyelene glycol side chains on the benzodithiophene (BDT) donor and benzotriazole acceptor moieties, respectively, which exhibits a relaxation process around -40 °C dominated by side chains followed by relaxation of the backbone at 21 °C.[116] Likewise, p(g_3TT-T2) displays a similar trend, with a sub-glass transition T_β at -50 °C and T_α at -5 °C, suggesting a relaxation process associated with the side-chains followed by backbone relaxation.

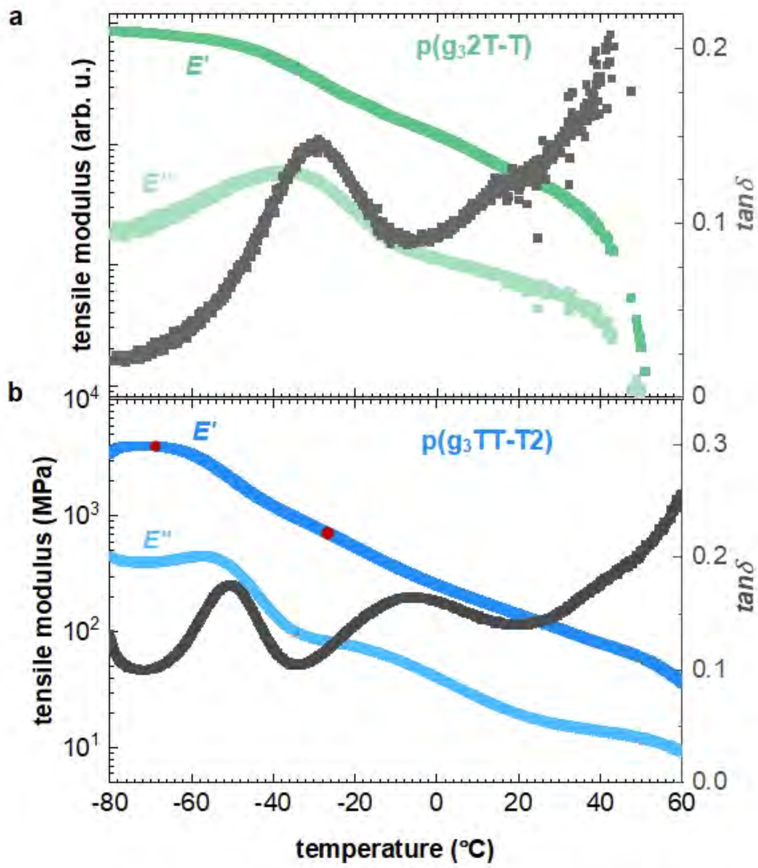

Figure 6.1. DMTA thermograms showing the storage modulus (E′, dark color), loss modulus (E″, light color) and tanδ (grey) measured for: a) a glass mesh supported film of neat p($g_3$2T-T) (adapted with permission from ref [64] published by ACS Publications) and b) a free-standing film of neat p(g_3TT-T2).

6.2 Effect of chemical doping on the mechanical properties

In Section 5 I have discussed how chemical doping enhances the order of thin films based on thiophene-based copolymers with oligoether side chains. Specifically, an increase in π-stacking is observed upon chemical doping. Given these structural changes, I argued that the mechanical properties would also be influenced by chemical doping. To investigate this hypothesis, I performed DMTA and tensile deformation experiments on free-standing samples of p($g_3$2T-T) co-processed with 20 mol% F_4TCNQ (paper II) and p(g_3TT-T2) sequentially doped with 10 mM F_4TCNQ solution in dry acetonitrile (paper V).

For both polymers, an increase in the temperature above which relaxation processes occur was observed. Co-processing p($g_3$2T-T) with 20 mol% F_4TCNQ considerably increases the peak in tanδ from -30 °C to 5 °C (Figure 6.2a). A similar effect was reported for F_4TCNQ-doped p($g_4$2T-T) by Zokaei *et al.*.[63]

Likewise, in case of p(g_3TT-T2), the tanδ peak that I associate with T_β shifts from -50 °C to -3 °C when comparing the neat and doped polymer (Figure 6.2b). Interestingly, the DMTA thermograph of doped p(g_3TT-T2) exhibits a single transition, suggesting that only one dominant or, alternatively, two overlapping relaxation process occur within the temperature range of -80 °C to 60 °C.

This increase in $T_{\alpha/\beta}$ for doped p($g_3$2T-T) and in T_β for doped p(g_3TT-T2) can be attributed to various factors, such as doping-induced π-stacking, a change in the rigidity of the backbone upon oxidation as well as a change in the available free volume to chain motion due to the presence of dopant counterions. For instance, in case of p(g_3TT-T2) the dopant counterions intercalate between the side chains in the ordered polymer domains, as indicated by the increase in lamellar spacing upon doping (Section 5.2). Hence, I argue that the presence of counterions may reduce the free volume fraction available for side-chain relaxation, leading to a higher sub-glass transition temperature T_β. Moreover, interactions between dopant counterions and semiconductor can also contribute to an increase in T_β, above which the side chains can relax.

The enhanced solid-state order induced by doping, along with the presence of dopant counterions, has a significant impact on the storage modulus E'. In case of both doped polymers, E' shows a smaller decrease in magnitude when comparing $E'(T_\beta - 20°\text{C})/E'(T_\beta + 20°\text{C})$ of neat and doped polymer. In case of p(g_3TT-T2), the estimated ratio is approximately 5.5 for the neat and ~ 3 for the doped polymer. Moreover, E' shows only a weak temperature dependence above the transition temperatures observed with DMTA, suggesting that doping enhances the stiffness of these materials. Further studies are needed to investigate how the stiffness is influenced by oxidation level and ionization efficiency at different temperatures.

Tensile tests at room temperature of free-standing samples confirmed an increase in stiffness upon chemical doping. For p(g$_3$2T-T) doped with 20 mol% F_4TCNQ, the Young's modulus increased by a factor of 10, reaching a value of $E = 826 \pm 141$ MPa, while maintaining a similar elongation at break ε_{break} (Figure 6.2c). In case of p(g$_3$TT-T2) sequentially doped with F_4TCNQ, the Young's modulus increased by a factor of 20 up to $E = 693 \pm 185$ MPa, along with a decrease in ε_{break} (Figure 6.2d).

I expect the increase in the degree of order to benefit charge transport and to increase the Young's modulus of the material, leading to correlation between electrical and mechanical properties (Section 2.3).

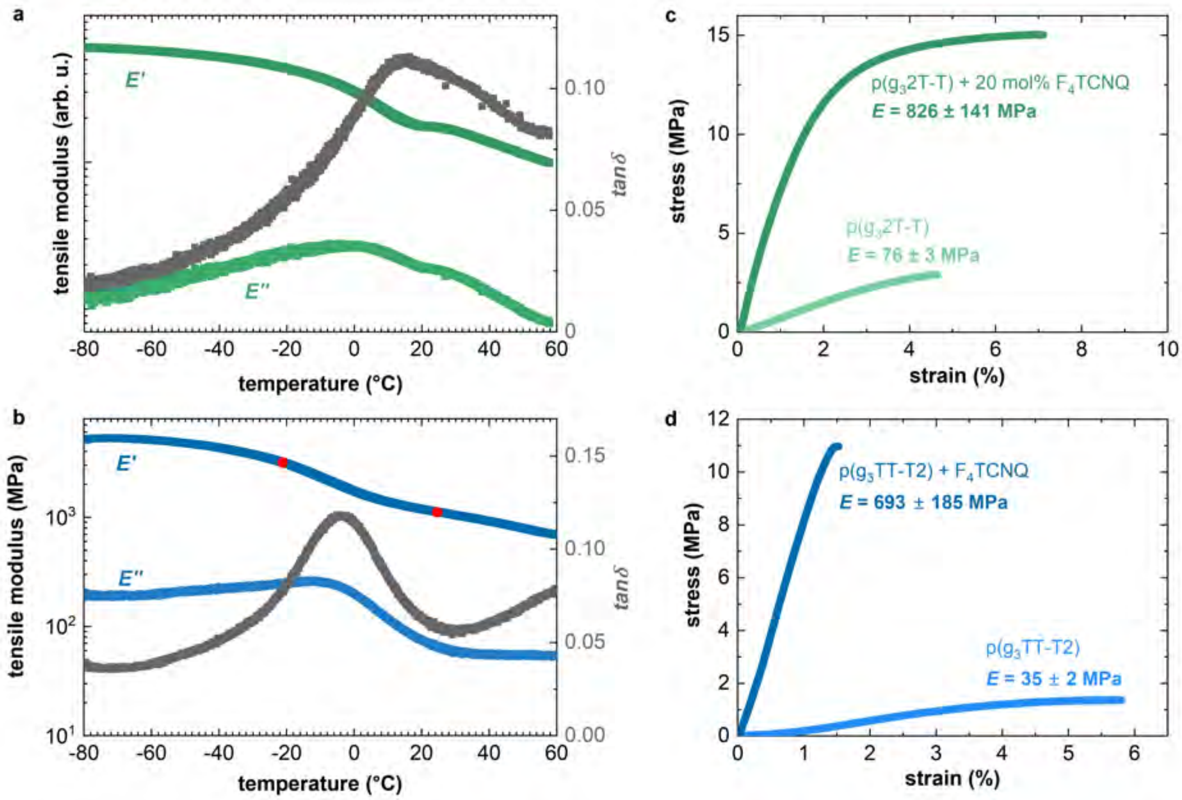

Figure 6.2. DMTA thermograms (left) and stress-strain curves (right) showing E', E'' and tanδ measured for a) a glass mesh supported film of p(g$_3$2T-T) co-processed with 20 mol% of F_4TCNQ (green) and for b) a free-standing film of p(g$_3$TT-T2) sequentially doped with F_4TCNQ (blue). Adapted with permission from ref [64] published by ACS Publications.

Given that the degree of solid-state order is influenced by the amount of dopant introduced (Section 5.4), the change in $T_{\alpha/\beta}$ of p(g$_4$2T-T) co-processed with different amounts of H-TFSI was studied by DSC at a scan rate of 10 °C min^{-1} (paper I). The $T_{\alpha/\beta}$ increases with mol% of

H-TFSI, reaching the highest value of -32 °C (starting from -59 °C in case of the neat polymer) for aged material doped with 40 mol% H-TFSI (Figure 6.3).[20]

The increase in $T_{\alpha/\beta}$ observed in case of p(g$_4$2T-T) when co-processed with H-TFSI is less pronounced compared to the increase achieved through doping with F$_4$TCNQ (Figure 6.3). This difference is thought to be due to a different oxidation level, changes in the conformation of the polymer, possibly due to protonation in case of doping with H-TFSI, as well as the location of the anion relative to the polymer backbone. Indeed, as suggested by MD simulations performed by Prof. Igor Zozoulenko and his team, TFSI anions are positioned further away from the polymer backbone than F$_4$TCNQ anions.[20, 63] The difference in the $T_{\alpha/\beta}$ of doped polymers suggests that different dopant counterions and different oxidation levels can yield different outcomes with regard to the mechanical properties.

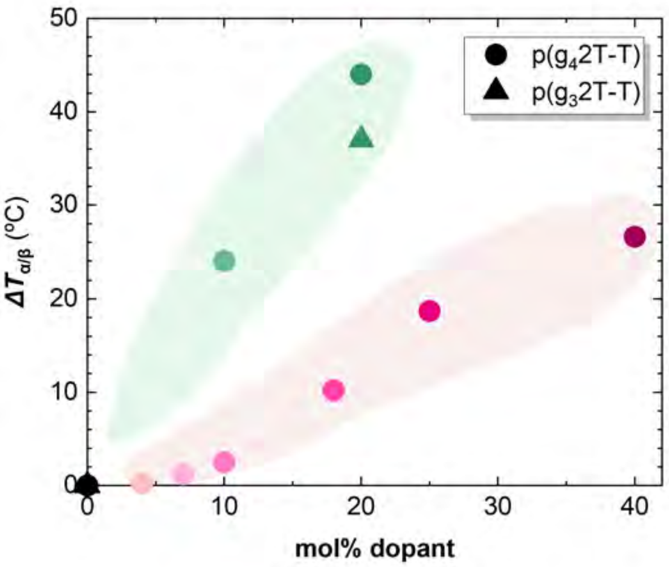

Figure 6.3. Transition temperature difference $\Delta T_{\alpha/\beta}$ vs. dopant concentration of p(g$_3$2T-T) and p(g$_4$2T-T) co-processed with H-TFSI or F$_4$TCNQ. The $\Delta T_{\alpha/\beta}$ is calculated according to $T_{\alpha/\beta,doped} - T_{\alpha/\beta,neat}$, where $T_{\alpha/\beta,neat}$ is -36 °C for p(g$_3$2T-T) (measured by DMTA), -41 °C for p(g$_4$2T-T) (measured by DMTA), and -59 °C for p(g$_4$2T-T) (measured by DSC). DSC measurements were carried out by Sepideh Zokaei and Sandra Hultmark.

I further investigated the impact of doping on T_β of p(g$_3$TT-T2), which was doped by various doping mechanisms, including redox doping (F$_4$TCNQ, Magic Blue), acid mediated doping by oxygen (H-TFSI), and PCET in the presence of aqueous LiNFSI electrolyte (paper V). Free-standing samples of neat polymer were prepared by hot pressing and sequential doping, which involved immersing them in the dopant solution for 4 – 24 hours.

Regardless of the doping mechanism, all samples exhibit an increase in T_β upon doping (Figure 6.4a), similar to F_4TCNQ-doped p(g_3TT-T2) described in Section 6.2. However, the magnitude of change in T_β differs depending on the specific dopant counterion. For instance, in case of H-TFSI-doped p(g_3TT-T2), T_β increased slightly to -44 °C, i.e. just 6 °C higher than T_β of the neat polymer. While for p(g_3TT-T2) doped with PCET (with NFSI as the counterion) and Magic Blue, T_β increased to -34 °C and -25 °C, respectively. The most pronounced increase was observed in case of p(g_3TT-T2) doped with F_4TCNQ, where T_β reached a value up to -3 °C. This behavior suggests differences in free volume due to the presence of different counterions. To prove this hypothesis, the fractional free volume in doped samples was calculated by Dr. Meghna Jha (see paper V for calculation details), and it is found to decrease with increasing side-chain relaxation temperature T_β (see Figure 6c in paper V). This correlation can be understood in terms of the energy that is required for side-chain relaxation to occur, which depends on the free volume that is available for the motion of side chains.

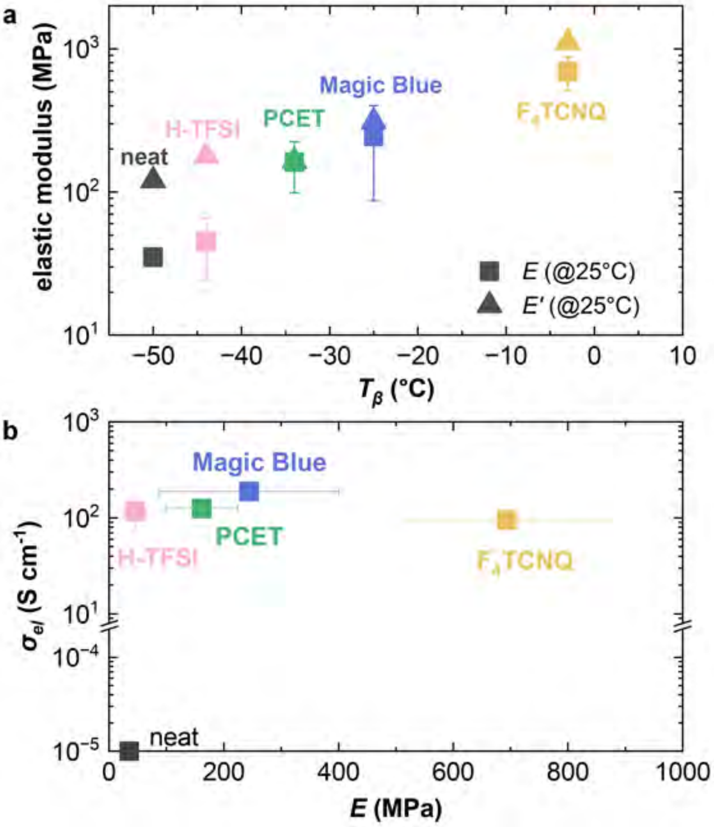

Figure 6.4. a) Elastic modulus vs. T_β of free-standing samples and b) σ_{el} vs. E of p(g_3TT-T2) doped by F_4TCNQ, Magic Blue, H-TFSI, and through PCET (with NFSI as the counterion).

Interestingly, the storage and Young's moduli at room temperature of doped samples followed the same increasing trend with different counterions as T_β (Figure 6.4a). This suggests that the stiffness at room temperature correlates with T_β and thus depends on the ability of side chains to relax.

Doping p(g$_3$TT-T2) with different counterions allows to achieve samples with a similar σ_{el} ≈ 100 S cm^{-1}, but a significantly different Young's modulus with values varying from E = 0.05 to 0.7 GPa at room temperature (Figure 6.4b). This suggests that selecting a specific doping mechanism and dopant counterion allows to partially decouple the often-observed correlation between σ_{el} and E.

6.3 Mechanical properties of a conjugated polymer without side chains

In paper IV, the mechanical properties of the recently reported n-type polymer PBFDO[117, 118] (see Figure 6.5a for chemical structure, the polymer was synthesized by Qifan Li according to ref [117]) were explored to evaluate its potential as a yarn coating material for wearable thermoelectric devices.[73] Unlike the other conjugated polymers studied in this thesis, PBFDO lacks flexible and long side chains. Hence, I anticipated that PBFDO would be a very stiff and brittle material. However, the polymer could be easily processed into free-standing films that were mechanically robust and could be handled without fracture, even at temperatures below room temperature. Bending without breaking was possible after being immersed in liquid nitrogen for a few minutes (bending radius 5 mm; Figure 6.5a).[73]

DMTA in tensile mode at a frequency of 1 Hz was used to investigate the thermomechanical behavior of free-standing PBFDO films. The tensile storage modulus E' had a value of 18 GPa at -10 °C which slightly decreased above 0 °C, to a value of, e.g., E'= 16 GPa at room temperature (Figure 6.5b). A further decrease to about 10 GPa was observed above 100 °C, accompanied by a pronounced peak in tanδ at 120 °C (Figure 6.5b).[73] DMTA thermograph indicate that PBFDO exhibits limited relaxation processes, which may absorb impact energy even below T_α resulting in a certain degree of impact toughness.[55, 119]

To explore the ductility of PBFDO in more detail, tensile deformation measurements were performed on free-standing samples. At room temperature, the polymer is stiff but nevertheless somewhat ductile (Figure 6.5c), with a E = 6.6 ± 0.9 GPa and a ε_{break} = 5.2 ± 1.1 % when measured with tensile deformation in force-controlled mode at a deformation rate of 0.01 N min^{-1}, yielding a toughness of 3.6 ± 1.1 MJ. The somewhat lower Young's modulus values compared with the storage modulus from DMTA can be attributed to the here employed low tensile deformation rate.[73]

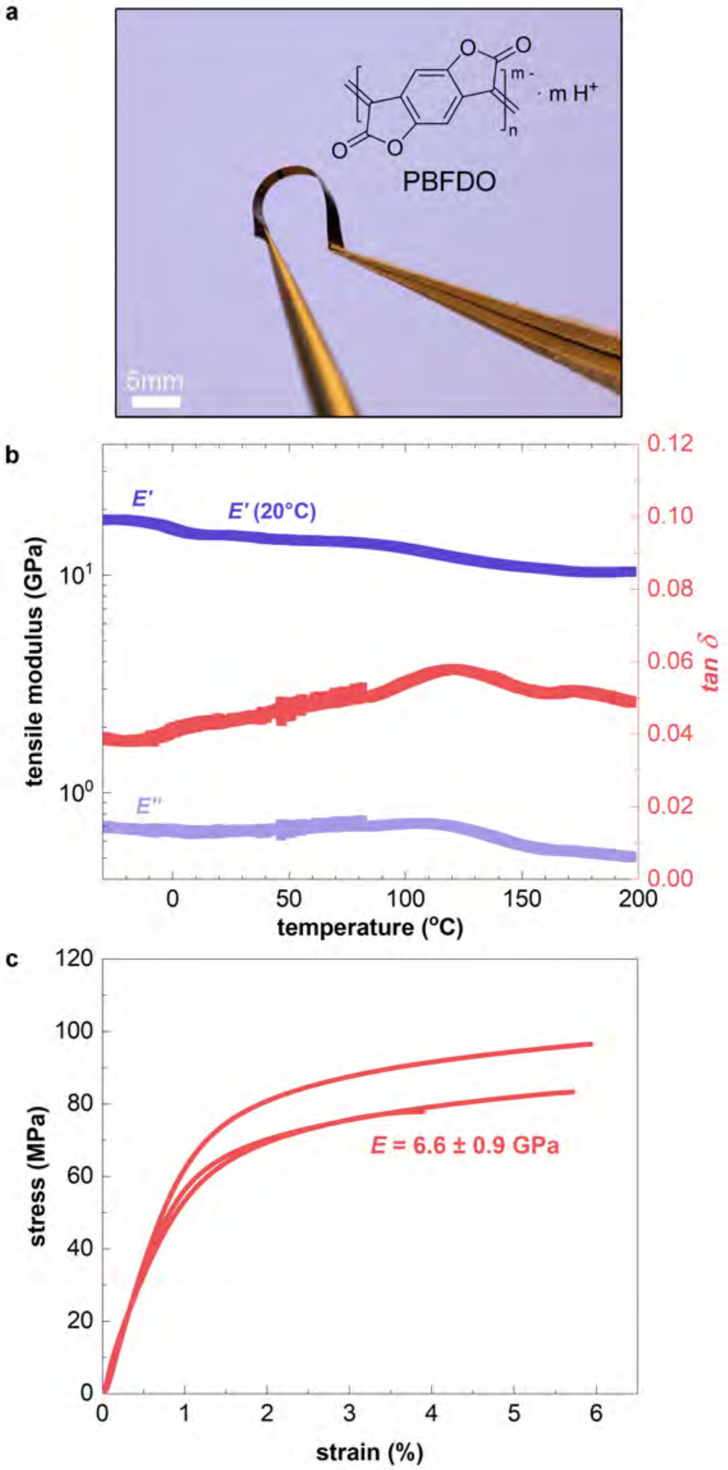

Figure 6.5. a) Chemical structure of reduced PBFDO and photograph of a bent film after being immersed in liquid nitrogen for a few minutes. b) DMTA thermographs of a free-standing film showing E', E'' and tanδ. c) Stress–strain response of three free-standing films measured by tensile deformation at 20 °C. All measurements were performed together with Qifan Li. Adapted with permission from ref [73] published by Wiley.

7 Stability of doped conjugated polymers

Organic electronic devices must have a long operating lifetime, maintaining a near "as-new" performance, e.g. electrical and thermal in case of organic thermoelectrics, as they age. In reality, this is difficult to accomplish due to degradation processes that doped conjugated polymers can experience, compromising their stability and long-term performance.

Chemical doping is a reversible process, hence there are many events that likely influence the stability of the doped state, such as neutralization of the charged state, diffusion and sublimation of dopant counterions. For instance, diffusion of dopant molecules is beneficial for achieving a uniform doping level throughout polymer films during sequential doping. However, it negatively impacts long-term stability due to dopant redistribution resulting in local variations of the doping level.[31] The diffusion behavior of dopant molecules depends on both their valency and size. Neutral dopant molecules diffuse more easily than dopant counterions, which experience Coulombic interactions with polarons on the polymer backbone.[120, 121] Furthermore, larger dopant counterions tend to have lower diffusion coefficients, as seen in the case of F_6TCNNQ anions and F_4TCNQ derivatives that feature methyl ester groups, which diffuse more slowly than F_4TCNQ anions.[112, 120]

Moreover, doped conjugated polymers are highly sensitive to exposure to air, light, and heat. Interactions with an atmosphere (e.g. air or nitrogen)[122] or an electrolyte can lead to dopant loss through sublimation or leaching. For example, many dopants are relatively small molecules with high vapor pressure, such as iodine and F_4TCNQ, and hence sublime upon heating, leading to a reduction of the doping level.[44, 123] Additionally, chemical side reactions between dopant counterions and the conjugated polymer can affect the long-term performance, as, e.g., observed in the case of F_4TCNQ and P3HT upon thermal annealing above 60 ºC, where the counterion extracts a hydrogen atom from the polymer side chain, forming a weaker dopant HF_4TCNQ.[124]

In order to develop competitive and reliable thermoelectric technologies, it is important to study and address these stability issues. Various approaches have been proposed that allow to enhance the stability of doped conjugated polymers. One of these involves using Lewis-paired dopant complexes, such as a complex of BCF and F_4TCNQ, which features a large molecular size and large binding energy. This has been shown to significantly improve the thermal stability of doped films, as demonstrated by the prolonged operational lifetime of P3HT at 100 °C in air.[26] A similar method utilizes sulfonic or bistriflimidic acid as p-dopants to enhance the thermal stability of p($g_4$2T-T) films, which retained their electronic properties after annealing at 120 °C for over 10 hours.[22]

An alternative approach focuses on exchanging small and highly reactive dopant counterions such as F_4TCNQ or iron(III) chloride ($FeCl_3$)with electrolyte anions such as TFSI through ion exchange doping (Section 1.2.2, Figure 1.3). This doping technique allows to achieve a high ionization efficiency and enhanced stability, especially when a complete anion exchange is achieved.[17, 28]

Here, I investigate the long-term electrical performance at ambient condition of three doped polymers. Moreover, the lateral drift of dopant counterions in an electric field is discussed and a method that exploits this drift to improve thermoelectric properties is presented.

7.1 Interaction with atmosphere

To study the electrical stability of p($g_3$2T-T) co-processed with 20 mol% of F_4TCNQ at ambient conditions, the thermoelectric properties were monitored over time (Figure 7.1a, paper II). The doped polymer is sensitive to air, as evidenced by a drop in electrical conductivity within the first 24 hours of ageing, thus leading to a decrease in the thermoelectric performance. After an initial drop in σ_{el}, thin films of p($g_3$2T-T) co-processed with F_4TCNQ retained a high $\sigma_{el} \approx 200$ S cm^{-1} for three months of ageing at ambient conditions.

The initial drop in electrical conductivity can be attributed to partial dedoping that occurs at ambient conditions. UV-vis spectrum of a 3-months old sample shows the reappearance of the absorption peak of the neat polymer at 2.1 eV, along with a reduction in the intensity of the polaronic absorption bands in the near infrared region (Figure 7.1b). Additionally, the peak at 3.2 eV, assigned to neat F_4TCNQ, decreases and shifts to 3.5 eV, which I associate to the gradual sublimation of the dopant at ambient conditions and to the formation of F_4TCNQ dianions, which occurs only at low doping levels.[63, 92] To verify the presence of dopant dianions, I recorded a transmission FTIR absorbance spectrum of a 3-months old sample, which exhibits the characteristic absorption peak of F_4TCNQ dianions (Figure 7.1c).

I attribute the promising level of long-term stability to the presence of F_4TCNQ dianions, which likely experience a stronger Coulomb interaction with the polymer compared to F_4TCNQ

anions, hence enhancing the diffusion resistance, similarly to the high stability achieved by doping an n-type polymer with tetravalent counterions, as reported by Koch *et al.*.[121]

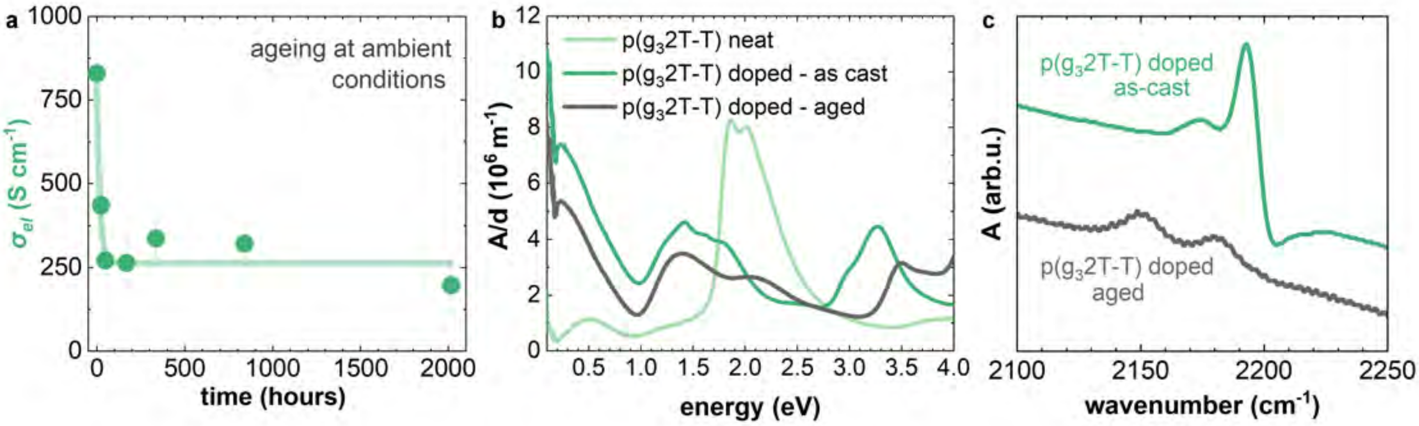

Figure 7.1. a) Electrical conductivity vs. ageing time of p(g$_3$2T-T) co-processed with 20 mol% of F$_4$TCNQ at ambient conditions. b) UV-vis and transmission FTIR absorbance spectra, with the absorbance A normalized by the film thickness d, of neat p(g$_3$2T-T) and films doped with 20 mol% F$_4$TCNQ, as-cast and aged at ambient conditions for 3 months. c) Transmission FTIR absorbance spectra of doped p(g$_3$2T-T) films, as-cast and aged at ambient conditions for 3 months. Adapted with permission from ref [64] published by ACS Publications.

Unlike the initial drop in electrical conductivity observed in case of p(g$_3$2T-T) co-processed with 20 mol% of F$_4$TCNQ, p(g$_4$2T-T) co-processed with H-TFSI exhibits an increase in conductivity upon exposure to air (Figure 7.2, paper I).[20]After 2 days of ageing at ambient conditions films exhibited a higher σ_{el} than as-cast films reported by Hofmann *et al.*.[22] The observation that a high σ_{el} is only obtained when the material is exposed to air can be explained with acid mediated oxidation of the polymer through O_2.[19]

To investigate the effect of ageing on the stiffness and elongation at break of neat and doped p(g$_4$2T-T), I carried out tensile deformation tests of as-cast free-standing samples and samples aged for 14-days (Figure 7.2). For as-cast samples the elastic modulus increases up to E = 90 $\pm$ 5 MPa at 18 mol% H-TFSI, and then decreases at higher concentrations of H-TFSI. Aged samples display a similar trend with the Young's modulus reaching a maximum of 164 ± 11 MPa at 18 mol% H-TFSI, followed by a drop in modulus at higher concentrations. The Young's modulus of aged samples is higher than for as-cast ones, especially at H-TFSI concentrations higher than 9 mol%, indicating a gradual modification of the nanostructure due to the slow kinetics of the doping process. An electrical conductivity of 40 ± 5 S cm^{-1} was measured for a several-months old thick sample doped with 18 mol% H-TFSI, that was previously used for mechanical testing, which confirms that bulk samples can retain a high conductivity over long periods of time.[20]

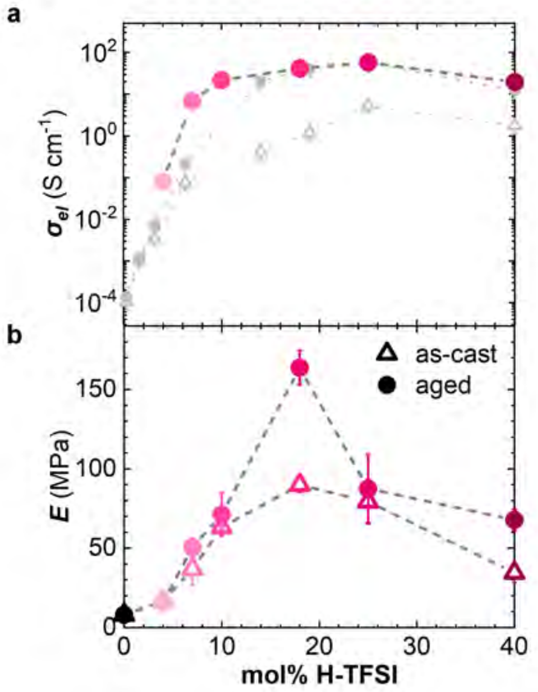

Figure 7.2. a) Electrical conductivity and b) Young's modulus of as-cast (open triangles) and aged (filled circles) samples of doped p(g$_4$2T-T) as a function of mol% H-TFSI. Grey symbols: data from ref [22]. Adapted with permission from ref [20] published by RSC.

In paper IV, the n-type polymer PBFDO, featuring high electrical conductivity and high air stability,[117] was used to coat silk yarn, resulting in conductive yarns for thermoelectric textiles (Section 8 for more details). To assess the long-term stability of PBFDO coated yarn, the electrical resistance was occasionally measured during storage at ambient conditions. Notably, the electrical conductivity remained almost constant over a span of 24 months when stored at ambient conditions (Figure 7.3), which indicates exceptional stability of the yarn compared to other types of n-type polymers.[125] It was extrapolated that the PBFDO coated yarn would lose 50% of its initial conductivity after 3.7 ± 0.8 years.

The thermoelectric properties of PBFDO coated silk yarn were optimized through partial oxidation, i.e. dedoping, by exposing the polymer to the strong oxidizing agent Magic Blue,[126] commonly used a p-type dopant.[83, 89] Oxidized yarn sections displayed a decrease in $\sigma_{el,\ eff}$, while α became more negative (see Figure S11 in paper IV), leading to an overall increase in the power factor up to one order of magnitude from about 0.5 to 5 µW m^{-1} K^{-1}. However, the thermoelectric properties of partially oxidized PBFDO yarn were not stable at ambient conditions, likely due to gradual reduction of the material by moisture in the air.

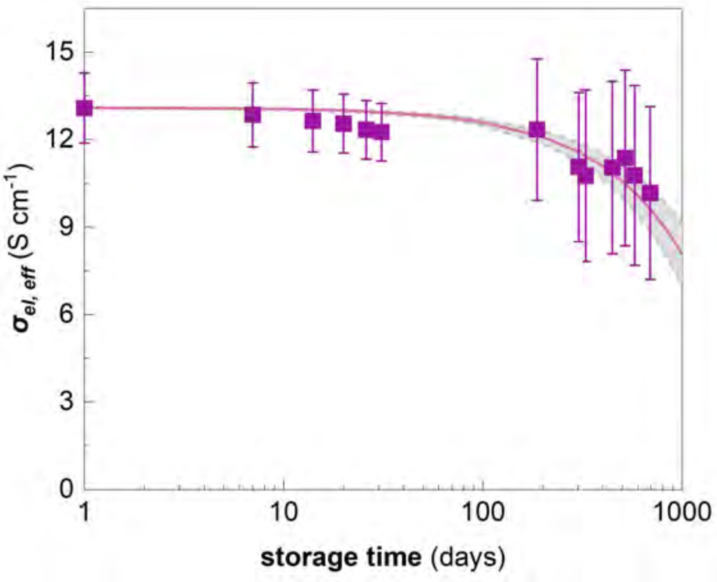

Figure 7.3. Effective electrical conductivity $\sigma_{el,\ eff}$ of PBFDO coated yarn (purple squares) and ageing prediction (grey area) as a function storage time at ambient conditions. Adapted with permission from ref [73] published by Wiley with data points for t > 500 days added.

7.2 Doping gradients

The movement of dopant counterions due to diffusion or drift in an electric field can have a negative effect on the long-term electrical performance of doped conjugated polymers. However, the drift of dopant counterions within polymer films can also be harnessed to create lateral doping gradients. Indeed, dopant counterions can drift in the presence of an electric field, accompanied by a redistribution of charge carriers. For example, F_4TCNQ anions undergo lateral drift in P3HT thin films if a strong electric field of 3 V mm^{-1} is applied, leading to a doping gradient.[127]

In our lab, we exploited the same approach to create lateral doping gradients in p($g_4$2T-T) films doped with F_4TCNQ. This polymer has a larger dielectric constant than P3HT ($\varepsilon_r = 4.4$ instead of 2.7),[31, 91] which can be expected to reduce the Coulomb interactions between F_4TCNQ (di)anions and the charged polymer backbone,[31] facilitating the drift of anions in an electric field.

A bias voltage V_{bias} = 5 V across a 50 µm long channel (electric field of 0.1 V µm^{-1}) was sufficient to laterally dedope p($g_4$2T-T) films close to the negatively charged electrode as a result of F_4TCNQ counterions drifting toward the positive electrode (Figure 7.4a).

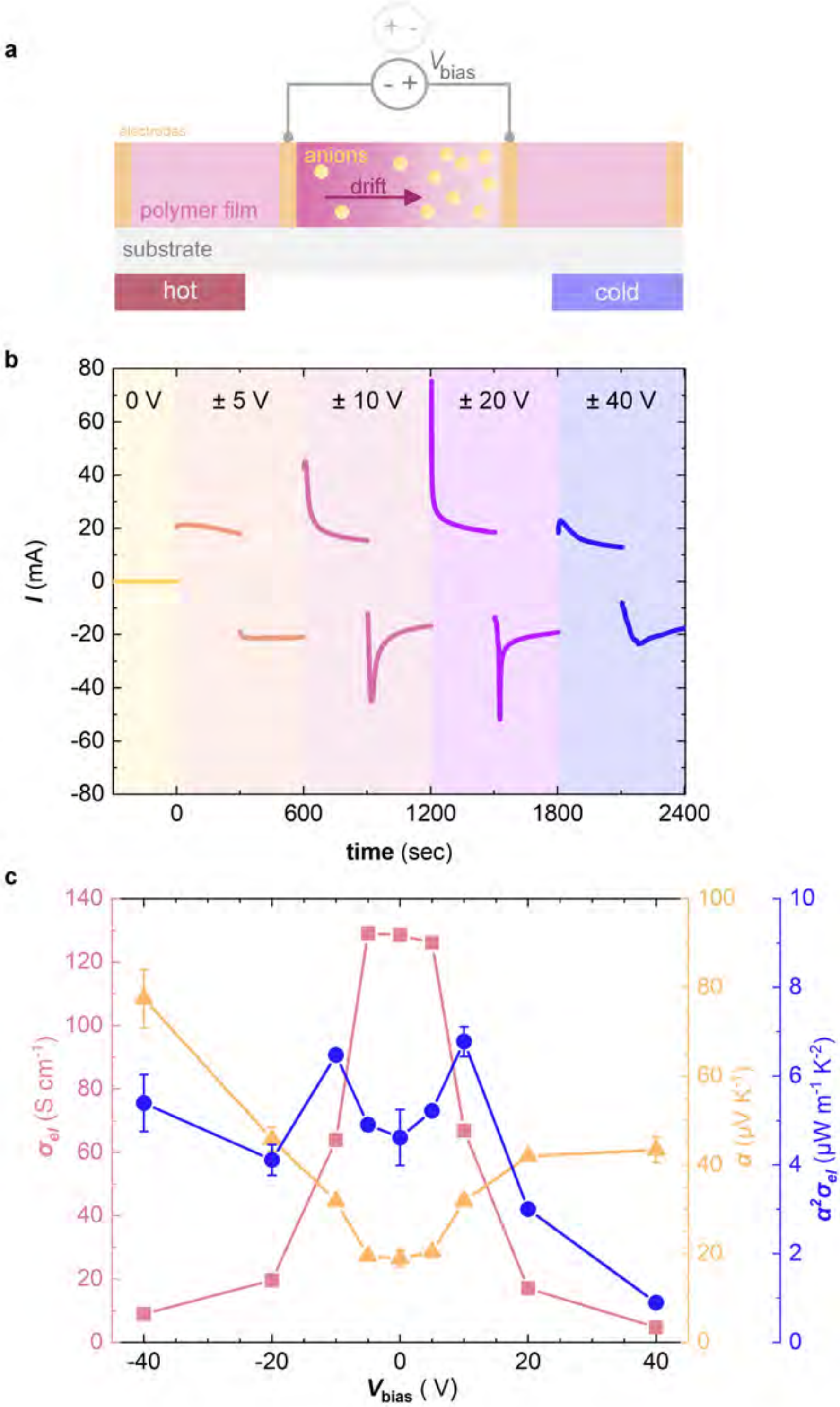

Figure 7.4. Thermoelectric properties of sequentially doped p(g$_4$2T-T) films with electrically programmed doping gradients: a) schematic of the setup, b) current between the inner electrodes vs. time upon application of different bias voltages V_{bias} with alternating sign between the inner electrodes; and c) effective electrical conductivity σ_{el} (pink squares), effective Seebeck coefficient α (yellow triangles), and power factor $\alpha^2\sigma_{el}$ (blue circles) obtained after each applied V_{bias}. Adapted with permission from ref [128] published by Wiley.

By gradually changing the magnitude and polarity of V_{bias} a decrease in σ_{el} and increase in α were observed for both cases, i.e. when the doping gradient is (1) parallel with the direction of ΔT ($V_{bias} < 0$) and (2) antiparallel ($V_{bias} > 0$). Interestingly, suitable doping gradients created at a specific V_{bias} (e.g. ± 10 V in Figure 7.4) resulted in an overall enhancement in power factor compared to homogeneously doped films.

The electrically programmed in-plane gradients remained stable for at least several minutes. However, over longer periods gradual changes occurred as evidenced by a return of the electrical resistance to close to its original value. This can be attributed to the gradual equilibration of the oxidation level along the channel.

These results indicate that lateral doping gradients can be created in doped conjugated polymer films, offering a new avenue for enhancing the thermoelectric performance of organic materials not yet optimized and for screening new materials for thermoelectric applications. However, for these gradients to become relevant for the construction of thermoelectric devices, it will be necessary to achieve stable profiles that do not change with time and temperature.

8 Thermoelectric generator for e-textiles

The text in this Section is adapted with permission from ref [73] published by Wiley.

Electronic textiles (e-textiles) are a versatile platform that uses textile manufacturing to integrate new functionalities into fabrics, such as health monitoring via sensors,[129, 130] communication via antennae[131] and thermal regulation via heating and cooling elements.[132] To power the integrated electronics, e-textiles should also incorporate energy harvesting devices capable of converting on-site energy into electricity.

Thermoelectric devices are attractive for this task, as they can generate electricity from body heat without relying on, e.g., external light, as required by solar cells,[133] or motion, as needed by piezo- [134, 135] and triboelectric[136] generators. Any difference in temperature, i.e. between skin and a colder (or warmer) environment, can be directly converted into an electrical potential through the Seebeck effect (Section 2.1).

A typical thermoelectric generator consists of multiple thermocouples, each composed of two legs that are connected thermally in parallel and electrically in series. These legs should be made of semiconductor materials that feature excellent thermoelectric properties, resulting in a high dimensionless figure of merit ZT (Equation 2.1, Section 2.1). Specifically, one type of leg is composed of a p-type material characterized by a positive Seebeck coefficient α_p, and the other leg is composed of an n-type material characterized by a negative Seebeck coefficient α_n. Each pair contributes to the total open-circuit voltage V_{oc} of a thermoelectric generator according to:

$$V_{oc} = N(\alpha_p - \alpha_n)\Delta T_{tc} \tag{8.1}$$

where N is the number of thermocouples and ΔT_{tc} is the temperature difference experienced by the device.[11]

Thermoelectric devices can be classified as in-plane or out-of-plane, based on the orientation of the temperature gradient, i.e. planar and vertical, respectively. For wearable applications, out-of-plane TEGs are more suitable since the temperature gradient between the human skin and the surroundings is along the orientation of the legs of the device, i.e. perpendicular to its outer surface.[11, 137]

Extensive research has been dedicated to p-type conjugated polymers. One promising material is PEDOT:PSS with σ_{el} > 1000 S cm^{-1} and a promising $ZT > 0.3$.[138, 139] PEDOT:PSS can be wet-spun into monofilaments[14, 74] and used as a coating material for, e.g., silk or cellulose yarns.[140, 141] However, the lack of air-stable n-type conjugated polymers has limited the advancement and the utility of this type of thermoelectric devices.

To address hypothesis 6, I herein summarize the most important findings of paper IV.[73] Specifically, I describe the fabrication of n-type conducting yarns based on the air-stable n-type polymer PBFDO (Section 8.1). Given their excellent performance in terms of mechanical and electrical properties, the n-type yarns were used to sew a button and construct a textile thermoelectric device through embroidery (Section 8.2).

8.1 n-type conducting yarns

There are various methods to produce electrically conducting fibers and yarns, which can be classified into two major types: (1) fiber spinning and drawing with an intrinsically conducting material, and (2) the functionalization of an already existing fiber through coating or dyeing.[142] Sarabia-Riquelme *et al.* recently reported the fabrication of highly conductive n-type monofilaments via wet-spinning of PBFDO, which feature a σ_{el} ≈ 1000-1600 S cm^{-1}, and a high E = 19.5 GPa while maintaining an ε_{break} of about 8%.[75]

Despite displaying outstanding thermoelectric properties as well as a high Young's modulus, single monofilaments have some limitations due to their small cross-sectional area, which results in a breaking force that is too low for many textile manufacturing methods.

To address this, PBFDO:DMSO ink, synthesized by Qifan Li,[117] was used to coat a multifilament yarn, which can be used as building blocks for the design of thermoelectric textiles through embroidery or machine sewing, as already reported for PEDOT:PSS multifilament yarns.[13, 143]

A batch coating process was used to prepare conducting n-type yarn, which involved two cycles of immersion of silk yarn in the PBFDO:DMSO ink followed by drying at 40 °C (see Methods section in paper IV for details). This method enabled the fabrication of continuous conductive yarn with a length of up to 1.5 m that comprised approximately 10 wt% of PBFDO (determined by weighing yarn before and after coating) (Figure 8.1a).

Scanning electron microscopy (SEM) was used to evaluate the quality of the PBFDO coating (Figure 8.1). SEM images of the yarn surface and cross section of freeze-fractured yarn sections show no distinct outer shell layer (Figure 8.1c-e). Intriguingly, charging artifacts are observed within the inner part of each filament, suggesting an insulating silk core surrounded by a conductive outer layer.

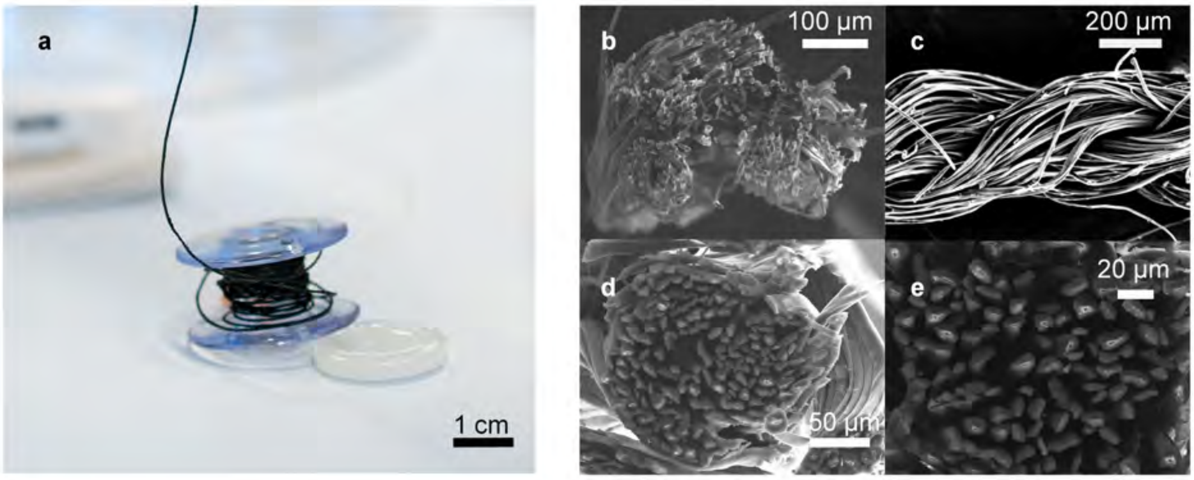

Figure 8.1. a) Photograph of a PBFDO coated silk yarn (photographer Hanna Magnusson). SEM micrographs of b) the cross section of neat silk yarn, c) a side view of silk yarn coated with PBFDO sputtered with gold, and d, e) the cross section of silk yarn coated with PBFDO (without gold sputtering). Adapted with permission from ref [73] published by Wiley.

Given the important role of mechanical properties in assessing the suitability of materials for the intended applications, tensile tests and fatigue cycles were performed on the conducting yarn using a DMA instrument.

The recorded stress-strain curves (Figure 8.2a) indicate that immersing silk yarn in PBFDO:DMSO ink reduces the Young's modulus from E = 1.7 ± 0.5 GPa for neat silk to 0.6 ± 0.1 GPa after coating, along with an increase in the strain at break reaching a value of up to ε_{break} = 14 ± 0.3 %. Similar mechanical changes are seen when immersing uncoated silk yarn in DMSO, indicating that the solvent and not the PBFDO causes the observed changes (Figure S8 in paper IV). To evaluate the impact of plastic deformation beyond the yield point, the electrical resistance of the n-type yarn was monitored during tensile deformation. The normalized resistance R/R_0, where R_0 is the resistance prior to tensile deformation, remains largely unaffected until the yarn fractures (Figure 8.2b). Moreover, PBFDO coated yarn can withstand cyclic stretching to 3 % for at least 200 cycles without fracture, while the in-situ resistance increased by less than 20 % (Figure 8.2c).[73]

The long-term stability of PBFDO coated yarn was monitored, and the electrical conductivity remained almost constant over a span of 24 months when storing the yarn at ambient conditions (Figure 7.3), as described in Section 7.1. Additionally, the conducting yarn was exposed to machine washing (see Methods section in paper IV for details). Interestingly, the PBFDO coated yarn also featured a promising degree of washability, with an increase in electrical resistance by a factor of only 3 after seven washing cycles at 20 °C (Figure 8.2d).

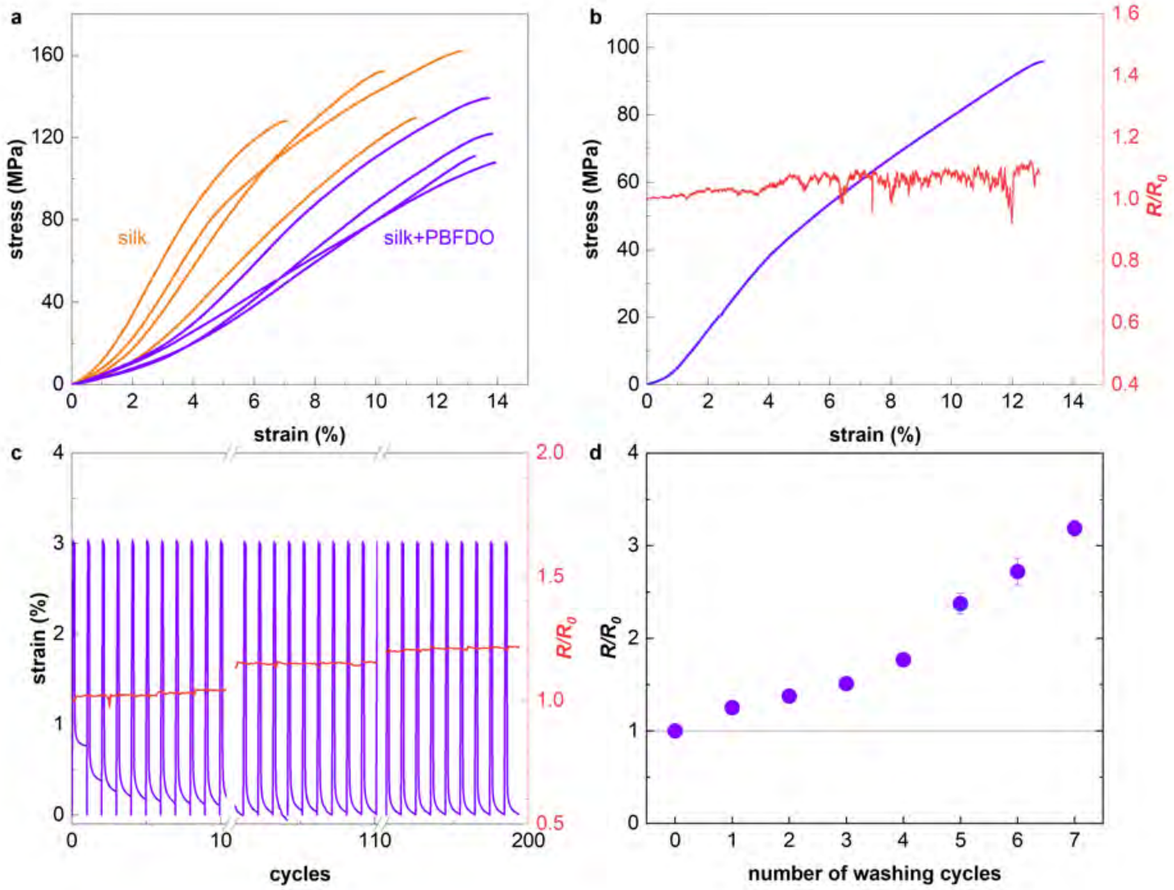

Figure 8.2. a) Stress-strain curves recorded during tensile deformation of neat (orange) and PBFDO coated (purple) silk yarn. b) Stress-strain curve of the PBFDO coated silk yarn (purple) and in-situ recorded change in electrical resistance R/R_0 (red) where R_0 is the resistance of the yarn prior to the tensile deformation. c) Strain during cyclic tensile deformation of the PBFDO coated silk yarn repeatedly stretched to 3 % then released for 60 s (purple) together with the in-situ recorded change in electrical resistance (red). d) Change in electrical resistance R/R_0 as a function of washing cycle of PBFDO coated silk yarn at 20 °C in a washing machine; measurement performed by the group of Prof. Byungil Hwang. Adapted with permission from ref [73] published by Wiley.

8.2 Textile thermoelectric generator

Ease of handling and mechanical robustness are essential for the fabrication of prototypes and devices. To demonstrate and highlight these qualities of PBFDO coated yarns, an out-of-plane textile thermocouple was fabricated by hand-stitching a commercial button with the conducting yarns onto three layers of felted wool fabric (Figure 8.3). The n- and p-type legs were constructed with PBFDO and PEDOT:PSS coated silk yarn, respectively, with the latter produced with a previously reported roll-to-roll coating method that yielded machine-washable p-type conducting yarn.[144] The thermoelectric properties of the n- and p-type yarns closely match, except for the opposite sign of the Seebeck coefficient (Table 8.1). The performance of the thermoelectric button was characterized (see Methods section in paper IV for details), and notably it did not considerably change after at least 41 weeks of storage at ambient conditions, indicating an excellent air-stability of the prototype.[73]

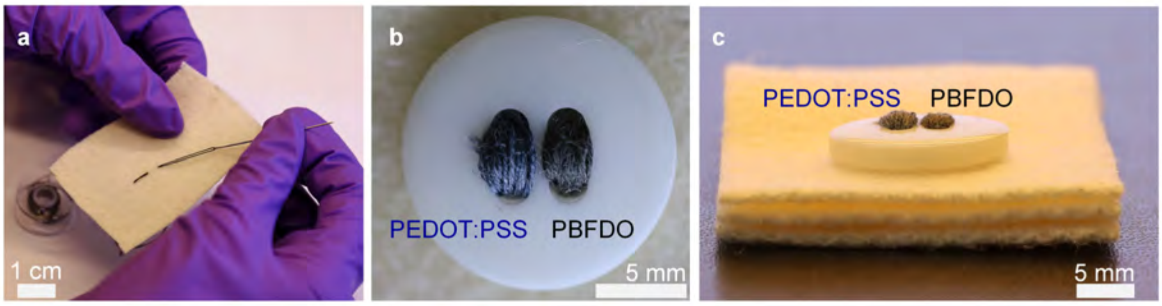

Figure 8.3. Photographs of a) hand-stitching process using PBFDO coated silk yarn, b) the top and c) side view of the thermoelectric button. Photographer: Dr. Youngseok Kim. Adapted with permission from ref [73] published by Wiley.

Table 8.1. Mechanical and thermoelectric properties of coated silk yarns. Young's modulus E, strain at break ε_{break}, effective electrical conductivity $\sigma_{el,eff}$ based on the total cross-sectional area of the yarn including the silk, conducting ink and voids, Seebeck coefficient α, and power factor $\alpha^2\sigma_{el,eff}$; values represent the mean and standard deviation of measurements of 5 samples; [a]values from ref [144].

yarn	E (GPa)	ε_{break} (%)	$\sigma_{el,eff}$ (S cm^{-1})	α (µV K^{-1})	$\alpha^2\sigma_{el,eff}$ (µW m^{-1} K^{-2})
PBFDO coated silk	0.6 ± 0.1	14 ± 0.3	13 ± 1	-18.8 ± 0.8	0.46 ± 0.04
PEDOT:PSS coated silk	2.9 ± 0.6[a]	10 ± 0.3[a]	13 ± 2	17.9 ± 0.1	0.42 ± 0.06

Given the robustness of the conducting yarns, a larger out-of-plane textile thermoelectric generator was also fabricated. PBFDO and PEDOT:PSS coated silk yarns were hand-sewn through 6 layers of felt wool forming 8 n-legs and 8 p-legs, respectively (Figure 8.4a). The n- and p-type legs were constructed with the same number of yarn sections and cross-sectional area because of the similar $\sigma_{el,eff}$ of the two types of coated silk yarn (see Table 8.1), meaning that the performance of the TEG is optimized if the legs have comparable dimensions.[13, 145]

The thermoelectric performance of the generator was characterized by placing the device between a hot plate and a heat sink with a temperature T_{hot} and T_{cold}, respectively. The temperature of the hot plate was increased to generate stepwise increasing temperature gradients $\Delta T = T_{hot} - T_{cold}$, thus exposing the thermoelectric legs to a temperature gradient ΔT_{tc} (note that $\Delta T_{tc} < \Delta T$ because of thermal contact resistance between the device and the heat source and sink). At each ΔT, the generated voltage V was recorded while a variable load was applied by drawing different currents I with a source-measure unit (see Methods section in paper IV for details).

The measured open circuit voltage V_{oc}, i.e. the extrapolated voltage at I = 0, increased linearly with ΔT (Figure 8.4b) and a value of $V_{oc}/\Delta T$ = 243 μV K^{-1} was estimated assuming that $\Delta T_{tc} = \Delta T$. Instead, Equation 8.1 predicts a higher value of $V_{oc}/\Delta T_{tc}$ = 294 μV K^{-1}, which was explained with thermal contact resistance and hence $\Delta T_{tc} \approx 0.83 \cdot \Delta T$ (cf. solid and dashed lines in Figure 8.4b). The output power was calculated according to:

$$P_{out} = VI \tag{8.2}$$

and reached a maximum for the current at which the internal resistance of the device R_{in} = 119 Ω and the load R_{load} are equal. The measured P_{max} achieved by the device increased with ΔT, reaching a highest value of P_{max} = 0.67 μW at ΔT = 70 K (Figure 8.4c).[73]

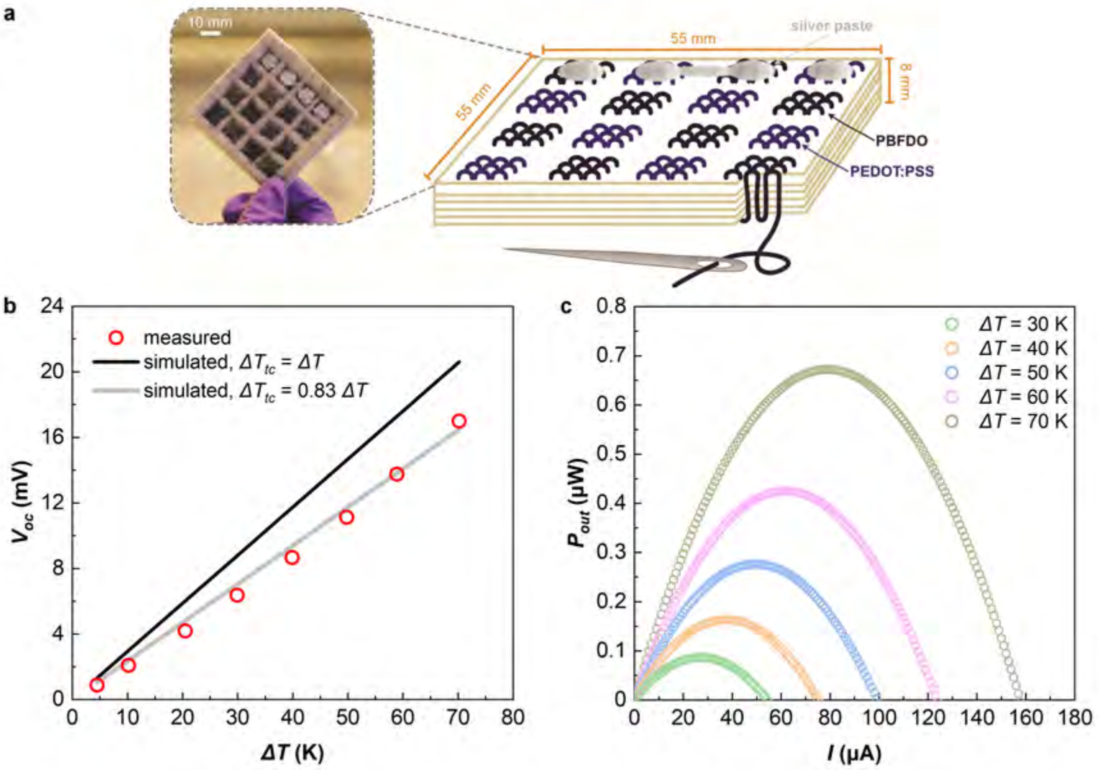

Figure 8.4. Performance of the thermoelectric generator composed of 8 thermocouples. a) Schematic and photograph of the thermoelectric generator. The photograph was taken by Dr. Youngseok Kim, while Chunghyeon Choi and Hyungsub Yoon hand-sewed the thermoelectric generator. b) Open-circuit voltage V_{oc} as a function of $\Delta\mathrm{T}$ (circles represent experimental values; black and grey lines calculated assuming that $\Delta T_{tc} = \Delta T$ and $\Delta T_{tc} = 0.83 \cdot \Delta T$, respectively). c) Output power P_{out} of the thermopile as a function of current I for different temperature differences ΔT. Adapted with permission from ref [73] published by Wiley.

9 Conclusions and outlooks

In this thesis, I investigate various structure-property relationships that influence the thermoelectric and mechanical properties of p- and n-type conjugated polymers. Specifically, I highlight the importance of solid-state order for enhancing charge transport, air stability for ensuring long-term performance, and mechanical robustness for enabling the fabrication of thermoelectric generators.

To begin with, I studied how side-chain engineering can influence the thermoelectric properties of thiophene-based conjugated polymers. Varying the length of oligoether side chains influenced the resulting degree of order of polymer films. Notably, p($g_3$2T-T), having the shortest side chains, exhibited a higher degree of structural order in both its pristine and oxidized state compared to p($g_4$2T-T) and p($g_6$2T-T). This directly translated to superior thermoelectric properties (Figure 9.1a), primarily attributed to the enhanced charge-carrier mobility, and thus electrical conductivity, favored by more pronounced π-stacking. Films of p($g_3$2T-T) co-processed with 20 mol% of F_4TCNQ reached an electrical conductivity of up to σ_{el} = 830 ± 15 S cm^{-1}. This value initially dropped to about 200 S cm^{-1}, and subsequently it remained stable for at least 3 months of aging at ambient conditions. I attributed the promising level of stability of aged samples to the presence of F_4TCNQ dianions, which likely exhibit reduced diffusion within the polymer film due to their higher valency compared to F_4TCNQ anions, leading to an improved long-term performance. Exchanging oligoether side chains for alkyl side chains in a random oligoether:alkyl copolymer, pTTEG-*co*-pTTA, influenced its thermoelectric performance (Figure 9.1a). Despite exhibiting a lower degree of order, the copolymer with mixed side chains displayed a higher power factor $\alpha^2\sigma_{el}$ compared to the fully oligoether-side-chain counterpart, pTTEG. This finding suggests that other factors than structural order contribute to thermoelectric performance, which still need to be elucidated for pTTEG-*co*-pTTA.

Next, the drift of dopant counterions in an electric field was exploited to create lateral doping gradients. It was demonstrated that applying an electric field of 0.1 V µm^{-1} is sufficient to induce drift of F_4TCNQ counterions within p($g_4$2T-T) films. The obtained doping gradients displayed an overall increase in $\alpha^2\sigma_{el}$ compared to initially homogeneous films, when an intermediate V_{bias} is applied (Figure 9.1a). Regardless of the limited stability, i.e. several minutes, the creation of lateral doping gradients is a promising strategy to improve the thermoelectric performance of not yet optimally doped conjugated polymers, which may facilitate the screening of new materials as well as new dopant:polymer systems.

Given the change in microstructure of polymer films upon doping, I argued that their mechanical properties would also be affected. Hence, I studied the impact of chemical doping on the mechanical properties of conjugated polymers with oligoether side chains, i.e. p($g_3$2T-T) and p(g_3TT-T2). The results showed that doping leads to an increase in the temperature associated with relaxation processes of the polymer chain. For instance, in the case of p($g_3$2T-T), $T_{\alpha/\beta}$ shifted from −30 °C to 5 °C upon doping, while in p(g_3TT-T2), T_β increased from −50 °C to −3 °C when doped with F_4TCNQ. I attributed this increase to several factors, such as an improved π-stacking induced by doping, a change in the rigidity of the backbone upon oxidation as well as a change in free volume due to the presence of dopant counterions, which likely interact with the polymer chain. Moreover, the type of dopant counterions influenced the extent to which the relaxation temperature increased, which can be explained by differences in oxidation level, location of the anion relative to the polymer backbone, and variations in free volume available for side-chain motion.

These changes in relaxation temperatures upon doping also resulted in a change in the stiffness of the polymers at room temperature. Specifically, the Young's moduli of doped polymers were found to be higher than the neat counterpart, with the most pronounced enhancement observed in case of p(g_3TT-T2), where sequential doping with F_4TCNQ resulted in a 20-fold increase, reaching E = 0.7 ± 0.2 GPa. Interestingly, the choice of counterion had a significant impact on the Young's modulus of doped polymers. For example, p(g_3TT-T2) doped samples exhibited a similar $\sigma_{el} \approx 100$ S cm^{-1} but a significantly different Young's modulus with values varying from E = 0.05 to 0.7 GPa at room temperature. This observation suggests that selecting a specific doping mechanism and dopant counterion allows to partially decouple the often-observed correlation between σ_{el} and E.

Lastly, I studied the thermomechanical properties of PBFDO, which was assumed to be stiff and brittle due to the absence of soft and flexible side chains. However, the polymer could be processed into bendable free-standing samples, which exhibited a high stiffness and a certain degree of ductility. This behavior is likely attributed to limited local relaxation processes at low temperatures that facilitate a certain degree of deformation even below T_α. The polymer

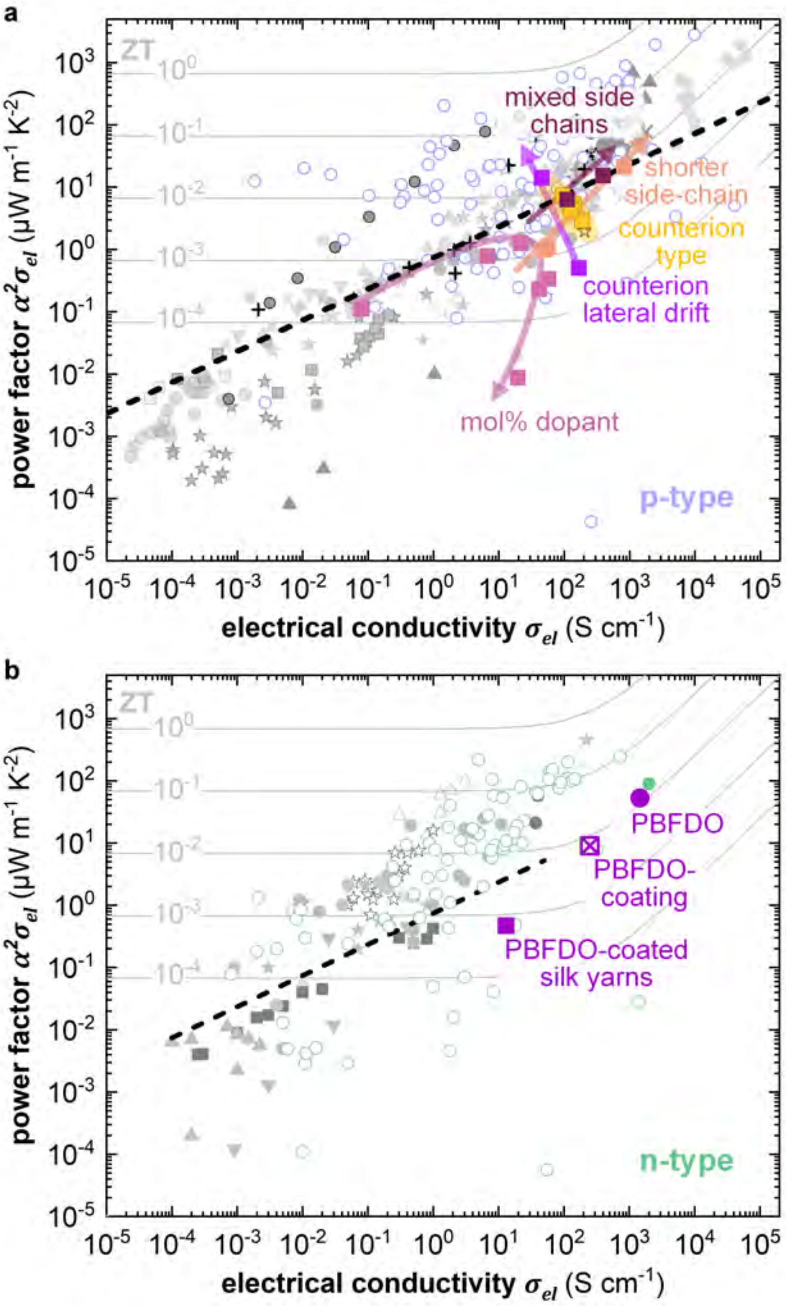

Figure 9.1. Thermoelectric power factor $\alpha^2\sigma_{el}$ vs. electrical conductivity σ_{el} of a) p-type and b) n-type conducting polymers. Highlighted symbols are experimental data from this thesis. Grey symbols are data extracted from ref [38] (and references therein), open blue and green symbols are data from literature extracted from an open-access database built within the Marie Curie ITN project HORATES.[146] The dashed black lines represent the empirical power laws proposed by Chabinyc *et al.*[46] and by Kemerink *et al.*.[147] The grey isolines indicating constant *ZT* for *T* = 300 K were drawn using Equation 2.1, assuming κ_{phonon} = 0.2 W m^{-1}K^{-1} and that the Wiedemann-Franz law is obeyed. Adapted with permission from ref [38] published by Elsevier.

demonstrates a Young's modulus $E = 6.6 \pm 0.9$ GPa and a strain at break $\varepsilon_{break} = 5.2 \pm 1.1\%$ at room temperature. Its excellent processability and mechanical robustness enabled the fabrication of n-type multifilaments by coating silk yarn. The obtained conductive yarn exhibited a remarkable air-stability for conducting polymers, maintaining an effective bulk conductivity of 13 S cm^{-1} for nearly 2 years (Figure 9.1b; overall conductivity of silk and conducting coating), with a projected half-life of 3.7 ± 0.8 years at ambient conditions. Given the outstanding mechanical and electrical performance, PBFDO coated yarn was used to fabricate an out-of-plane thermoelectric generator by embroidery, characterized by an open-circuit voltage of 17 mV and a maximum output power of 0.67 µW for a temperature difference of 70 K.

These results emphasize the importance of investigating the mechanical properties, alongside the thermoelectric performance, of conjugated polymers in their neat and oxidized or reduced state. They also highlight the crucial role of mechanical robustness and ease of handling in the context of device fabrication for wearable thermoelectric applications.

The limited stability of doped conjugated polymers is one of the challenges that hinder the transition of organic thermoelectric materials from lab to real-world applications. Fundamental studies on the degradation processes of the doped state, such as dopant diffusion and sublimation, are needed, which may allow to identify approaches that improve the stability. Hence, in future research, I would aim to explore the stability of new polymer:dopant systems, with a particular focus on how the size and valency of dopant counterions influence the long-term performance. For example, the use of tetravalent counterions was reported to enhance the system stability due to the strong Coulomb interaction between the counterion and the doped polymer, increasing the diffusion resistance.[121] Expanding the investigation of proton-coupled electron-transfer doping in the presence of electrolytes containing multivalent anions would allow to evaluate their impact on doping stability. This strategy may also be extended to the development of lateral doping gradients with enhanced stability, improving their potential in enhancing the thermoelectric properties of not yet optimized materials. Altogether, this comprehensive approach could yield valuable insights into both improving thermoelectric performance and ensuring ambient stability of organic thermolectrics.

This thesis demonstrates that the mechanical properties of conjugated polymers correlate with the relaxation processes of the polymer chains, which are influenced by chemical doping. However, further research is required. Additional experiments are needed to elucidate the polymer chain relaxation mechanisms of conjugated polymers, as well as the role of doping process and dopant counterions. Complementary experimental techniques, such as fast scanning calorimetry and optical spectroscopy including FTIR and Raman spectroscopy at different temperatures, may be considered to provide valuable insights. Moreover, expanding the investigation to other conjugated polymers will help to determine if the doping-induced effects observed in this thesis are relevant also for other systems. It can be anticipated that this study will provide an in-depth understanding of the complex mechanical (and rheological) behavior of conjugated polymers in their neat and doped state. Ultimately, this knowledge will aid the design of robust and/or elastic materials, with significant outcomes for the advancement of wearable electronics and bioelectronics.

ACKNOWLEDGMENTS

I want to express my gratitude to my supervisor Prof. Christian Müller. It has been a pleasure working with you, I am very thankful for believing in me and giving me the opportunity to be part of your research group at Chalmers. Your continuous support and guidance helped me grow a lot, both from a professional and personal point of view. I could not have asked for a better supervisor, thank you!

Thanks to my examiner Anna Martinelli for guiding me through this journey, especially from the educational point of view.

Big thanks to everyone at Chalmers I had the privilege to collaborate closely with:
Joost for being an incredible teammate and friend, always ready to help and share your passion for science, I learnt so much from you; Youngseok for all your help in the lab and for sharing your knowledge (and lab tricks!); Sepideh for being a great supervisor during my master's and a caring and supportive friend (can't wait for the next German city!); Meghna for all your support, both scientific and personal, and for bringing such positive energy during the last months of my PhD; Emmy for being always so kind and for sharing with me your doping skills; Mariza and Sozan for the fun times working together on the cellulose project in the lab; S. Haraguchi for being very helpful and kind all the times.
Thanks to Jesika, Qifan and Jiali to be fantastic workmates and friends. I feel very lucky to have worked closely with you!

Thanks to everyone who I had the pleasure to collaborate with:
R. Kroon and S. Fabiano from Linköping university and I. Mcculloch, S. Griggs, J. Tian from University of Oxford for making the polymers I could use for my thesis; J. Martin, S. Marina and A. Peinador Veiga from University of La Coruna for all GIWAXS measurements; D. Kim, I. Zozoulenko and T. Liu from Linköping university; J. Liu from Changchun Institute of Applied Chemistry; V.K. Gupta, A. Martinelli and A. Schaefer from Chalmers; K. Xu, J.S. Reparaz and M. Campoy-Quiles from ICMAB; D. Scheunemann and M. Kemerink from Heidelberg University; J.A. Koster form University of Groningen; C. Choi, H. Yoon and B. Hwang from Chung-Ang University. Z. Zeng and B. Mihiretie from HotDisk AB.
I would also like to thank Prof. Martin Brinkmann, Prof. Mariano Campoy-Quiles and Dr. Antonio Iacchetti and their teams for warmly welcoming and hosting me during my secondments at ICS-CNRS in Strasbourg, ICMAB in Barcelona and RibesTech in Milan.

Thanks to Ruby, Judith and Vero for being such wonderful friends, for all the laughs, the support and the sweet presents that you left on my desk. Looking forward to the next Ikea trip!

Big thanks to all friends and colleagues on floor 8th for creating such a friendly and positive working environment. It has been amazing to share so many great moments with you: starting from everyday lunches to the amazing trips organized by Krzys, barbecues at Joost's, girl shopping sessions and dinners, board games nights, hotpot dinners, escape rooms, crafting activities, AWs at Tullen, cocktail evenings at Strangers, and brunches at Brunchoteket.
Special thanks to Lotta for taking care of us.

To all members (past and present) of Christian's group: you are an incredible group! It has been amazing to work with you.

Thanks to the whole HORATES group, you made all our workshops so much fun!

Thank you Mona for being a great friend, you are my family in Göteborg since 2019!

Grazie a Margherita, Peter, Martin e Tea per avermi sempre accolta a braccia aperte, come una famiglia. Con voi mi sono sentita spesso più vicina a casa.

Vivere lontano da amici e familiari non è mai semplice. Vorrei ringraziare i miei amici per esserci stati, nonostante la distanza, con messaggi, lunghe chiamate e le immancabili cene di reunion ogni volta che tornavo in Italia. Un grazie speciale a Giuli, Meri e Chià: anche se non ci vediamo spesso, ogni volta è come se il tempo non fosse mai passato. Grazie anche agli alumni BT-ER, sempre pronti ad organizzare un aperitivo di aggiornamento.

Grazie alla mia amata famiglia: nonni, zii e cuginetti! Tornare a casa da voi è sempre stata una gioia immensa. Anche da lontano, vi ho sentiti sempre vicini. Il vostro affetto mi ha accompagnata in ogni momento.

Un grazie speciale va ai miei genitori, Fosca e Renzo. Ogni traguardo che raggiungo è anche un traguardo vostro: non sarei qui oggi senza il vostro amore e il vostro supporto. Sono orgogliosa e fortunata di avervi come genitori, non avrei potuto desiderare un amore più grande del vostro.

Ad Ale, grazie per il tuo infinito supporto e amore. Per esserci sempre stato in questa avventura, ogni giorno, con una chiamata e un pensiero. Anche da lontano, ti ho sentito vicino in ogni momento.

BIBLIOGRAPHY

[1] H. Shirakawa, E. J. Louis, A. G. MacDiarmid, C. K. Chiang, A. J. Heeger, *Journal of the Chemical Society, Chemical Communications* **1977**, 578.

[2] N. Sun, C. Jiang, Q. Li, D. Tan, S. Bi, J. Song, *Journal of Materials Science: Materials in Electronics* **2020**, *31*, 20688.

[3] J. Bauri, R. B. Choudhary, G. Mandal, *Journal of Materials Science* **2021**, *56*, 18837.

[4] H. Zhou, Y. Zhang, J. Seifter, S. D. Collins, C. Luo, G. C. Bazan, T.-Q. Nguyen, A. J. Heeger, *Advanced Materials* **2013**, *25*, 1646.

[5] E. K. Solak, E. Irmak, *RSC Advances* **2023**, *13*, 12244.

[6] S. Inal, J. Rivnay, A.-O. Suiu, G. G. Malliaras, I. McCulloch, *Accounts of Chemical Research* **2018**, *51*, 1368.

[7] T. Someya, Z. Bao, G. G. Malliaras, *Nature* **2016**, *540*, 379.

[8] J. F. Mike, J. L. Lutkenhaus, *Journal of Polymer Science Part B: Polymer Physics* **2013**, *51*, 468.

[9] Z. Genene, Z. Xia, G. Yang, W. Mammo, E. Wang, *Advanced Materials Technologies* **2024**, *9*, 2300167.

[10] Z. Zhang, M. Liao, H. Lou, Y. Hu, X. Sun, H. Peng, *Advanced Materials* **2018**, *30*, 1704261.

[11] R. Kroon, D. A. Mengistie, D. Kiefer, J. Hynynen, J. D. Ryan, L. Yu, C. Müller, *Chemical Society Reviews* **2016**, *45*, 6147.

[12] N. Pataki, P. Rossi, M. Caironi, *Applied Physics Letters* **2022**, *121*.

[13] A. Lund, Y. Tian, S. Darabi, C. Müller, *Journal of Power Sources* **2020**, *480*, 228836.

[14] Y. Kim, A. Lund, H. Noh, A. I. Hofmann, M. Craighero, S. Darabi, S. Zokaei, J. I. Park, M.-H. Yoon, C. Müller, *Macromolecular Materials and Engineering* **2020**, *305*, 1900749.

[15] G. Heimel, *ACS Central Science* **2016**, *2*, 309.

[16] I. Zozoulenko, A. Singh, S. K. Singh, V. Gueskine, X. Crispin, M. Berggren, *ACS Applied Polymer Materials* **2019**, *1*, 83.

[17] M. Jha, J. Mogollon Santiana, A. A. Jacob, K. Light, M. L. Hong, M. R. Lau, L. R. Filardi, H. Miao, S. M. Gurses, C. X. Kronawitter, M. Mascal, A. J. Moulé, *The Journal of Physical Chemistry C* **2024**, *128*, 1258.

[18] A. D. Scaccabarozzi, A. Basu, F. Aniés, J. Liu, O. Zapata-Arteaga, R. Warren, Y. Firdaus, M. I. Nugraha, Y. Lin, M. Campoy-Quiles, N. Koch, C. Müller, L. Tsetseris, M. Heeney, T. D. Anthopoulos, *Chemical Reviews* **2022**, *122*, 4420.

[19] R. J. Mammone, A. G. MacDiarmid, *Journal of the Chemical Society, Faraday Transactions 1: Physical Chemistry in Condensed Phases* **1985**, *81*, 105.

[20] S. Hultmark, M. Craighero, S. Zokaei, D. Kim, E. Järsvall, F. Farooqi, S. Marina, R. Kroon, J. Martin, I. Zozoulenko, C. Müller, *Journal of Materials Chemistry C* **2023**, *11*, 8091.

[21] W. Jin, C.-Y. Yang, R. Pau, Q. Wang, E. K. Tekelenburg, H.-Y. Wu, Z. Wu, S. Y. Jeong, F. Pitzalis, T. Liu, Q. He, Q. Li, J.-D. Huang, R. Kroon, M. Heeney, H. Y. Woo, A. Mura, A. Motta, A. Facchetti, M. Fahlman, M. A. Loi, S. Fabiano, *Nature* **2024**, *630*, 96.

[22] A. I. Hofmann, R. Kroon, L. Yu, C. Müller, *Journal of Materials Chemistry C* **2018**, *6*, 6905.

[23] Y. Cao, P. Smith, A. J. Heeger, *Synthetic Metals* **1992**, *48*, 91.

[24] B. Yurash, D. X. Cao, V. V. Brus, D. Leifert, M. Wang, A. Dixon, M. Seifrid, A. E. Mansour, D. Lungwitz, T. Liu, P. J. Santiago, K. R. Graham, N. Koch, G. C. Bazan, T.-Q. Nguyen, *Nature Materials* **2019**, *18*, 1327.

[25] E. Hyun Suh, S. Beom Kim, J. Jung, J. Jang, *Angewandte Chemie International Edition* **2023**, *62*, e202304245.

[26] O. Zapata-Arteaga, A. Perevedentsev, M. Prete, S. Busato, P. S. Floris, J. Asatryan, R. Rurali, J. Martín, M. Campoy-Quiles, *ACS Energy Letters* **2024**, *9*, 3567.

[27] I. E. Jacobs, Y. Lin, Y. Huang, X. Ren, D. Simatos, C. Chen, D. Tjhe, M. Statz, L. Lai, P. A. Finn, W. G. Neal, G. D'Avino, V. Lemaur, S. Fratini, D. Beljonne, J. Strzalka, C. B. Nielsen, S. Barlow, S. R. Marder, I. McCulloch, H. Sirringhaus, *Advanced Materials* **2022**, *34*, 2102988.

[28] Y. Yamashita, J. Tsurumi, M. Ohno, R. Fujimoto, S. Kumagai, T. Kurosawa, T. Okamoto, J. Takeya, S. Watanabe, *Nature* **2019**, *572*, 634.

[29] Y. Yamashita, S. Kohno, E. Longhi, S. Jhulki, S. Kumagai, S. Barlow, S. R. Marder, J. Takeya, S. Watanabe, *Communications Materials* **2024**, *5*, 79.

[30] M. Ishii, Y. Yamashita, S. Watanabe, K. Ariga, J. Takeya, *Nature* **2023**, *622*, 285.

[31] D. Scheunemann, E. Järsvall, J. Liu, D. Beretta, S. Fabiano, M. Caironi, M. Kemerink, C. Müller, *Chemical Physics Reviews* **2022**, *3*.

[32] S. Ihnatsenka, X. Crispin, I. V. Zozoulenko, *Physical Review B* **2015**, *92*, 035201.

[33] H. Sirringhaus, P. J. Brown, R. H. Friend, M. M. Nielsen, K. Bechgaard, B. M. W. Langeveld-Voss, A. J. H. Spiering, R. A. J. Janssen, E. W. Meijer, P. Herwig, D. M. de Leeuw, *Nature* **1999**, *401*, 685.

[34] J. Rivnay, R. Noriega, R. J. Kline, A. Salleo, M. F. Toney, *Physical Review B* **2011**, *84*, 045203.

[35] R. Noriega, J. Rivnay, K. Vandewal, F. P. V. Koch, N. Stingelin, P. Smith, M. F. Toney, A. Salleo, *Nature Materials* **2013**, *12*, 1038.

[36] S. E. Root, S. Savagatrup, A. D. Printz, D. Rodriquez, D. J. Lipomi, *Chemical Reviews* **2017**, *117*, 6467.

[37] R. Xie, R. H. Colby, E. D. Gomez, *Advanced Electronic Materials* **2018**, *4*, 1700356.

[38] D. Beretta, N. Neophytou, J. M. Hodges, M. G. Kanatzidis, D. Narducci, M. Martin- Gonzalez, M. Beekman, B. Balke, G. Cerretti, W. Tremel, A. Zevalkink, A. I. Hofmann, C. Müller, B. Dörling, M. Campoy-Quiles, M. Caironi, *Materials Science and Engineering: R: Reports* **2019**, *138*, 100501.

[39] J. Liu, B. van der Zee, R. Alessandri, S. Sami, J. Dong, M. I. Nugraha, A. J. Barker, S. Rousseva, L. Qiu, X. Qiu, N. Klasen, R. C. Chiechi, D. Baran, M. Caironi, T. D. Anthopoulos, G. Portale, R. W. A. Havenith, S. J. Marrink, J. C. Hummelen, L. J. A. Koster, *Nature Communications* **2020**, *11*, 5694.

[40] D. Scheunemann, M. Kemerink, *Physical Review B* **2020**, *101*, 075206.

[41] X. Rodríguez-Martínez, F. Saiz, B. Dörling, S. Marina, J. Guo, K. Xu, H. Chen, J. Martin, I. McCulloch, R. Rurali, J. S. Reparaz, M. Campoy-Quiles, *Advanced Energy Materials* **2024**, *14*, 2401705.

[42] D. Moses, A. Denenstein, *Physical Review B* **1984**, *30*, 2090.

[43] D. Rosas Villalva, S. Singh, L. A. Galuska, A. Sharma, J. Han, J. Liu, M. A. Haque, S. Jang, A. H. Emwas, L. J. A. Koster, X. Gu, B. C. Schroeder, D. Baran, *Materials Horizons* **2022**, *9*, 500.

[44] O. Zapata-Arteaga, A. Perevedentsev, S. Marina, J. Martin, J. S. Reparaz, M. Campoy-Quiles, *ACS Energy Letters* **2020**, *5*, 2972.

[45] H. Zhao, N. Prine, G. Ma, Y. Zhang, M. A. Haque, D. Baran, X. Gu, *Sustainable Energy & Fuels* **2023**, *7*, 369.

[46] A. M. Glaudell, J. E. Cochran, S. N. Patel, M. L. Chabinyc, *Advanced Energy Materials* **2015**, *5*, 1401072.

[47] J. Kimpel, Y. Kim, H. Schomaker, D. R. Hinojosa, J. Asatryan, J. Martín, R. Kroon, M. Sommer, C. Müller, *Science Advances* **2025**, *in press*.

[48] J. Kimpel, Y. Kim, J. Asatryan, J. Martín, R. Kroon, C. Müller, *Chemical Science* **2024**, *15*, 7679.

[49] D. Scheunemann, V. Vijayakumar, H. Zeng, P. Durand, N. Leclerc, M. Brinkmann, M. Kemerink, *Advanced Electronic Materials* **2020**, *6*, 2000218.

[50] S. Guchait, Y. Zhong, M. Brinkmann, *Macromolecules* **2023**, *56*, 6733.

[51] J. Hynynen, E. Järsvall, R. Kroon, Y. Zhang, S. Barlow, S. R. Marder, M. Kemerink, A. Lund, C. Müller, *ACS Macro Letters* **2019**, *8*, 70.

[52] O. Zapata-Arteaga, S. Marina, G. Zuo, K. Xu, B. Dörling, L. A. Pérez, J. S. Reparaz, J. Martín, M. Kemerink, M. Campoy-Quiles, *Advanced Energy Materials* **2022**, *12*, 2104076.

[53] A. Abtahi, S. Johnson, S. M. Park, X. Luo, Z. Liang, J. Mei, K. R. Graham, *Journal of Materials Chemistry A* **2019**, *7*, 19774.

[54] A. X. Chen, A. T. Kleinschmidt, K. Choudhary, D. J. Lipomi, *Chemistry of Materials* **2020**, *32*, 7582.

[55] S. H. K. Paleti, Y. Kim, J. Kimpel, M. Craighero, S. Haraguchi, C. Müller, *Chemical Society Reviews* **2024**, *53*, 1702.

[56] S. Zokaei, R. Kroon, J. Gladisch, B. D. Paulsen, W. Sohn, A. I. Hofmann, G. Persson, A. Stamm, P.-O. Syrén, E. Olsson, J. Rivnay, E. Stavrinidou, A. Lund, C. Müller, *Advanced Science* **2021**, *8*, 2002778.

[57] M. Ashizawa, Y. Zheng, H. Tran, Z. Bao, *Progress in Polymer Science* **2020**, *100*, 101181.

[58] S. Zokaei, M. Craighero, C. Cea, L. M. Kneissl, R. Kroon, D. Khodagholy, A. Lund, C. Müller, *Small* **2022**, *18*, 2102813.

[59] M. Z. Seyedin, J. M. Razal, P. C. Innis, G. G. Wallace, *Advanced Functional Materials* **2014**, *24*, 2957.

[60] D. Kiefer, L. Yu, E. Fransson, A. Gómez, D. Primetzhofer, A. Amassian, M. Campoy-Quiles, C. Müller, *Advanced Science* **2017**, *4*, 1600203.

[61] M. Mone, Y. Kim, S. Darabi, S. Zokaei, L. Karlsson, M. Craighero, S. Fabiano, R. Kroon, C. Müller, *ACS Applied Materials & Interfaces* **2023**, *15*, 28300.

[62] D. Zhao, Q. Zhang, W. Chen, X. Yi, S. Liu, Q. Wang, Y. Liu, J. Li, X. Li, H. Yu, *ACS Applied Materials & Interfaces* **2017**, *9*, 13213.

[63] S. Zokaei, D. Kim, E. Järsvall, A. M. Fenton, A. R. Weisen, S. Hultmark, P. H. Nguyen, A. M. Matheson, A. Lund, R. Kroon, M. L. Chabinyc, E. D. Gomez, I. Zozoulenko, C. Müller, *Materials Horizons* **2022**, *9*, 433.

[64] M. Craighero, J. Guo, S. Zokaei, S. Griggs, J. Tian, J. Asatryan, J. Kimpel, R. Kroon, K. Xu, J. S. Reparaz, J. Martín, I. McCulloch, M. Campoy-Quiles, C. Müller, *ACS Applied Electronic Materials* **2024**, *6*, 2909.

[65] I. M. Ward, J. Sweeney, *An Introduction to the Mechanical Properties of Solid Polymers, 2nd Edition*, Wiley, 2004.

[66] C. Müller, *Chemistry of Materials* **2015**, *27*, 2740.

[67] S. H. K. Paleti, S. Haraguchi, Z. Cao, M. Craighero, J. Kimpel, Z. Zeng, P. Sowinski, D. Zhu, J. Pons i Tarrés, Y. Kim, Q. Li, J. Huang, A. Kalaboukhov, B. Mihiretie, S. Fabiano, X. Gu, C. Müller, *Macromolecules* **2025**, *58*, 3578.

[68] R. Xie, A. R. Weisen, Y. Lee, M. A. Aplan, A. M. Fenton, A. E. Masucci, F. Kempe, M. Sommer, C. W. Pester, R. H. Colby, E. D. Gomez, *Nature Communications* **2020**, *11*, 893.

[69] K. Tang, A. Shaw, S. Upreti, H. Zhao, Y. Wang, G. T. Mason, J. Aguinaga, K. Guo, D. Patton, D. Baran, S. Rondeau-Gagné, X. Gu, *Chemistry of Materials* **2025**, *37*, 756.

[70] B. O'Connor, E. P. Chan, C. Chan, B. R. Conrad, L. J. Richter, R. J. Kline, M. Heeney, I. McCulloch, C. L. Soles, D. M. DeLongchamp, *ACS Nano* **2010**, *4*, 7538.

[71] J. Moulton, P. Smith, *Polymer* **1992**, *33*, 2340.

[72] B. O'Connor, R. J. Kline, B. R. Conrad, L. J. Richter, D. Gundlach, M. F. Toney, D. M. DeLongchamp, *Advanced Functional Materials* **2011**, *21*, 3697.

[73] M. Craighero, Q. Li, Z. Zeng, C. Choi, Y. Kim, H. Yoon, T. Liu, P. Sowinski, S. Haraguchi, B. Hwang, B. Mihiretie, S. Fabiano, C. Müller, *Advanced Science* **2024**, *11*, 2406770.

[74] R. Sarabia-Riquelme, R. Andrews, J. E. Anthony, M. C. Weisenberger, *Journal of Materials Chemistry C* **2020**, *8*, 11618.

[75] R. Sarabia-Riquelme, L. E. Noble, P. Alarcon Espejo, Z. Ke, K. R. Graham, J. Mei, A. F. Paterson, M. C. Weisenberger, *Advanced Functional Materials* **2024**, *34*, 2311379.

[76] N. Kim, S. Lienemann, I. Petsagkourakis, D. Alemu Mengistie, S. Kee, T. Ederth, V. Gueskine, P. Leclère, R. Lazzaroni, X. Crispin, K. Tybrandt, *Nature Communications* **2020**, *11*, 1424.

[77] Y. Wang, C. Zhu, R. Pfattner, H. Yan, L. Jin, S. Chen, F. Molina-Lopez, F. Lissel, J. Liu, N. I. Rabiah, Z. Chen, J. W. Chung, C. Linder, M. F. Toney, B. Murmann, Z. Bao, *Science Advances* **2017**, *3*, e1602076.

[78] M. Craighero, M. Jha, V. Flores Vela, J. Kimpel, A. Schaefer, J. Guo, J. Asatryan, A. Peinador Veiga, S. Haraguchi, J. Martín, M. Campoy-Quiles, C. Müller, *manuscript in preparation* **2025**.

[79] I. Brunetti, A. Dash, D. Scheunemann, M. Kemerink, *Journal of Materials Research* **2024**, *39*, 1197.

[80] A. J. Moulé, G. Gonel, T. L. Murrey, R. Ghosh, J. Saska, N. E. Shevchenko, I. Denti, A. S. Fergerson, R. M. Talbot, N. L. Yacoub, M. Mascal, A. Salleo, F. C. Spano, *Advanced Electronic Materials* **2022**, *8*, 2100888.

[81] T. L. Murrey, M. A. Riley, G. Gonel, D. D. Antonio, L. Filardi, N. Shevchenko, M. Mascal, A. J. Moulé, *The Journal of Physical Chemistry Letters* **2021**, *12*, 1284.

[82] V. Untilova, J. Hynynen, A. I. Hofmann, D. Scheunemann, Y. Zhang, S. Barlow, M. Kemerink, S. R. Marder, L. Biniek, C. Müller, M. Brinkmann, *Macromolecules* **2020**, *53*, 6314.

[83] A. I. Hofmann, R. Kroon, S. Zokaei, E. Järsvall, C. Malacrida, S. Ludwigs, T. Biskup, C. Müller, *Advanced Electronic Materials* **2020**, *6*, 2000249.

[84] E. Järsvall, T. Biskup, Y. Zhang, R. Kroon, S. Barlow, S. R. Marder, C. Müller, *Chemistry of Materials* **2022**, *34*, 5673.

[85] T. Biskup, *Applied Physics Letters* **2021**, *119*.

[86] W. Zhu, X. Qiu, J. E. M. Laulainen, H.-l. Un, X. Ren, M. Xiao, G. Freychet, P. Vacek, D. Tjhe, Q. He, W. Wood, Z. Wang, Y. Zhang, Z. Qu, J. Asatryan, J. Martin, M. Heeney, C. R. McNeill, P. A. Midgley, I. E. Jacobs, H. Sirringhaus, *Advanced Materials* **2024**, *36*, 2310480.

[87] I. E. Jacobs, G. D'Avino, V. Lemaur, Y. Lin, Y. Huang, C. Chen, T. F. Harrelson, W. Wood, L. J. Spalek, T. Mustafa, C. A. O'Keefe, X. Ren, D. Simatos, D. Tjhe, M. Statz, J. W. Strzalka, J.-K. Lee, I. McCulloch, S. Fratini, D. Beljonne, H. Sirringhaus, *Journal of the American Chemical Society* **2022**, *144*, 3005.

[88] F. Pallini, S. Mattiello, N. Manfredi, S. Mecca, A. Fedorov, M. Sassi, K. Al Kurdi, Y.-F. Ding, C.-K. Pan, J. Pei, S. Barlow, S. R. Marder, T.-Q. Nguyen, L. Beverina, *Journal of Materials Chemistry A* **2023**, *11*, 8192.

[89] Y. Zhong, V. Untilova, D. Muller, S. Guchait, C. Kiefer, L. Herrmann, N. Zimmermann, M. Brosset, T. Heiser, M. Brinkmann, *Advanced Functional Materials* **2022**, *32*, 2202075.

[90] M. Moser, L. R. Savagian, A. Savva, M. Matta, J. F. Ponder, Jr., T. C. Hidalgo, D. Ohayon, R. Hallani, M. Reisjalali, A. Troisi, A. Wadsworth, J. R. Reynolds, S. Inal, I. McCulloch, *Chemistry of Materials* **2020**, *32*, 6618.

[91] R. Kroon, D. Kiefer, D. Stegerer, L. Yu, M. Sommer, C. Müller, *Advanced Materials* **2017**, *29*, 1700930.

[92] D. Kiefer, R. Kroon, A. I. Hofmann, H. Sun, X. Liu, A. Giovannitti, D. Stegerer, A. Cano, J. Hynynen, L. Yu, Y. Zhang, D. Nai, T. F. Harrelson, M. Sommer, A. J. Moulé, M. Kemerink, S. R. Marder, I. McCulloch, M. Fahlman, S. Fabiano, C. Müller, *Nature Materials* **2019**, *18*, 149.

[93] A. Hawkey, X. Rodríguez-Martínez, S. Lindenthal, M. C. F. Jansen, R. Crispin, J. Zaumseil, *Advanced Electronic Materials*, *n/a*, 2400817.

[94] I. E. Jacobs, F. Wang, N. Hafezi, C. Medina-Plaza, T. F. Harrelson, J. Li, M. P. Augustine, M. Mascal, A. J. Moulé, *Chemistry of Materials* **2017**, *29*, 832.

[95] P. Y. Yee, D. T. Scholes, B. J. Schwartz, S. H. Tolbert, *The Journal of Physical Chemistry Letters* **2019**, *10*, 4929.

[96] E. Lim, A. M. Glaudell, R. Miller, M. L. Chabinyc, *Advanced Electronic Materials* **2019**, *5*, 1800915.

[97] D. T. Duong, C. Wang, E. Antono, M. F. Toney, A. Salleo, *Organic Electronics* **2013**, *14*, 1330.

[98] A. Hamidi-Sakr, L. Biniek, J.-L. Bantignies, D. Maurin, L. Herrmann, N. Leclerc, P. Lévêque, V. Vijayakumar, N. Zimmermann, M. Brinkmann, *Advanced Functional Materials* **2017**, *27*, 1700173.

[99] J. Hynynen, D. Kiefer, L. Yu, R. Kroon, R. Munir, A. Amassian, M. Kemerink, C. Müller, *Macromolecules* **2017**, *50*, 8140.

[100] A. R. Chew, R. Ghosh, Z. Shang, F. C. Spano, A. Salleo, *The Journal of Physical Chemistry Letters* **2017**, *8*, 4974.

[101] Z.-D. Yu, Y. Lu, J.-Y. Wang, J. Pei, *Chemistry – A European Journal* **2020**, *26*, 16194.

[102] K. J. Thorley, C. B. Nielsen, *ChemPlusChem* **2024**, *89*, e202300773.

[103] Y. Yang, Z. Liu, G. Zhang, X. Zhang, D. Zhang, *Advanced Materials* **2019**, *31*, 1903104.

[104] J. Mei, Z. Bao, *Chemistry of Materials* **2014**, *26*, 604.

[105] B. Zhu, J. He, H. Shan, X. Cao, J. Zhou, H. Huo, *Macromolecules* **2024**, *57*, 4118.

[106] M. L. Chabinyc, M. F. Toney, R. J. Kline, I. McCulloch, M. Heeney, *Journal of the American Chemical Society* **2007**, *129*, 3226.

[107] N. Siemons, D. Pearce, H. Yu, S. M. Tuladhar, G. S. LeCroy, R. Sheelamanthula, R. K. Hallani, A. Salleo, I. McCulloch, A. Giovannitti, J. M. Frost, J. Nelson, *Proceedings of the National Academy of Sciences* **2023**, *120*, e2306272120.

[108] M. Moser, T. C. Hidalgo, J. Surgailis, J. Gladisch, S. Ghosh, R. Sheelamanthula, Q. Thiburce, A. Giovannitti, A. Salleo, N. Gasparini, A. Wadsworth, I. Zozoulenko, M. Berggren, E. Stavrinidou, S. Inal, I. McCulloch, *Advanced Materials* **2020**, *32*, 2002748.

[109] Y. Wang, E. Zeglio, H. Liao, J. Xu, F. Liu, Z. Li, I. P. Maria, D. Mawad, A. Herland, I. McCulloch, W. Yue, *Chemistry of Materials* **2019**, *31*, 9797.

[110] S. Guchait, A. Dash, A. Lemaire, L. Herrmann, M. Kemerink, M. Brinkmann, *Advanced Functional Materials* **2024**, *34*, 2404411.

[111] A. Dash, S. Guchait, D. Scheunemann, V. Vijayakumar, N. Leclerc, M. Brinkmann, M. Kemerink, *Advanced Materials* **2024**, *36*, 2311303.

[112] V. Vijayakumar, P. Durand, H. Zeng, V. Untilova, L. Herrmann, P. Algayer, N. Leclerc, M. Brinkmann, *Journal of Materials Chemistry C* **2020**, *8*, 16470.

[113] R. Kroon, A. I. Hofmann, L. Yu, A. Lund, C. Müller, *Chemistry of Materials* **2019**, *31*, 2770.

[114] S. Pankaj, E. Hempel, M. Beiner, *Macromolecules* **2009**, *42*, 716.

[115] M. Gazzano, C. Gualandi, A. Zucchelli, T. Sui, A. M. Korsunsky, C. Reinhard, M. L. Focarete, *Polymer* **2015**, *63*, 154.

[116] N. Balar, J. J. Rech, S. Siddika, R. Song, H. M. Schrickx, N. Sheikh, L. Ye, A. Megret Bonilla, O. Awartani, H. Ade, W. You, B. T. O'Connor, *Advanced Functional Materials* **2022**, *32*, 2105597.

[117] H. Tang, Y. Liang, C. Liu, Z. Hu, Y. Deng, H. Guo, Z. Yu, A. Song, H. Zhao, D. Zhao, Y. Zhang, X. Guo, J. Pei, Y. Ma, Y. Cao, F. Huang, *Nature* **2022**, *611*, 271.

[118] Z. Ke, A. Abtahi, J. Hwang, K. Chen, J. Chaudhary, I. Song, K. Perera, L. You, K. N. Baustert, K. R. Graham, J. Mei, *Journal of the American Chemical Society* **2023**, *145*, 3706.

[119] N. Balar, S. Siddika, S. Kashani, Z. Peng, J. J. Rech, L. Ye, W. You, H. Ade, B. T. O’Connor, *Chemistry of Materials* **2020**, *32*, 6540.

[120] J. Li, C. Koshnick, S. O. Diallo, S. Ackling, D. M. Huang, I. E. Jacobs, T. F. Harrelson, K. Hong, G. Zhang, J. Beckett, M. Mascal, A. J. Moulé, *Macromolecules* **2017**, *50*, 5476.

[121] F. Saeedifard, D. Lungwitz, Z.-D. Yu, S. Schneider, A. E. Mansour, A. Opitz, S. Barlow, M. F. Toney, J. Pei, N. Koch, S. R. Marder, *ACS Applied Materials & Interfaces* **2022**, *14*, 33598.

[122] C. G. Tang, K. Hou, W. L. Leong, *Chemistry of Materials* **2024**, *36*, 28.

[123] O. Zapata-Arteaga, B. Dörling, A. Perevedentsev, J. Martín, J. S. Reparaz, M. Campoy-Quiles, *Macromolecules* **2020**, *53*, 609.

[124] K. E. Watts, B. Neelamraju, M. Moser, I. McCulloch, E. L. Ratcliff, J. E. Pemberton, *The Journal of Physical Chemistry Letters* **2020**, *11*, 6586.

[125] S. Darabi, C.-Y. Yang, Z. Li, J.-D. Huang, M. Hummel, H. Sixta, S. Fabiano, C. Müller, *Advanced Electronic Materials* **2023**, *9*, 2201235.

[126] Z. Ke, J. Chaudhary, L. Q. Flagg, K. N. Baustert, A. O. Yusuf, G. Liu, L. You, K. R. Graham, D. M. DeLongchamp, J. Mei, *Advanced Functional Materials* **2024**, *34*, 2400255.

[127] L. Müller, S.-Y. Rhim, V. Sivanesan, D. Wang, S. Hietzschold, P. Reiser, E. Mankel, S. Beck, S. Barlow, S. R. Marder, A. Pucci, W. Kowalsky, R. Lovrincic, *Advanced Materials* **2017**, *29*, 1701466.

[128] J. Liu, M. Craighero, V. K. Gupta, D. Scheunemann, S. H. K. Paleti, E. Järsvall, Y. Kim, K. Xu, J. S. Reparaz, L. J. A. Koster, M. Campoy-Quiles, M. Kemerink, A. Martinelli, C. Müller, *Advanced Functional Materials* **2024**, *34*, 2312549.

[129] G. Chen, X. Xiao, X. Zhao, T. Tat, M. Bick, J. Chen, *Chemical Reviews* **2022**, *122*, 3259.

[130] S. Takamatsu, T. Lonjaret, D. Crisp, J.-M. Badier, G. G. Malliaras, E. Ismailova, *Scientific Reports* **2015**, *5*, 15003.

[131] Z. Li, S. K. Sinha, G. M. Treich, Y. Wang, Q. Yang, A. A. Deshmukh, G. A. Sotzing, Y. Cao, *Journal of Materials Chemistry C* **2020**, *8*, 5662.

[132] Y. Fang, G. Chen, M. Bick, J. Chen, *Chemical Society Reviews* **2021**, *50*, 9357.

[133] M. Hatamvand, E. Kamrani, M. Lira-Cantú, M. Madsen, B. R. Patil, P. Vivo, M. S. Mehmood, A. Numan, I. Ahmed, Y. Zhan, *Nano Energy* **2020**, *71*, 104609.

[134] A. Lund, K. Rundqvist, E. Nilsson, L. Yu, B. Hagström, C. Müller, *npj Flexible Electronics* **2018**, *2*, 9.

[135] F. Mokhtari, G. M. Spinks, C. Fay, Z. Cheng, R. Raad, J. Xi, J. Foroughi, *Advanced Materials Technologies* **2020**, *5*, 1900900.

[136] J.-E. Lee, Y.-E. Shin, G.-H. Lee, J. Kim, H. Ko, H. G. Chae, *Composites Part B: Engineering* **2021**, *223*, 109098.

[137] B. Dörling, J. D. Ryan, J. D. Craddock, A. Sorrentino, A. E. Basaty, A. Gomez, M. Garriga, E. Pereiro, J. E. Anthony, M. C. Weisenberger, A. R. Goñi, C. Müller, M. Campoy-Quiles, *Advanced Materials* **2016**, *28*, 2782.

[138] G. H. Kim, L. Shao, K. Zhang, K. P. Pipe, *Nature Materials* **2013**, *12*, 719.

[139] D. A. Mengistie, C.-H. Chen, K. M. Boopathi, F. W. Pranoto, L.-J. Li, C.-W. Chu, *ACS Applied Materials & Interfaces* **2015**, *7*, 94.

[140] J. D. Ryan, D. A. Mengistie, R. Gabrielsson, A. Lund, C. Müller, *ACS Applied Materials & Interfaces* **2017**, *9*, 9045.

[141] S. Darabi, M. Hummel, S. Rantasalo, M. Rissanen, I. Öberg Månsson, H. Hilke, B. Hwang, M. Skrifvars, M. M. Hamedi, H. Sixta, A. Lund, C. Müller, *ACS Applied Materials & Interfaces* **2020**, *12*, 56403.

[142] A. Lund, N. M. van der Velden, N.-K. Persson, M. M. Hamedi, C. Müller, *Materials Science and Engineering: R: Reports* **2018**, *126*, 1.

[143] H. Xu, Y. Guo, B. Wu, C. Hou, Q. Zhang, Y. Li, H. Wang, *ACS Applied Materials & Interfaces* **2020**, *12*, 33297.

[144] A. Lund, S. Darabi, S. Hultmark, J. D. Ryan, B. Andersson, A. Ström, C. Müller, *Advanced Materials Technologies* **2018**, *3*, 1800251.

[145] N. J. Pataki, N. Zahabi, Q. Li, P. Rossi, M. Cassinelli, M. Butti, M. Massetti, S. Fabiano, I. Zozoulenko, M. Caironi, *Advanced Functional Materials* **2024**, *34*, 2400982.

[146] Database of Thermoelectric Data for Organic p- and n-Type Materials, 2025.

[147] G. Zuo, Z. Li, E. Wang, M. Kemerink, *Advanced Electronic Materials* **2018**, *4*, 1700501.